TÉCNICO LISBOA

Design and Development of a Magnetic Anomaly Detection Unmanned Aerial Vehicle

Bruno Miguel Wong Luís

Thesis to obtain the Master of Science Degree in

Aerospace Engineering

Supervisor: Prof. Afzal Suleman

Examination Committee

Chairperson: Prof. Fernando José Parracho Lau
Supervisor: Prof. Afzal Suleman
Member of the Committee: Dr. Frederico José Prata Rente Reis Afonso

November 2019

Dedicated to my parents. This work was only made possible through their continued love and support, which made the distance between Canada, Portugal and China seem much smaller.

Acknowledgments

The completion of this work was accomplished with a large amount of support from individuals and organizations.

First of all, I would like to thank my supervisor, Professor Afzal Suleman, for believing in me from the beginning and providing me the opportunity for growth and professional development throughout the project. I would also like to thank him for bringing me to Canada where I had the chance of getting to know a new culture and new people.

On the Center for Aerospace Research design team, I'd like to thank everyone who helped me throughout my work. In particular, I would like to thank Dr. José Vale. His knowledge, experience, leadership and availability were of utmost importance for the completion of this work. I recall all the countless hours spent by him and all his patience trying to explain me the best way to tackle a certain problem. Furthermore, Dr. Max Rukosuvev and Sean Bazzocchi also supported me a lot during my thesis. Dr. Max Rukosuvev kindly clarified all my doubts about mechanical design and Sean Bazzocchi kindly clarified all my doubts about control and avionics.

It is also worth mentioning the important contributions from Dr. Zahir Daya (DRDC), Dr. Thomas Naprstek (NRC) and Brad Nelson (Aeromagnetic Solutions Incorporated). Their feedback was crucial for the evolution of the project and to check if all the steps of the design process were in accordance with the mission requirements.

Finally, a very heartfelt thanks to all the friends made in Canada. The amazing moments spent together were countless. Between all the work developed at the Center for Aerospace Research, I also have very fond memories of all the occasions spent together hanging out, playing football, visiting places, etc...

Resumo

Esta tese foca-se no projeto e desenvolvimento de um novo veículo aéreo não-tripulado (UAV) de asa fixa, com um canard e capaz de descolagem e aterragem vertical (VTOL), a ser usado pela Força Aérea do Canadá em missões de Deteção de Anomalia Magnética (MAD).

Uma configuração optimizada para cruzeiro é obtida para a aeronave. Perfis alares adequados para a asa e canard, geometria e dimensões das superfícies sustentadoras, fuselagem, estabilizadores verticais, superfícies de controlo são optimizadas para dotar a aeronave das características mais adequadas em termos de redução de interferência magnética, funcionalidade, aerodinâmica, estabilidade e controlo.

A definição e implementação da arquitectura VTOL é realizada, considerando questões de interferência magnética, consumo de potência, aerodinâmica, rigidez estrutural, vibração e controlo. A melhor localização para os motores VTOL é determinada e o modo de transição da aeronave é estudado.

A aeronave projectada, transportando o sensor MAD-XR no nariz de modo a reduzir a interferência magnética, apresenta um bom desempenho aerodinâmico à velocidade de cruzeiro, bem como boas características de estabilidade longitudinal e lateral. A localização dos motores VTOL respeita as distâncias mínimas requeridas ao sensor MAD-XR, garantindo também um consumo de potência adequado. O atrito devido à presença da arquitectura VTOL é estimado.

Apesar da actual configuração da aeronave cumprir os objectivos estabelecidos para esta tese, são apresentadas soluções para possíveis melhorias em futuras versões da aeronave. Estas soluções visam aumentar eficiência aerodinâmica, reduzir consumo de combustível, aumentar velocidade máxima e reduzir massa do sistema propulsivo.

Palavras-chave: Desenho Preliminar de Aeronaves, Optimização Aerodinâmica, Descolagem e Aterragem Vertical, Transição de Modo de Voo

Abstract

This thesis focuses on the design and development of a new canard fixed-wing vertical take-off and landing (VTOL) unmanned aerial vehicle (UAV) to be used by the Canadian Air Force to conduct Magnetic Anomaly Detection (MAD) operations.

An optimized configuration for cruise is obtained for the aircraft. Suitable wing and canard airfoils, shape and dimensions of the lifting surfaces, fuselage, vertical fins, control surfaces are optimized in order to provide the most adequate magnetic interference reduction, functionality, aerodynamics, stability and control characteristics to the aircraft.

The definition and implementation of the VTOL architecture is also performed, bearing in mind magnetic interference, power consumption, aerodynamic, structural, vibration and control issues. The best location for the VTOL motors is determined and the transition mode of the aircraft is studied.

The designed aircraft, which carries the MAD-XR sensor in its nose in order to reduce the magnetic interference, presents a fine aerodynamic performance at cruise speed, as well as good longitudinal and lateral stability characteristics. The location of the VTOL motors respects the required minimum distances from the MAD-XR sensor, while also meaning a suitable power consumption. The drag due to the presence of the VTOL architecture is estimated.

Although the current design fully fulfils the goals established for this thesis, solutions for possible improvements in future design versions of the aircraft are presented. These solutions are meant to increase aerodynamic efficiency, reduce fuel consumption, increase maximum forward speed and reduce propulsive system mass.

Keywords: Aircraft Preliminary Design, Aerodynamic Optimization, Vertical Take-off and Landing (VTOL), Flight Mode Transition

Contents

List of Tables

List of Figures

List of Symbols

α	Angle of attack
α_{2D}	Airfoil section flow angle
α_c	Canard angle of attack
α_i	Airfoil section downwash induced flow angle
α_{stall}	Stall angle of attack
α_w	Wing angle of attack
β	Sideslip angle
Γ	Circulation (vortex strength)
δ_A	Aileron deflection
$\delta_{A_{max}}$	Maximum aileron deflection
δ_R	Rudder deflection
η_p	Propeller efficiency
η_V	Dynamic pressure ratio at the vertical tail
θ	Euler pitch angle
θ_t	Airfoil section twist angle
μ	Advance ratio
ν	Air dynamic viscosity
ρ	Air density
σ	Rotor blade solidity
τ	Control surface effectiveness
τ_{ij}	Stress tensor
ϕ	Euler roll angle
ϕ_1	Aircraft bank angle when the roll rate reaches its steady-state value
ϕ_{req}	Required aircraft bank angle
ψ	Euler yaw angle
$\vec{\omega_B}$	Body-fixed frame angular velocity
$\vec{\omega_E}$	Earth-fixed frame angular velocity

A_i	Area of rotor i
a_c	Canard lift derivative with respect to its angle of incidence

a_w	Wing lift derivative with respect to its angle of incidence
b_a	Aileron span
b_{ai}	Aileron inboard position
b_{ao}	Aileron outboard position
b_c	Canard span
b_r	Rudder span
b_{ri}	Rudder inboard position
b_{ro}	Rudder outboard position
b_V	Vertical fins span
b_w	Wingspan
c_0	Canard lift at zero angle of incidence
c_a	Aileron chord
c_c	Canard chord
C_D	Aircraft drag coefficient
c_d	Airfoil drag coefficient
C_{D_0}	Base drag coefficient
C_{d_0}	Blade profile drag coefficient
C_{D_c}	Canard drag coefficient
CD_R	Aircraft drag coefficient in rolling motion
C_{D_w}	Wing drag coefficient
C_f	Viscous drag coefficient
C_L	Aircraft lift coefficient
$C_{\mathcal{L}}$	Aircraft roll moment coefficient
c_l	Airfoil lift coefficient
C_{L_α}	Lift coefficient slope
$C_{L\alpha,V}$	Derivative of the vertical fins lift coefficient with respect to the angle of attack
$C_{L_{\alpha,w}}$	Derivative of the wing lift coefficient with respect to the angle of attack
$C_{L\beta}$	Derivative of the aircraft roll moment coefficient with respect to the sideslip angle
$C_{l_{\delta A}}$	Derivative of the aircraft rolling moment coefficient with respect to the ailerons deflection
C_{L_c}	Canard lift coefficient
$C_{l_{max}}$	Maximum aircraft rolling moment coefficient
C_{L_w}	Wing lift coefficient
C_M	Aircraft pitch moment coefficient

C_m	Airfoil pitch moment coefficient
C_N	Aircraft yaw moment coefficient
C_{N_β}	Derivative of the aircraft yaw moment coefficient with respect to the sideslip angle
$C_{N\beta,F}$	Derivative of the fuselage yaw moment coefficient with respect to the sideslip angle
$C_{N_{\delta_A}}$	Derivative of the aircraft yaw moment coefficient with respect to the aileron deflection
$C_{N_{\delta_R}}$	Derivative of the aircraft yaw moment coefficient with respect to the rudder deflection
C_p	Pressure coefficient
c_r	Rudder chord
$\bar{c}_w$	Wing mean chord
$C_{Y\beta,V}$	Derivative of the transverse force caused by vertical fins with respect to sideslip angle
D	Aircraft drag
D_c	Canard drag
d_F	Fuselage maximum diameter
D_{fus}	Fuselage drag
D_i	Lift-induced drag
$D_{viscous}$	Viscous drag
D_w	Wing drag
F	Form factor
Fr	Froude number
F_x	Force in x-direction
F_y	Force in y-direction
F_z	Force in z-direction
g	Gravitational constant
I	Aircraft inertia matrix
i_c	Canard angle of incidence
i_w	Wing angle of incidence
I_{xx}	Aircraft moment of inertia around the longitudinal axis
J	Advance ratio
k_i	Induced power correction factor
L	Aircraft lift
$\mathcal{L}$	Aircraft roll moment
$L_{A_{max}}$	Maximum aircraft rolling moment
L_c	Canard lift

l_F	Fuselage length
L_V	Transverse force caused by the vertical fins
l_V	Distance between the aerodynamic center of the vertical fins and the aircraft CG
l_{VT}	Distance between the aerodynamic center of the vertical fins and the aircraft CG
L_w	Wing lift
L/D	Lift-to-drag ratio
M	Aircraft pitch moment
m	Aircraft mass
M_{acc}	Canard aerodynamic center moment
M_{acw}	Wing aerodynamic center moment
M_x	Moment in x-direction at the origin of the CAD model
M_y	Moment in y-direction at the origin of the CAD model
M_z	Moment in z-direction at the origin of the CAD model
N	Aircraft yaw moment
N_{CG}	Total yaw moment at the aircraft's CG
N_F	Fuselage yaw moment
N_W	Wing yaw moment
P	Pressure
P_{c_i}	Power consumed by rotor i during axial climb
P_{d_i}	Power consumed by rotor i during axial descent
P_F	Front rotor power
P_{ideal}	Ideal power spent by the aircraft
P_P	Pusher engine power
P_R	Rear rotor power
P_{real}	Real power spent by the aircraft
P_{ss}	Steady-state roll rate
Q	Interference factor
q	Dynamic pressure
R	Range
Re	Reynolds number
$\bar{Re}$	Average Reynolds number
R_F	Front rotor radius
R_R	Rear rotor radius

S_a	Aileron area
S_c	Canard area
S_r	Rudder area
S_V	Vertical fins area
S_w	Wing area
S_{wet}	Lifting surface wetted area
t_2	Time for the aircraft to achieve the required bank angle
T_F	Front rotor thrust
T_i	Thrust of rotor i
T_p	Pusher engine thrust
T_R	Rear rotor thrust
t_{ss}	Time interval for the aircraft to reach the steady-state roll rate
$\vec{u}$	Velocity vector
u_0	Aircraft forward velocity (dynamic analysis)
U_1	Aircraft forward velocity in a cross-wind situation
V	Aircraft forward velocity
V_∞	Free-stream velocity
$\vec{V_B}$	Body-fixed frame linear velocity
V_c	Axial climb speed
V_d	Axial descent speed
$\vec{V_E}$	Earth-fixed frame linear velocity
v_{i_F}	Induced speed of the front rotors
v_{i_R}	Induced speed of the rear rotors
V_{stall}	Aircraft stall speed
V_t	Total aircraft speed in a cross-wind situation
V_{tip}	Propeller blade tip speed
V_{trans}	Aircraft transition speed
$\bar{V}_V$	Vertical tail volume coefficient
V_W	Wind speed
V_x	Velocity in x-direction
V_y	Velocity in y-direction
V_z	Velocity in z-direction
W	Aircraft weight

w_0	Wing lift at zero angle of incidence
W_{Fuel}	Fuel weight
w_i	Airfoil section velocity induced by the trailing vortex
x_c	Longitudinal distance between CG and canard aerodynamic center
x_F	Longitudinal distance between the front rotors and the aircraft CG
x_R	Longitudinal distance between the rear rotors and the aircraft CG
x_w	Longitudinal distance between CG and wing aerodynamic center
y_D	Average distance (along wingspan) between the rolling drag center and the aircraft CG
$\frac{d\sigma}{d\beta}$	Vertical tail sidewash gradient
dP/dt	Time rate of roll rate
W/A	Disc loading
W/P	Power loading
W/S	Wing loading

Acronyms

AR	Aspect Ratio
ASW	Anti-Submarine Warfare
CAD	Computer-Aided Design
CFD	Computational Fluid Dynamics
CfAR	Centre for Aerospace Research
CG	Center of Gravity
DRDC	Defence Research and Development Canada
GIS	Geographic Information System
LLT	Lifting Line Theory
MAD	Magnetic Anomaly Detection
MTOW	Maximum Take-off Weight
NRC	National Research Council
SFC	Specific Fuel Consumption
SM	Static Margin
SST	Shear Stress Transport
UAH	Unmanned Autonomous Helicopter
UAS	Unmanned Aircraft System
UASS	Unmanned Aerial Survey System
UAV	Unmanned Aerial Vehicle
UVic	University of Victoria
VTOL	Vertical Take-off and Landing
WLE	Wing Leading Edge

Chapter 1

Introduction

1.1 Overview

The goal of this thesis is to design and develop a canard fixed-wing vertical take-off and landing (VTOL) unmanned aerial vehicle (UAV) to be used by the Canadian Air Force to conduct Magnetic Anomaly Detection (MAD) operations. This aircraft will look for submerged metallic vehicles, namely submarines. The operations will be based from a ship's helipad, and will be conducted in a maritime environment. In order to track the submarines, a Magnetic Anomaly Detection sensor is carried as payload in the nose of the aircraft. The magnetic noise generated by the inboard components of the aircraft cannot exceed tolerable values in the MAD sensor. These limits are defined by the Canadian Air Force.

The project was completed in collaboration with Defence Research and Development Canada (DRDC), National Research Council (NRC) and the University of Victoria (UVic) Centre for Aerospace Research (CfAR).

1.2 Motivation

This thesis represents a wonderful chance for its author to make use of his theoretical knowledge to address a practical case. It is a perfect way to complete a 5-year path and indeed a motive of pride for the author to witness an aircraft being designed and built with a significant contribution from him.

Designing an aircraft such that the magnetic interference in the MAD sensor does not exceed tolerable values is specially hard to achieve, if we take into account that propulsion and flight control systems all carry significant magnetic properties. Internal combustion engines, electric motors, flight control servos, avionics and batteries all represent an important source of magnetic noise. Since these systems cannot be removed it is necessary to mitigate their effects on magnetometer payloads, and ultimately the detection capabilities of the aircraft.

Since most of this aircraft's mission time is spent in cruise, a design with optimum aerodynamic and stability characteristics in cruise is of utmost importance. Obtaining an aircraft configuration that achieves a lift-to-drag ratio as high as possible and minimizes the power consumed are fundamental

constraints to be considered. The minimization of power also implies lighter propulsive system components such as engines and motors. The aircraft configuration should guarantee suitable pitch, roll, yaw and dynamic stability properties as well.

Another motivation regarding this thesis is the fact that the aircraft must be VTOL-capable. Hence, the aircraft will have the advantages of traditional fixed-wing configurations, but also the capability of taking-off and landing in small areas, such as a ship's helipad. Taking specially into consideration the magnetic noise contribution from the VTOL motors, but also other aspects such as power consumption minimization, aerodynamic efficiency, structural stiffness to reduce the aircraft deformation amplitude due to the vibration of the VTOL motors and control feasibility of the aircraft, an ideal location for the VTOL motors should be defined. In order to understand how the aircraft performs the transition from a VTOL stage to a fixed-wing stage and, vice-versa, the evolution of forces and powers should be studied.

In order to complement the analysis of this aircraft, some possible improvements to its design are also presented in this thesis. Additional improvements in future design versions of the aircraft should be determined by obtaining experimental data from ground and flight tests of a proof of concept.

1.3 Background

1.3.1 Brief look at the modern history of Unmanned Aerial Vehicles

An unmanned aerial vehicle, also referred to as unmanned aircraft system, unmanned aircraft, or drone, is the name given to any aircraft that flies without a human pilot onboard during its operations. A UAV can be controlled through various methods, from remote control by a human pilot to fully autonomous navigation [1].

While modern UAV saw their beginning during World War I, it only achieved significant development during World War II and Cold War.

For example, in World War II, Nazi Germany developed a UAV to be used against non-military targets. The Revenge Weapon 1, an unmanned flying bomb better known as the V-1, could reach speeds of almost 800 km/h, carry 900 kg of explosives and could travel 240 km before releasing its ordnance. Its wingspan was about 6 m and it measured nearly 7.6 m long. In towns and cities across Britain, the V-1 was responsible for more than 900 civilian deaths and 35000 injured civilians [2].

During Cold War, it is known that both US and USSR used unmanned drones to some extent to spy on each other, but the specifics are still classified and the leaked reports are often contradictory [3].

It is often assumed that modern drone warfare began in earnest in 1982, when Israel coordinated the use of battlefield UAVs alongside manned aircraft to wipe out the Syrian fleet with very minimal losses. The Israeli Air Force used military drones to recon the enemy's position, to jam communications, and to act as decoys that would prevent the loss of pilot life. The technology used was nothing new, but the Israeli Air Force figured out how to use drone technology in a way that would make operations more successful, and international interest in drone hardware picked up significantly. The US, for example, spent tens of millions of dollars on new drone contracts in 1984 [3].

In the present time, the use of drones by armies across the world is widespread. The US Army itself has at least 678 drones in service, of 18 different types. While the number of drones of the Chinese Army and Russian Army are not known, it is speculated that their figures are similar to that of the US [4].

As UAV technology improved in the military sector, those same technological improvements started being used in the non-military sector. According to a Wall Street Journal report, the history of non-military drone use began in earnest in 2006. Government agencies began using drones for disaster relief, border surveillance and wildfire fighting, while corporations began using drones to inspect pipelines and spray pesticides on farms [3].

Nowadays, with the tremendous technological achievements regarding drone technology, UAV are used in several civil and military applications. Within the civil applications, one can highlight package delivery, agriculture, mining, aerial shooting and so on [5]. Furthermore, the Chinese company EHANG wants to turn drones into a taxi service and has built and tested a quadcopter capable of carrying passengers [6]. Within the military applications, one can highlight espionage, enemy detection and warfare [5]. Given the topic of this thesis, it is important to mention that drones are increasingly being used to detect enemy ships, namely submarines. The use of drone technology together with magnetic anomaly detection (MAD) sensors gives support to this type of missions.

1.3.2 Airborne Magnetometry: Aeromagnetic Survey and Anti-Submarine Warfare with the use of Magnetometers

Magnetometers are mechanical devices that were invented to measure the magnetic fields of objects and anomalies within Earth's geomagnetic field. In more detail, a magnetometer is an instrument with a sensor that measures magnetic flux density. Since magnetic flux density in air is directly proportional to magnetic field strength, a magnetometer is capable of detecting fluctuations in the Earth's field [7].

Also, materials that distort magnetic flux lines are known as magnetic. For example, magnetite possesses magnetic fields of its own, as well as a very high magnetic conductivity. Such magnetic materials create distortions in the Earth's magnetic flux that is flowing around them. Magnetometers detect these distortions.

A magnetometer measures magnetic flux density at the point in space where the sensor is located. A magnetic field drops in intensity with the cube of the distance from the object. Therefore, the maximum distance that a given magnetometer can detect the object is directly proportional to the cube root of the magnetometer's sensitivity [7].

Magnetometers can be classified within two categories [7]:

- Vector magnetometers measure the flux density value in a specific direction in 3 dimensional space. An example is a fluxgate magnetometer that can measure the strength of any component of the Earth's field by orienting the sensor in the direction of the desired component.

- Scalar magnetometers measure only the magnitude of the vector passing through the sensor regardless of the direction. An example is a quantum magnetometer.

In terms of practical application, the use of magnetometers onboard of an aircraft serves normally two main purposes: aeromagnetic survey and anti-submarine warfare (ASW).

Aeromagnetic surveys consist of measuring the intensity of the geomagnetic field in order to detect local magnetic variations from the rocks. The resulting aeromagnetic data is generally used to support the mapping of geological formations and accidents that have effects on these in order to directly detect any concentrations of magnetic minerals. This type of survey is used by government geological services and is quite useful for land-use development and planning. It is also used by mining and oil exploration companies, as well as for hydrogeological, archaeological, environmental and even military research [8].

Magnetometers are fixed onto an aircraft, a helicopter or a UAV that flies over the area by performing a series of equidistant linear pathways to collect magnetic measurements. The direction of the lines is generally perpendicular to the geological structures of the area to study. Then, the data is processed to produce profiles, maps and models that geologists can interpret [8].

Modern technology in geophysical drone surveys is now able to sample data at very high resolution compared to those of geophysical land surveys on the ground and, do so at a lower cost and without having to resort to line cutting [8].

As for anti-submarine warfare, as early as 1917, alternatives to the detection of submarines by hydrophones were being studied. One such area for consideration was the use of magnetism. In 1918, the US experimentally tried a ship towed magnetic detection device. This device was found to have too limited a detection range and also suffered from the presence of the magnetic signature of the towing ship. For the time being, magnetic detection was abandoned as impractical [9].

With the outbreak of WW II, renewed interest occurred in alternative detection systems for anti-submarine warfare. For aircraft, there was a pressing need to devise a means for them to be able to detect a submerged submarine. One of the strategies that received renewed attention was the use of magnetic anomaly detection sensors [9]. The advent of the electronic magnetometer during World War II led to the use of airborne magnetometry for the detection, classification, localization, tracking and neutralization of submarines [10].

As early as 1941, magnetic detection devices had been developed in both Britain and the US. The first airborne use of these devices was in US K type blimps. This was followed by much wider installation of MAD devices in ASW patrol aircraft. By 1943 most ASW aircraft were equipped with MAD [9].

Initially, the US thought that MAD would be a primary mean of detecting submerged submarines. In use, MAD was found to be a system of limited usefulness. This was due to its very limited range and its incapability to distinguish between sources of magnetic variance. Frequently, wrecks or local magnetic disturbances were classified as submarines. This was particularly true earlier in the war before experience with the system had discovered its limitations [9].

By late war, MAD in combination with sonobuoys proved more useful. In combination, MAD allowed an aircraft to localize a contact made with sonobuoys and these sonobuoys provided confirmation that the contact was, indeed, a submarine. In this combination MAD became the secondary system to the sonobuoy, the reverse of what was originally expected [9].

Currently, the development of more sophisticated magnetometers and aircraft with lower magnetic

signatures is a core goal in the military sector. Research about how to employ MAD UAV within the context of ASW is a hot topic, since using UAV reduces the number of human lives at risk, especially in a war scenario.

1.3.3 Existing Aeromagnetic Survey and Anti-Submarine Warfare Aircraft

Existing aircraft that perform aeromagnetic survey are not that hard to find. However and although nowadays every blue-water navy is equipped with a MAD UAV, information regarding ASW aircraft is harder to find since it is normally classified. Below, a list of aircraft either performing aeromagnetic survey or ASW operations is presented.

Brican TD 100

TD 100 (see figure 1.1) is a high performance, fixed wing unmanned air vehicle developed by Brican Automated Systems of Brampton, Ontario, Canada [11] - [12]. Its concept was first defined in 2009.

This aircraft was developed as a multi-purpose aircraft. The vehicle has been used for aerial photography, low cost mapping, forest fire research, georeferenced mapping and, more recently, fitted with two Magnetic Anomaly Detection Systems including the Geometrics from the US and the 1.5 kg (MAD-XR) magnetometer manufactured by CAE in Montreal [11] - [12].

TD 100 is designed for a maximum weight of 25 kg. TD 100 can be catapult-launched from a ship or land. A very clean tractor propeller layout is used with a lightweight composite structure and a high aspect ratio wing to obtain good range and endurance. Also, there is a large capacity main payload bay that can accommodate large payloads. The payload bay is located under the wing which means that changes in the payload's fore and aft centre of gravity location or its weight do not cause large changes in the aircraft's centre of gravity when fully loaded which alleviates potential balance problems [12].

The first version of the vehicle was electrically powered using high energy density lithium-polymer batteries. It had a usable duration of more than two hours and it was very quiet. However, to substantially extend the range and duration, a version using a multifuel combustion engine was later developed [12].

In the spring of 2015, the Department of National Defence Industrial Research Program tested the aircraft's utility for coastal defense and detecting submarines [11].

Figure 1.1: Brican TD 100 [11]

Height Technologies PD-1 UAV

PD–1 UAV (see figure 1.2) is a multipurpose modular fixed–wing UAV with a wide range of payloads to fit any mission. Developed by the Dutch company Height Technologies, it is a combat–proven solution

that has been officially on service in Ukrainian Armed Forces since 2016 and previously tested for 2 years [13].

PD-1 UAV is used in many civil and military tasks. Among civil tasks, one can point aerial shooting and agriculture. Among military tasks, one can point advanced sea motion detection and border control. Furthermore, since PD-1 UAV is a small drone with low radar and magnetic signature and, hard to detect, it is also used to carry sensitive payload, such as a magnetometer [13].

The aircraft can be catapult-launched, take-off and land in a conventional way using a runway or use a VTOL approach. The PD–1 UAV VTOL conversion kit is able to convert any existing PD–1 drone into a vertical take-off and landing fixed–wing drone by adding extra four electric motors [13].

This UAV also has a modular design (allows to quickly add, remove, or replace airframe parts, engine unit, payloads and other equipment onboard), hybrid propulsive system (4–stroke engine for more than 10 hours of endurance plus a 150 W on-board generator to recharge main batteries during the flight and power up all equipment onboard), low radar visibility (due to the fully composite airframe and absence of large metal parts) and a parachute recovery system with airbag to make impact softer [13] - [14].

In terms of performance, PD-1 UAV has a MTOW of 40 kg, being capable of carrying payload up to 10 kg. With a ceiling of 3 km, it is designed to cruise at 95 km/h and has a stall speed of 50 km/h [13].

Figure 1.2: Height Technologies PD-1 UAV [15]

HAASW UTAS

In January 14, 2015, an article [16] revealed that anti-submarine warfare experts at BAE Systems were developing a UAV sensor payload able to look for submerged enemy submarines by detecting small variations in the Earth's magnetic field. The goal of this drone would be to help US Navy P-8A find submarines from high altitudes.

The HAASW (High Altitude Anti-Submarine Warfare) UTAS (Unmanned Targeting Air System) is integrated with a MAD sensor and algorithms for use on an air-launched drone that P-8A (see figure 1.3) will use to detect and pinpoint enemy submarines [16].

Figure 1.3: Left image: US Navy P-8A Poseidon. Right image: HAASW UTAS for the Navy P-8A Poseidon Maritime Patrol Jet [16]

MQ-8 Fire Scout

MQ-8 Fire Scout (see figure 1.4) is an Unmanned Autonomous Helicopter (UAH) developed by Northrop Grumman - USA in 2009 [17].

This UAV is used for several types of payload, according to its mission. It can carry a MAD sensor and be used to detect surface submarines (with limited capability), however its main application is carrying weapons [18].

Figure 1.4: MQ-8 Fire Scout [17]

Geoscan 201

Geoscan 201 (see figure 1.5) is an Unmanned Aerial Survey System that can fly a wide choice of payload during a substantial amount of time. It is developed by the Russian company Geoscan [19]. The last version of this aircraft is from 2015 [20].

This aircraft is used in aeromagnetic survey, GIS, mining, agriculture and inspection [20].

Geoscan 201 is designed for a maximum weight of 8.5 kg with a maximum payload of 1.5 kg. The propulsion of this aircraft is fully electric. It is catapult-launched and not capable of VTOL. The aircraft is designed to have a 3-hour endurance, being also capable of reaching a maximum speed of 130 km/h. Its ceiling is 4000 m [20].

As a disadvantage, no collision avoidance system is incorporated in this aircraft [20], which affects the safety regarding its operation and means that it can only operate in areas far from major air traffic routes, tall buildings and mountains.

Figure 1.5: Geoscan 201 [19]

GeoSurv II

GeoSurv II (see figure 1.6) is a small, all-composite UAV used to perform geomagnetic surveys, using a pair of sensitive cesium magnetometers mounted on its wing tips. Such surveys are extremely important for mineral and hydrocarbon exploration, and are frequently used, in conjunction with gravitational surveys, to determine prime locations to perform more expensive seismic surveying. It is a joint project between Carleton University and Sander Geophysics [21].

GeoSurv II is designed to be magnetically neutral to prevent interference with the highly sensitive magnetic imaging hardware onboard. This includes design choices such as using only titanium geared

servo actuators, all-composite structure, and a general avoidance of ferromagnetic materials [21].

Figure 1.6: GeoSurv II [22]

1.4 Topic Overview

1.4.1 Payload description: MAD-XR sensor

The CAE Inc MAD-XR (see figure 1.7 and table 1.1) is a military-grade MAD sensor that is improved and miniaturized from the existing AN/ASQ-508A MAD sensors used by ASW aircraft around the world [23]. The MAD-XR sensor unit combines a three-axis vector magnetometer with three scalar magnetometers in a splayed configuration to minimize dead zones.

The vector magnetometer senses the transverse, longitudinal and vertical components of Earth's geomagnetic field while the scalar magnetometers detects relative spikes (anomalies) in the ambient magnetic field. In the ASW application, and depending on a variety of factors including the magnetic noise inherent to the platform on which it is installed, the MAD-XR system will generally detect anomalies at target ranges of approximately 1200 m [23].

Figure 1.7: MAD-XR sensor used as payload [23]

Parameter	Value
Length	24 cm
Diameter	15 cm
Weight	1.5 kg

Table 1.1: Characteristics of the MAD-XR sensor

1.4.2 Minimum required distances between MAD-XR sensor and inboard components of the aircraft

Previously and, as part of Cody Hansen's Master's Thesis [24], NRC, CAE, DRDC and Aeromagnetic Solutions Incorporated developed an outstanding analysis regarding the minimum required distances between the MAD-XR sensor and the inboard components of an existing aircraft in the Center for Aerospace Research, the Nebula N1 UAV.

Since Nebula N1 UAV was not VTOL-capable, this aircraft was not used subsequently to perform a MAD mission with the characteristics desired by the Canadian Air Force. Nonetheless, Nebula N1 UAV's cruise characteristics are quite similar to the mission requirements defined for this new aircraft (refer to subsection 1.4.3) and, most of its inboard components will also be used in this new aircraft.

Hence, extrapolating from the analysis conducted in [24], the list with the minimum required distances between the MAD-XR sensor and the inboard components of the aircraft (see table 1.2) was provided by Brad Nelson from Aeromagnetic Solutions Incorporated.

Component	Distance	Component	Distance
Gas engine	1.95 m	Silvus radio	1.37 m
VTOL Motor & Electric Engine	1.35 m	Piccolo autopilot	1.22 m
Currawong servo	1.76 m	Battery pack #1	0.65 m
DGPS antenna	1.86 m	Battery pack #2	1.52 m
DGPS electronics	1.17 m	Mobius camera	0.23 m
Video encoder	1.04 m	900 MHz connector	1.55 m

Table 1.2: Minimum required distances between MAD-XR sensor and inboard components of the aircraft

1.4.3 Requirements defined for the aircraft's MAD mission

Besides all the minimum required distances between the MAD-XR sensor and the inboard components, the design of the aircraft must also be compliant with the requirements established for its mission, which were provided by DRDC and are listed in table 1.3. The mission profile is depicted in figure 1.8.

Requirement	Value	Requirement	Value
Cruise speed	30 - 50 m/s	Dash range	25 km
Cruise time	4 - 6 h	Maximum stall speed	20 m/s
Cruise altitude	60 - 140 m	MTOW	35 kg

Table 1.3: Requirements defined for the aircraft's MAD mission

Figure 1.8: Mission profile

1.4.4 Aircraft operation

The propulsive system of this aircraft is comprised of electric motors and a fuel engine.

To comply with the fact that the aircraft must be VTOL-capable, 4 electric motors will be responsible for this task. They must provide enough thrust not only to overcome the aircraft's weight, but also to make it controllable. The electric motors' location must respect the tolerable limits defined for the magnetic noise in the MAD-XR sensor.

In cruise, the aircraft will solely be powered by a pusher piston engine. The length of the aircraft shall guarantee that the piston engine is placed at enough distance from the MAD-XR sensor.

During transition between VTOL and fixed-wing stage, the electric motors and the piston engine will be operating together. Initially, the aircraft is in hover state, solely due to the contribution of the thrust generated by the electric motors to overcome the weight. As the forward speed is gradually increased, the lift from the lifting surfaces gradually starts playing a more prominent role in overcoming the weight and the thrust from the electric motors is gradually reduced, while the pusher thrust increases to balance the increasing drag. The electric motors shall not be switched off before the stall speed of the aircraft is surpassed, since the single contribution from the lift of the aircraft is still not enough to overcome the weight. Once the stall speed of the aircraft is surpassed, the electric motors can be switched off and the aircraft finishes its transition, being now in forward flight condition and just powered by the piston engine.

1.5 Objectives

This thesis is meant to suit the following goals:

- Sizing of an aircraft configuration with adequate aerodynamic and stability (both static and dynamic) characteristics
- Designing a fuselage capable of carrying the MAD-XR sensor and other internal components at an adequate distance from the MAD-XR sensor
- Sizing of the control surfaces
- Defining the VTOL architecture, namely the most suitable location for the VTOL motors
- Modeling, analysing and understanding the aircraft's behaviour in transition mode
- Performing a final aerodynamic/stability analysis of the designed aircraft
- Presenting possible improvements for future design versions of this aircraft
- Establishing suitable mathematical relationships between the physical variables of the designed aircraft and the physical variables of its scaled down proof of concept

1.6 Thesis Outline

There are four remaining chapters in this thesis. A brief description of the contents of subsequent chapters is provided below.

Chapter 2: Aircraft Design Methodology

In this chapter, a full description and explanation of all the rationale and theoretical models used throughout the project is provided.

A complete presentation of the design procedure followed, i.e, every steps performed while designing the aircraft, is given.

All the theories used to size the lifting surfaces, fuselage and vertical fins are presented. The engineering tools used to assess the aerodynamic and stability properties of the aircraft are mentioned, as well as the empirical equations used to dimension its control surfaces. The theoretical models used to understand the behaviour of the aircraft during VTOL and transition stages are also introduced. The dynamic model of the aircraft is provided too.

Chapter 3: Aircraft Design - Implementation and Results

In this chapter, the implementation of the theoretical models mentioned in Chapter 2, as well as the results obtained are presented.

Initially, still without taking into account the presence of a VTOL architecture, a suitable configuration for the aircraft to perform efficiently in cruise is obtained. Lifting surfaces, fuselage, vertical fins and control surfaces are designed for this purpose. Aerodynamic and stability analysis are carried out.

Later, the VTOL architecture is incorporated in the aircraft. The position of the VTOL motors determines the behavior of the aircraft during VTOL and transition stages, namely in what regards the forces and powers required from the electric motors and fuel engine.

A final configuration, suitable for fixed-wing, VTOL and transition, is then obtained for this aircraft.

Chapter 4: Aircraft Performance Analysis

In this chapter, the performance of the designed aircraft is evaluated.

First of all, a final aerodynamic/stability analysis of the aircraft is performed. This allows to estimate the aerodynamic forces and moments for different aerodynamic angles, but also to understand the additional drag associated with the presence of the VTOL architecture. Fuel estimation is carried out as well.

The flight dynamics modes are calculated for the aircraft under consideration. This allows to understand if the aircraft is dynamically stable or unstable for different flight conditions.

Lastly, solutions to improve future design versions of this aircraft are listed, namely the feasibility and advantages of variable-pitch propellers instead of fixed-pitch propellers, detachable booms instead of fixed booms and, a tilt rotor replacing the two rear VTOL motors and pusher engine of the actual aircraft.

Chapter 5: Conclusions

In this chapter, the summary and achievements of this thesis are listed. Major conclusions and suggestions for future work are then provided.

Chapter 2

Aircraft Design Methodology

2.1 Aircraft Design Stages

The design of this aircraft is divided in three stages.

The first stage consists of obtaining an aircraft configuration optimized for cruise, however without taking into account the presence of the VTOL architecture yet. Theoretical results, empirical methods and engineering tools are used to design the aircraft so as to meet all its mission requirements in the best way possible, namely in what regards the aerodynamic performance and stability.

The second stage consists of incorporating the VTOL architecture in the previously obtained configuration. The most suitable location for the VTOL motors is defined and a final configuration is obtained for the aircraft.

The third stage consists of analysing the aerodynamic, static and dynamic stability performance of the designed aircraft for different flight conditions. Using this theoretical data, solutions for possible improvements in future design versions are presented. The determination of other needed improvements is only possible with experimental data collected from ground and flight testing of a proof of concept.

2.2 Aircraft Design Procedure

Designing an aircraft is a cumbersome task and an iterative step-by-step process is followed so as to fully optimize and understand the characteristics of the aircraft and, proceed to eventual corrections during the design procedure, if necessary.

By using a step-by-step process, attention is focused on a certain characteristic of the aircraft and its design is optimized in order to fulfill the requirements for that characteristic. After a suitable design is achieved, the focus is switched to another characteristic of the aircraft and a design optimization is also carried out. In every steps of the aircraft design procedure, it should also be checked if previously designed characteristics were not affected in such a way that can jeopardize the good performance of the aircraft. The design procedure is iterative until a suitable aircraft configuration is finally obtained.

A flowchart with all the design steps followed is shown in figure 2.1.

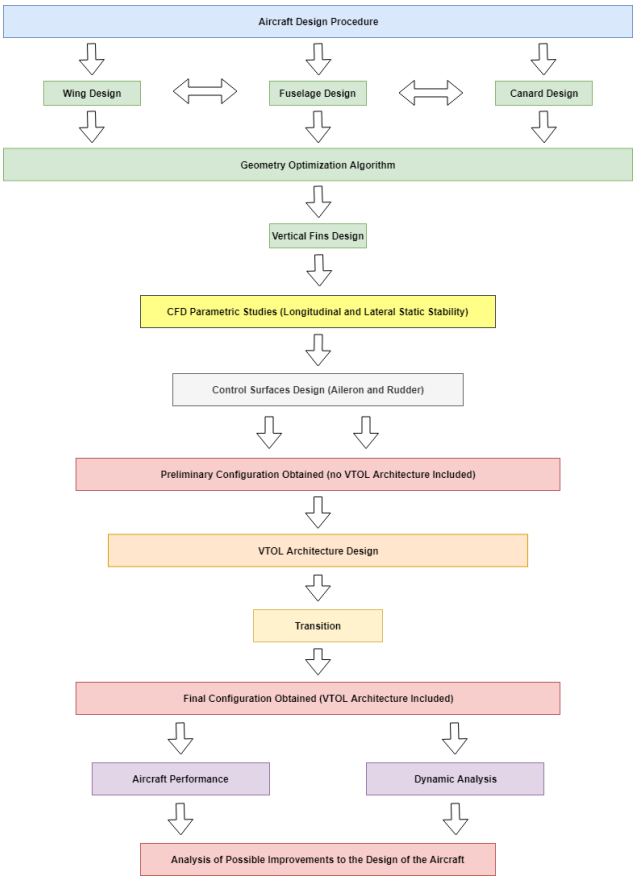

Figure 2.1: Steps followed during the design of the aircraft

The design procedure starts with obtaining a first configuration for the aircraft. A wing and a canard are designed so as to provide a good aerodynamic performance to the aircraft. The fuselage is mainly designed to be able to carry all the required internal components, though aerodynamic considerations are also taken into account. The location of the lifting surfaces with respect to the fuselage should provide the aircraft with adequate longitudinal stability characteristics. The lateral stability characteristics of the aircraft are taken into consideration by sizing the vertical fins. It was defined that vertical fins on the wingtips (thus, also acting as winglets) would be the ideal solution for this aircraft. An empirical method is used to obtain a first design for the vertical fins.

After obtaining a suitable first design for the aircraft, CFD parametric studies are carried out in order to enhance the geometry of the aircraft. By using a detailed CFD model to analyse the aircraft, a better assessment of the aerodynamic forces and moments applied can be performed and, subsequently, used to refine its aerodynamics, longitudinal and lateral static stability characteristics.

The control surfaces are then sized. Pitch control is achieved with the variation of canard incidence, so the only control surfaces used by the aircraft are ailerons (roll control) and rudders (yaw control).

Having designed the wing, canard, fuselage, vertical fins and control surfaces, a preliminary aircraft configuration (optimized for cruise, no VTOL architecture included) is thus obtained.

After obtaining this preliminary configuration, there is the need to conduct important studies regarding the most suitable characteristics for the VTOL architecture. The most adequate location for the VTOL motors is defined based on complying to magnetic interference, power consumption, aerody-

namic, structural, vibration and control requirements.

The aircraft's performance in flight transition is also presented in this thesis. A look at the evolution of forces and power consumption during the transition stage is provided. For a certain value of forward speed during transition, we can determine the required thrust for the rotors, pusher engine thrust and lift of the aircraft. The power consumed by the VTOL motors and the pusher engine can also be estimated.

With the VTOL architecture defined and incorporated, a final configuration is obtained for the aircraft. Aerodynamic efficiency, static and dynamic stability analysis of the aircraft are performed. The feasibility and advantages of possible improvements to the current aircraft design are determined.

2.3 Preliminary Configuration Design

A flowchart with the procedure used to obtain a basic configuration (wing, canard and fuselage) for the aircraft is shown in figure 2.2.

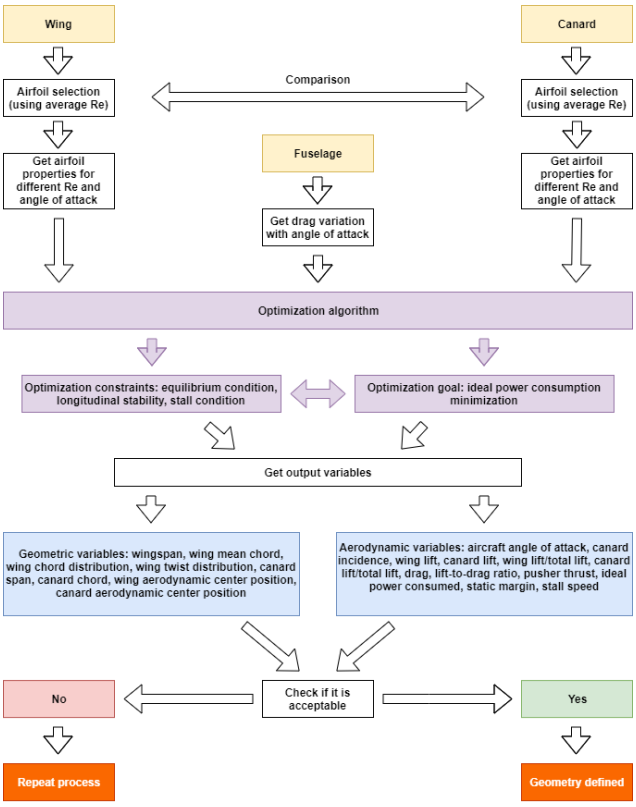

Figure 2.2: Basic configuration design: steps

Initially, it is important to define the airfoils used by the wing and canard. The aerodynamic characteristics of an airfoil vary with the angle of attack α and with the Reynolds number Re. Furthermore, the local chord of the wing and canard may not be constant and vary throughout the span, which implies that different local airfoils in both the wing and canard might be operating at different Re. The wing and canard may also have twist, which means that different local airfoils in both the wing and canard might be operating at different α. All these questions make the selection of adequate airfoils hard, however it is

possible to simplify the problem by using the average Reynolds number $\bar{Re}$ (based on the mean chord) of both the wing and canard to respectively select the most suitable airfoils.

For the $\bar{Re}$ of the wing and for the $\bar{Re}$ of the canard and, for different airfoils, lift and drag coefficients as a function of α are obtained. By comparing results between different airfoils, airfoils for the wing and the canard are selected. For the selected airfoils, the lift and drag coefficients as a function of Re (to take into account chord variation throughout the span of the lifting surfaces) and as a function of α (to take into account different flight conditions and twist effects) are obtained.

A fuselage is also designed. The primary design goal of the fuselage is to be able to fit all the required internal components, namely the MAD-XR sensor and the pusher engine which are expected to be the biggest components. The fuselage is also designed to be as aerodynamically smooth as possible in order to reduce its contribution for the aircraft's total drag. The fuselage drag coefficient as a function of its angle of attack α is obtained.

In order to define the most suitable geometry for the lifting surfaces as well as their location with respect to the fuselage, an optimization strategy was devised. For different forward velocities and while respecting a set of constraints, the code calculates the span, chord and twist distributions of the lifting surfaces, the distance between their aerodynamic centers and the aircraft center of gravity as well as the aerodynamic angles, lift and drag values that minimize the ideal power spent by the aircraft during cruise.

2.3.1 Airfoil selection

As mentioned previously, the first step is about selecting the most suitable airfoil for both the wing and the canard. Once the airfoils are selected, there is the need to obtain their aerodynamic properties for different angles of attack α and different Reynolds numbers Re.

In order to accomplish these calculations, XFOIL software is used. XFOIL is an interactive program for the design and analysis of subsonic isolated airfoils. Given the coordinates specifying the shape of a 2D airfoil, Reynolds and Mach numbers, XFOIL can calculate the pressure distribution on the airfoil and hence lift and drag characteristics. Calculations are performed by using Panel Method Theory with drag models included [25].

The inviscid formulation of XFOIL is a simple linear-vorticity stream function panel method. A finite trailing edge base thickness is modeled with a source panel. The equations are closed with an explicit Kutta condition [26].

The boundary layers and wake are described with a two-equation lagged dissipation integral boundary layer formulation and an envelope e^n transition criterion. The entire viscous solution (boundary layers and wake) is strongly interacted with the incompressible potential flow via the surface transpiration model. This permits proper calculation of limited separation regions. The drag is determined from the wake momentum thickness far downstream [26].

The boundary layer and transition equations are solved simultaneously with the inviscid flowfield, yielding a nonlinear elliptic system of equations, which is solved by a global Newton method [27].

2.3.2 Wing and canard

As for the design of the wing and canard, 3 different methods/theories are used to calculate the aerodynamic forces and moments applied on the wing and canard for different angles of attack: Lifting Line Theory, 3-D Panel Method Theory with drag models included (using XFLR5 software) and Navier-Stokes equations (using CFD commercial software Ansys).

Lifting Line Theory

A simple solution for high aspect ratio, unswept, 3-D wing/canard can be obtained by using Prandtl's Lifting Line Theory. For incompressible, inviscid and steady flow, the wing/canard is modelled as a single bound vortex line located at the 1/4 chord position and an associated shed vortex sheet [28]. Figure 2.3 gives a better understanding of what is mentioned.

In figure 2.3, Γ is the circulation (vortex strength), V_∞ is the free-stream velocity, α is the wing/canard angle of attack, b is the wing/canard span, s is the wing/canard semi-span, c is the wing/canard chord and y is the distance across the span measured from the wing/canard root [28]. The circulation Γ and the chord c are written as function of the coordinate y, i.e, $\Gamma = \Gamma(y)$ and $c = c(y)$.

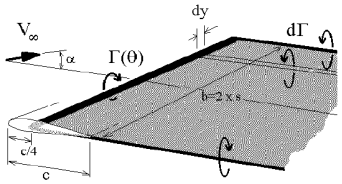

Figure 2.3: Lifting Line Theory model [28]

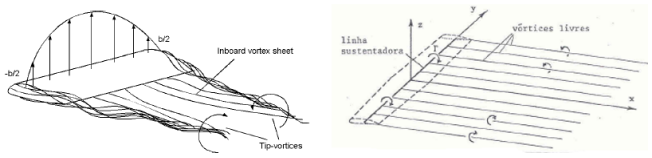

Figure 2.4: Left image: non-linear problem. Right image: linear problem

In the Lifting Line Theory, the lift per wingspan unit $L(y)$ of each 2-D section of the 3-D wing/canard is related with the circulation $\Gamma(y)$ by means of the Joukowski theorem. In general, the shed vortexes first align themselves with the incoming flow streamlines and then merge themselves with the tip vortexes. The problem is thus non-linear, however for small angles of attack, thickness and curvature, it is possible to linearize the problem and consider that the shed vortexes are always approximately aligned with the incoming flow streamlines and do not merge themselves with the tip vortexes [29]. Figure 2.4 depicts the differences between the non-linear problem and the linear problem.

In a 3-D wing/canard, the shed vortexes that are produced and trail behind the wing/canard cause a downwash. It can be proved that, for every 2-D sections of the 3-D wing/canard, the sum of the section flow angle with the section downwash induced flow angle must be equal to the sum of the angle of attack of the wing/canard with the section twist angle [28], as can be seen in figure 2.5.

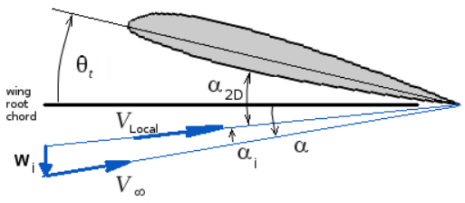

Figure 2.5: Relationship between the different angles in a 2-D section of the 3-D wing/canard [28]

, where α is the 3-D wing/canard angle of attack, θ_t is the section twist angle, α_{2D} is the section flow angle and α_i is the section downwash induced flow angle. In algebraic terms, we have:

$$\alpha + \theta_t(y) = \alpha_{2D}(y) + \alpha_i(y) \tag{2.1}$$

For a 2-D section, we can use the Joukowski theorem to relate the local lift coefficient $C_l(y)$ with the local circulation $\Gamma(y)$, the free-stream velocity V_∞, the local chord $c(y)$, the local lift derivative with respect to the local angle of attack $C'_{l\infty}(y)$, the local angle of attack $\alpha_{2D}(y)$ and the local zero-lift angle of attack $\beta(y)$, as shown in equation 2.2. This allows us to obtain equation 2.3 [29].

$$C_l(y) = \frac{2 \cdot \Gamma(y)}{V_\infty \cdot c(y)} = C'_{l\infty}(y) \cdot (\alpha_{2D}(y) + \beta(y)) \tag{2.2}$$

$$\alpha_{2D}(y) = \frac{2 \cdot \Gamma(y)}{C'_{l\infty}(y) \cdot V_\infty \cdot c(y)} - \beta(y) \tag{2.3}$$

For small angles of attack and by making use of the Helmotz theorem, the following relationship between the section downwash induced flow angle α_i and the section velocity induced by the trailing vortex sheet w_i is valid [29]:

$$\alpha_i(y) = \frac{1}{4\pi \cdot V_\infty} \int_{-b/2}^{b/2} \frac{1}{y - y'} dy' \tag{2.4}$$

Replacing equations 2.3 and 2.4 in equation 2.1, we can obtain the final equation to be solved when using the Lifting Line Theory [29]:

$$\alpha + \theta_t(y) = \frac{2 \cdot \Gamma(y)}{C'_{l\infty}(y) \cdot V_\infty \cdot c(y)} - \beta(y) + \frac{1}{4\pi \cdot V_\infty} \int_{-b/2}^{b/2} \frac{1}{y - y'} dy' \tag{2.5}$$

By solving equation 2.5, we can obtain the lift L and the lift-induced drag D_i (drag associated with the generation of lift) of the 3-D wing/canard for different angles of attack. These quantities are, respectively, given by equations 2.6 and 2.7 [29].

With direct application of the Lifting Line Theory equations, it is not possible to take into account the viscous drag (this is an inviscid theory), however the viscous drag can be calculated by integration of the drag of all the 2-D airfoils along the wing/canard span, as shown by equation 2.8. Using information obtained from XFOIL software, the viscous drag of a 2-D airfoil is known, once information about its Reynolds number Re and angle of attack α_{2D} is known.

$$L = \rho \cdot V_\infty \cdot \int_{-b/2}^{b/2} \Gamma(y) dy \tag{2.6}$$

$$D_i = \rho \cdot \int_{-b/2}^{b/2} w_i(y) \cdot \Gamma(y) dy \tag{2.7}$$

$$D_{viscous} = \frac{1}{b} \cdot \int_{-b/2}^{b/2} D_{airfoil}(y) dy \tag{2.8}$$

3-D Panel Method with drag models included - XFLR5

In [30], guidelines about using the XFLR5 software can be found. Although many methods are incorporated in XFLR5, it is recommended to use 3-D Panel Method since it is able to refine the Lifting Line Theory and Vortex Lattice Method results by a more sophisticated full 3D method, taking into account the thickness of the wing/canard, whereas for example the Vortex Lattice Method only considers the mean camber line [30].

The principle of a 3-D Panel Method is to model the perturbation generated by the wing/canard by a sum of doublets and sources uniformly distributed over the top and bottom surfaces of the wing/canard. The strength of the doublets and sources is calculated to meet the appropriate boundary conditions. The wing/canard is meshed into a number of panels distributed over the span and the chord of the planform, and a doublet and a source is associated to each panel [30].

The C_p distribution is calculated as the derivative of the doublet strength along the panel chordwise and spanwise strips. The wake is modeled as a series of flat panels which extend 'far behind' the wing/canard. The idea is that each of the wing/canard's chordwise strip sheds a column of wake panels. The doublet strength of each panel in this wake strip is the difference of the doublet strength of the top and bottom panels of the wing/canard's strip. This is a consequence of the fact that the wake cannot sustain load. In addition, being a thin surface, the wake panels have a zero source strength [30].

Navier-Stokes equations

The aircraft will be operating in the incompressible regime. The Navier-Stokes mass and momentum equations (equations 2.9 and 2.10, respectively) are used to describe how the velocity and pressure of the fluid are related [31].

$$\frac{\partial \rho}{\partial t} + \frac{\partial (\rho u_i)}{\partial x_i} = 0 \tag{2.9}$$

$$\frac{\partial (\rho u_i)}{\partial t} + \frac{\partial (\rho u_i u_j)}{\partial x_j} = -\frac{\partial P}{\partial x_i} + \frac{\partial \tau_{ij}}{\partial x_j} + \rho f_i \tag{2.10}$$

In the above equations, index notation is used and i,j = 1,2,3. Hence, there is a continuity equation for conservation of mass and three conservation of momentum equations. Since the fluid is incompressible, there are four unknowns: the pressure P and the three components of the velocity vector $\vec{u}$ [31].

The terms on the left hand side of the momentum equations are called the convection terms of the equations. Convection occurs when some property is transported by the ordered motion of the flow. The term on the right hand side of the momentum equations associated with the stress tensor τ_{ij} and the fluid viscosity is called the diffusion term. Diffusion occurs when some property is transported by the random motion of the flow. Turbulence and boundary layers are the result of diffusion in the flow. To describe τ_{ij}, different turbulence models can be used [31].

The equations are a set of coupled differential equations and very hard to solve analytically. The strategy is to use Computational Fluid Dynamics (CFD) to solve approximations to the equations using a variety of techniques like finite difference, finite volume, finite element, and spectral methods [31]. To

solve these equations in CFD, a turbulence model must be specified. SST (Shear Stress Transport) turbulence model is used. SST is a robust two-equation eddy-viscosity turbulence model which combines the k-ω and the k-ϵ turbulence models such that the k-ω is used in the inner region of the boundary layer and the k-ϵ is used in the free shear flow [32].

2.3.3 Fuselage

In order to compute the drag of the fuselage for different angles of attack, CFD simulations are performed. The theoretical details regarding the CFD analysis were already mentioned in subsection 2.3.2 when addressing the Navier-Stokes equations.

2.3.4 Geometry optimization problem

In order to obtain the most suitable geometry for an aircraft that is mainly operating in cruise condition, it is important to have a way to understand how different wing and canard geometries, as well as their locations with respect to the fuselage affect the aerodynamic performance and stability of the aircraft. A MATLAB code was created to do so.

As can be seen in figure 2.2 and for a range of forward speeds, the code will determine the wingspan, wing mean chord, wing chord and twist distributions, canard span, canard chord, distance between aircraft CG and wing aerodynamic center, distance between aircraft CG and canard aerodynamic center as well as the aerodynamic angles that minimize the ideal power consumed for each one of these different forward speeds.

The ideal power consumed in cruise $P_{cruise_{ideal}}$ is given, as a function of the required pusher engine thrust T_p and the forward velocity V, by equation 2.11:

$$P_{cruise_{ideal}} = T_p \cdot V \tag{2.11}$$

The power minimization respects important aerodynamic constraints of the aircraft. Namely, the 3 equilibrium equations (vertical, horizontal and pitch moment equilibrium) shall be met, a reasonable value ($\simeq$ 10%) for the static margin in cruise shall be achieved and the stall speed must be less or equal than 20 m/s (based on the requirements stated in table 1.3).

A schematics showing a simplified depiction of the considered forces and moments applied on the aircraft during cruise is presented in figure 2.6.

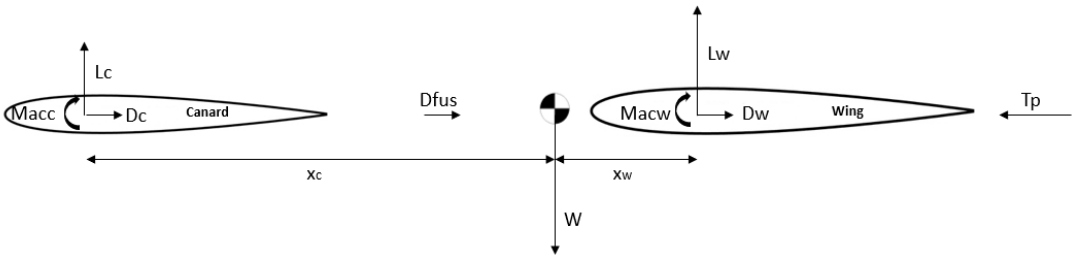

Figure 2.6: Forces and moments applied on the aircraft during cruise

By inspection of figure 2.6, the equilibrium equations 2.12 - 2.14 can be obtained. The static margin is given, in a first approximation, by equation 2.15, where only the wing and canard effects are considered.

$$L_w + L_c - W = 0 \quad (2.12) \qquad T_p - D_w - D_c - D_{fus} = 0 \quad (2.13)$$

$$M_{acw} + M_{acc} + x_c \cdot L_c - x_w \cdot L_w = 0 \quad (2.14) \qquad SM(\%) = \frac{x_w \cdot a_w \cdot S_w - x_c \cdot a_c \cdot S_c}{\bar{c}_w \cdot (a_w \cdot S_w + a_c \cdot S_c)} \cdot 100\% \quad (2.15)$$

In equations 2.12 - 2.15, L_w is the wing contribution to the aircraft's total lift, L_c is the canard contribution to the aircraft's total lift, W is the aircraft's weight, T_p is the pusher engine thrust, D_w is the wing contribution to the aircraft's total drag, D_c is the canard contribution to the aircraft's total drag, D_{fus} is the fuselage contribution to the aircraft's total drag, M_{acw} is the wing aerodynamic center moment, M_{acc} is the canard aerodynamic center moment, x_w is the distance between aircraft CG and wing aerodynamic center, x_c is the distance between aircraft CG and canard aerodynamic center, a_w is the wing lift derivative with respect to its angle of attack, S_w is the wing area, a_c is the canard lift derivative with respect to its angle of attack, S_c is the canard area and $\bar{c}_w$ is the wing mean chord. For purposes of simplicity, T_p, D_w, D_c and D_{fus} related pitch moments are neglected in equation 2.14.

The minimum forward speed at which it is not possible to trim the aircraft, i.e the balance of forces and moments cannot be achieved, is called the aircraft's stall speed. In this algorithm, a first estimation of the stall speed is done, by imposing a maximum angle of attack of 10º for both the wing and canard.

Different aircraft configurations are obtained, each one optimized for a certain forward speed. The aircraft angle of attack α and the canard angle of incidence i_c (the wing angle of incidence i_w is assumed to be 0, as a first approximation) that guarantee a trim condition, as well as the lift-to-drag ratio L/D, the ideal power required and the static margin are calculated. By inspection of these outputs, an aircraft configuration is selected and a mission cruise speed is defined.

2.3.5 Vertical fins

In [33], the design method to obtain some first dimensions for the vertical fins can be found. The vertical fins are used to achieve enough yaw stability in the aircraft.

The total yaw moment N_{CG} at the aircraft's CG is given, as a function of the wing yaw moment N_W, the fuselage yaw moment N_F, the transverse force L_V caused by the vertical fins and the distance l_V between the aerodynamic center of the vertical fins and the CG, by equation 2.16 [33]. The total yaw moment N_{CG} at the aircraft's CG should be positive and counteract the sideslip angle β. N_{CG} is also given by equation 2.17 [33].

$$N_{CG} = N_W + N_F - L_V \cdot l_V \quad (2.16) \qquad N_{CG} = C_{N\beta} \cdot \beta \cdot q \cdot S_W \cdot b_w \quad (2.17)$$

The fuselage yaw moment N_F has a destabilizing effect and is given by equation 2.18 [33]. The transverse force L_V caused by the vertical fins has a stabilizing effect and is given by equation 2.19 [33].

$$N_F = C_{N\beta,F} \cdot \beta \cdot q \cdot S_W \cdot b_w \tag{2.18}$$

$$L_V = C_{Y\beta,V} \cdot \beta \cdot q \cdot S_V \tag{2.19}$$

The wing yaw moment N_W has a stabilizing effect, however since its contribution to the total yaw moment N_{CG} is less important than that of the vertical fins and since there is no method available to estimate its contribution, the wing yaw moment can be disregarded in the calculations [33].

In equations 2.17 to 2.19, β is the sideslip angle, q is the dynamic pressure, S_W is the wing area, b_w is the wingspan and S_V is the area of the vertical fins. $C_{N\beta,F}$ and $C_{Y\beta,V}$ are given by equations 2.20 and 2.21, respectively [33].

$$C_{N\beta,F} = \frac{-360}{2\pi} \cdot k_N \cdot k_{R,I} \cdot \frac{l_F \cdot l_F \cdot d_F}{S_w \cdot b_w} \tag{2.20}$$

$$C_{Y\beta,V} = -C_{L\alpha,V} \tag{2.21}$$

Inserting all the contributions from equations 2.17 to 2.19 in equation 2.16, we have [33]:

$$C_{N\beta} = C_{N\beta,F} - \frac{C_{Y\beta,V} \cdot S_V \cdot l_V}{S_W \cdot b_w} \tag{2.22}$$

Thus, the minimum required area for the vertical fins S_V can be calculated [33]:

$$S_V = \frac{C_{N\beta} - C_{N\beta,F}}{-C_{Y\beta,V}} \cdot \frac{b_w}{l_V} \cdot S_W \tag{2.23}$$

According to [34], the following should be met for sufficient yaw stability

$$C_{N\beta} \geq 0.001/^{\circ} = 0.0571/rad \tag{2.24}$$

2.3.6 CFD parametric studies: longitudinal and lateral stability

After a first design for the fuselage, wing, canard and vertical fins is completed, it is necessary to have a better assessment of the aerodynamics and stability of the full aircraft so as to identify possible problems and modify some of the aircraft's features to tackle those issues.

In order to accomplish the tasks mentioned in the aforementioned paragraph, CFD simulations are performed. The theoretical details regarding the CFD analysis were already mentioned in subsection 2.3.2 when addressing the Navier-Stokes equations.

Regarding its aerodynamic performance, lift and drag forces acting on the aircraft as function of the aircraft's angle of attack and canard angle of incidence are better estimated by means of a CFD analysis.

Regarding the longitudinal stability of the aircraft, CFD simulations are done to evaluate the possible need to improve the pitch stability obtained from the first design for the aircraft (refer to subsection 2.3.4).

This can be achieved by moving the canard backwards, moving the wing backwards and/or by moving the intended CG forward.

As for the lateral stability of the aircraft, CFD simulations are done to evaluate the possible need to improve the yaw stability obtained from the first design for the aircraft (refer to subsection 2.3.5). This can be achieved by increasing the area of the fins, increasing the distance between the CG and the aerodynamic center of the fins and/or by adding a third vertical fin. Roll stability is also evaluated with CFD, in particular if wing dihedral is required.

2.3.7 Control surfaces sizing

Ailerons sizing

In [35], the design method to obtain the dimensions of the ailerons can be found. The ailerons are used to provide enough roll control to the aircraft.

The ailerons are sized for a class I aircraft (small, light aircraft), flight phase category A (anti-submarine search) and level of acceptability 1 (flying qualities clearly adequate for the mission flight phase) [35]. This means that the ailerons should guarantee that the aircraft achieves a bank angle ϕ_{req} of 60º in no more than 1.3 s [35].

The design procedure is iterative. Initially, important parameters that define the geometry of the ailerons must be assumed: the inboard position of the ailerons b_{ai}, the aileron span b_a and the aileron chord c_a. A better understanding of the meaning of these parameters is provided in figure 2.7, which is valid for a generic wing [35].

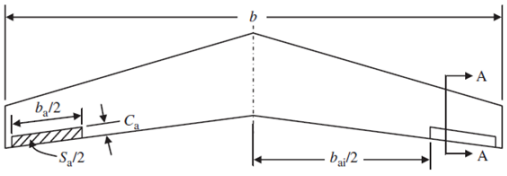

Figure 2.7: Parameters that define the geometry of the ailerons [35]

Once a possible geometry for the ailerons is assumed, it is needed to check if they allow the aircraft to achieve a bank angle of 60º in no more than 1.3 s. To do so, the procedure described next is followed.

The aircraft rolling moment coefficient derivative with respect to the ailerons deflection $C_{l_{\delta A}}$, as a function of the wing lift coefficient derivative with respect to the angle of attack $C_{L_{\alpha,w}}$, the control surface effectiveness τ, the wing chord distribution $c_w(y)$, the wing area S_w, the wingspan b_w, the inboard position of the ailerons y_i and the outboard position of the ailerons y_o, is given by equation 2.25 [35].

$$C_{l_{\delta A}} = \frac{2 \cdot C_{L\alpha,w} \cdot \tau}{S_w \cdot b_w} \int_{y_i}^{y_o} c_w(y) \cdot y dy \tag{2.25}$$

The maximum rolling moment coefficient $C_{l_{max}}$ is achieved when the ailerons have the maximum deflection $\delta_{A_{max}}$, as can be seen in equation 2.26. The maximum rolling moment $L_{A_{max}}$ comes from equation 2.27 [35].

$$C_{l_{max}} = C_{l_{\delta A}} \cdot \delta_{A_{max}} \tag{2.26}$$

$$L_{A_{max}} = \frac{1}{2} \cdot \rho \cdot V^2 \cdot S_w \cdot b_w \cdot C_{l_{max}} \tag{2.27}$$

The aircraft roll rate response to the ailerons deflection has two distinct states: (i) a transient state and (ii) a steady state [35].

The steady-state roll rate P_{ss} is given by equation 2.28. The bank angle ϕ_1 when the roll rate reaches its steady-state value P_{ss} is given by equation 2.29. The time rate of roll rate dP/dt is given by equation 2.30 and the duration t_{ss} for the aircraft to reach the steady-state roll rate P_{ss} is given by equation 2.31.

$$P_{ss} = \sqrt{\frac{2 \cdot L_{A_{max}}}{\rho \cdot S_{total} \cdot CD_R \cdot y_D^3}} \tag{2.28}$$

$$\phi_1 = \frac{I_{xx} \cdot \log(P_{ss}^2)}{\rho \cdot S_{total} \cdot CD_R \cdot y_D^3} \tag{2.29}$$

$$dP/dt = \frac{P_{ss}^2}{2 \cdot \phi_1} \tag{2.30}$$

$$t_{ss} = \sqrt{\frac{2 \cdot \phi_1}{dP/dt}} \tag{2.31}$$

, where S_{total} is the sum of wing, canard and vertical fin areas, CD_R is the aircraft drag coefficient in rolling motion, y_D is the average distance (along the wingspan) between the rolling drag center and the aircraft center of gravity and, I_{xx} is the aircraft moment of inertia around the longitudinal axis [35].

If the bank angle ϕ_1 is greater than the required bank angle (60º), the time t_2 that it takes the aircraft to achieve this required bank angle is given by equation 2.32. If the bank angle ϕ_1 is smaller than the required bank angle (60º), the time t_2 that it takes the aircraft to achieve this required bank angle is given by equation 2.33 [35].

$$t_2 = \sqrt{\frac{2 \cdot \phi_{req}}{dP/dt}} \tag{2.32}$$

$$t_2 = t_{ss} + \frac{\phi_{req} - \phi_1}{P_{ss}} \tag{2.33}$$

If the time t_2 is smaller than the required time of 1.3 s, the design of the ailerons is completed. If the time t_2 is greater than the required time of 1.3 s, a new geometry must be assumed for the ailerons [35] and the whole design process starts all over again.

Rudders sizing

In [35], the design method to obtain the dimensions of the rudders can be found. The rudders are used to provide enough yaw control to the aircraft.

The rudder plays different roles in different flight phases. Some of its major tasks are: cross-wind condition, directional control for balancing asymmetric thrust on multi-engine aircraft, turn coordination and spin recovery. Among these functions, one of them is usually the most critical depending upon the aircraft mission and configuration and, thus, the rudder is designed to meet that most crucial case [35]. For the case of this project, the most critical condition corresponds to a cross-wind condition.

When in a cross-wind situation, the worst-case scenario occurs when the direction of the wind speed $\vec{V_W}$ is totally perpendicular to the forward velocity of the aircraft $\vec{U_1}$, as can be seen in figure 2.8. The existence of cross-wind will cause a sideslip angle β in the aircraft.

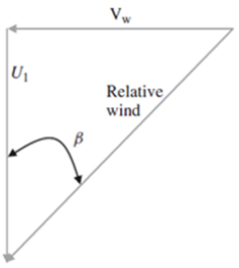

Figure 2.8: Triangle of velocities and sideslip angle in a cross-wind condition [35]

Under these conditions, the total aircraft speed V_t is given by equation 2.34 and the sideslip angle β is given by equation 2.35.

$$V_t = \sqrt{U_1^2 + V_W^2} \tag{2.34}$$

$$\beta = tan^{-1}(\frac{V_W}{U_1}) \tag{2.35}$$

The total yaw moment coefficient C_N at the aircraft CG is given, as a function of the sideslip angle β, the ailerons deflection δ_A and the rudders deflection δ_R, by equation 2.36. It can be assumed that the aircraft is symmetrical ($C_{N_0} = 0$) and that there is no ailerons deflection ($\delta_A = 0$). To have a steady-state motion ($C_N = 0$), we can simplify equation 2.36 and obtain equation 2.37 [35].

$$C_N = C_{N_0} + C_{N_\beta} \cdot \beta + C_{N_{\delta_A}} \cdot \delta_A + C_{N_{\delta_R}} \cdot \delta_R \tag{2.36}$$

$$C_{N_\beta} \cdot \beta + C_{N_{\delta_R}} \cdot \delta_R = 0 \tag{2.37}$$

, where C_{N_β} can be obtained from the CFD analysis or by using equation 2.38. $C_{N_{\delta_R}}$ can be obtained from equation 2.39 [35].

$$C_{N_\beta} = K_{f1} \cdot C_{L_{\alpha,V}} \cdot (1 - \frac{d\sigma}{d\beta}) \cdot \eta_V \cdot \frac{l_{VT} \cdot S_V}{b_w \cdot S_w} \tag{2.38}$$

$$C_{N_{\delta_R}} = -C_{L_{\alpha,V}} \cdot \bar{V}_V \cdot \eta_V \cdot \tau \cdot \frac{b_r}{b_V} \tag{2.39}$$

In equations 2.38 and 2.39, K_{f1} is the fuselage contribution to the aircraft C_{N_β}, $C_{L_{\alpha,V}}$ is the derivative of the vertical fins lift coefficient with respect to the angle of attack, $\frac{d\sigma}{d\beta}$ is the vertical tail sidewash gradient, η_V is the dynamic pressure ratio at the vertical tail and τ is the control surface effectiveness.

Using equations 2.37 - 2.39, the design of the rudders can be performed. First, a geometry for the rudders is assumed. Then, the derivatives C_{N_β} and $C_{N_{\delta_R}}$ can be calculated from CFD analysis (equation 2.38, alternatively) and from equation 2.39, respectively. Using equation 2.37, we can obtain

the required rudder deflection δ_R for a given wind speed and therefore sideslip angle β. In particular, we can calculate the maximum sustained cross-wind, when the maximum rudder deflection is used [35].

2.4 VTOL Architecture Incorporation

This aircraft must be able to comply with one of the main requirements of the mission: vertical take-off and landing. To accomplish this, 4 electric motors are used.

Since the main goal of this project is to reduce magnetic interference in the MAD-XR sensor during the research phase, electric motors (a big source of magnetic noise) are switched off during this phase. However, they must operate during take-off and landing, as well as during transition.

2.4.1 Location of the VTOL motors

When sizing the VTOL architecture, the first aspect to be taken into consideration is the position of the VTOL motors. When selecting the most suitable location for the VTOL motors, magnetic interference, power consumption, aerodynamic, structural, vibration and control issues are considered.

First of all, it is strictly mandatory to guarantee that all the VTOL motors are placed at a distance of at least 1.35 m from the MAD-XR sensor (refer to table 1.2).

Minimizing the power consumption during VTOL stages implies smaller, lighter electric motors and batteries, which is beneficial in terms of aircraft weight reduction.

In case booms are required to ”make the connection” between the VTOL motors and the structure of the aircraft, this will imply drag penalties. Minimizing these drag penalties is important to achieve a more aerodynamically efficient configuration.

The location of the VTOL motors, together with the eventual booms, should also guarantee that no excessive twist and bending moments are passed to the structure of the aircraft. The vibration of the electric motors is also a problem and, stiffening the structure is required.

In order to achieve good control characteristics, the VTOL motors should not be placed too close to the CG. Furthermore, a minimum thrust-to-weight ratio of 1.5 should be used to guarantee the control and manoeuvrability of the aircraft [36].

2.4.2 Power calculations

Regarding the power calculations, Linear Momentum Theory is used. This is a very extensive theory and its detailed explanation can be found in [37].

During axial/vertical climb, the aircraft must respect the equilibrium equations 2.40 and 2.42. During axial/vertical descent, the aircraft must respect the equilibrium equations 2.41 and 2.42.

$$2 \cdot T_F + 2 \cdot T_R - 1.5 \cdot W - D_{aircraft} = 0 \tag{2.40}$$

$$2 \cdot T_F + 2 \cdot T_R - 1.5 \cdot W + D_{aircraft} = 0 \tag{2.41}$$

$$2 \cdot x_F \cdot T_F - 2 \cdot x_R \cdot T_R = 0 \tag{2.42}$$

, where T_F is the front rotor thrust, T_R is the rear rotor thrust, x_F is the distance between the front rotor and the aircraft CG, x_R is the distance between the rear rotor and the aircraft CG and, $D_{aircraft}$ is the aircraft drag. A thrust-to-weight ratio of 1.5 is also assumed [36].

Axial climb and hover

During axial/vertical climb, the power consumed by a rotor P_{c_i} can be given by equation 2.43 [37]:

$$P_{c_i} = T_i \cdot V_c - \frac{k_i}{2} \cdot T_i \cdot V_c + \frac{k_i \cdot T_i}{2} \cdot \sqrt{V_c^2 + \frac{2 \cdot T_i}{\rho \cdot A_i}} + \rho \cdot A_i \cdot V_{tip}^3 \cdot \frac{\sigma \cdot C_{d_0}}{8} \tag{2.43}$$

Neglecting the interference between all the 4 VTOL rotors, the total power consumed by the aircraft P_c during axial climb can be given by equation 2.44 [37]:

$$P_c = 4 \cdot P_{c_i} \tag{2.44}$$

Axial descent

During axial/vertical descent, the power consumed by a rotor P_{d_i} can be given by equation 2.45, if $V_d + 2 \cdot \sqrt{\frac{T_i}{2 \cdot \rho \cdot A_i}} < 0$ (windmill wake state) or by equation 2.46, if $V_d + 2 \cdot \sqrt{\frac{T_i}{2 \cdot \rho \cdot A_i}} > 0$ (vortex ring and turbulent wake states) [37]:

$$P_{d_i} = T_i \cdot V_d - \frac{k_i}{2} \cdot T_i \cdot V_d - \frac{k_i \cdot T_i}{2} \cdot \sqrt{V_d^2 - \frac{2 \cdot T_i}{\rho \cdot A_i}} + \rho \cdot A_i \cdot V_{tip}^3 \cdot \frac{\sigma \cdot C_{d_0}}{8} \tag{2.45}$$

$$P_{d_i} = T_i \cdot (V_d + k_i \cdot v_{h_i} - 1.125 \cdot v_{h_i} \cdot (\frac{V_d}{v_{h_i}}) - 1.372 \cdot v_{h_i} \cdot (\frac{V_d}{v_{h_i}})^2 - 1.718 \cdot v_{h_i} \cdot (\frac{V_d}{v_{h_i}})^3 - 0.655 \cdot v_{h_i} \cdot (\frac{V_d}{v_{h_i}})^4) + \rho \cdot A_i \cdot V_{tip}^3 \cdot \frac{\sigma \cdot C_{d_0}}{8} \tag{2.46}$$

, where $v_{h_i} = \sqrt{\frac{T_i}{2 \cdot \rho \cdot A_i}}$ is the rotor induced velocity.

Neglecting the interference between all the 4 VTOL rotors, the total power consumed by the aircraft P_d during axial descent can be given by equation 2.47 [37]:

$$P_d = 4 \cdot P_{d_i} \tag{2.47}$$

In equations 2.43 - 2.47, V_c is the climb speed, V_d is the descent speed, T_i is the thrust of rotor i, A_i is the area of rotor i and V_{tip} is the speed at the blade tip. Also note that, using equations 2.43 and 2.44,

the power consumed by the aircraft during hover is obtained when V_c = 0.

As for the other parameters in equations 2.43 - 2.47, the following must be noted:

- According to [37], rotor blade solidity σ has typical values between 0.07 and 0.12. A value of 0.1 is used in this design.
- According to [38], induced power correction factor k_i has a typical value of 1.15 in axial movement.
- According to [37], blade profile drag coefficient C_{d_0} has a typical value of 0.01.

2.4.3 Transition: power studies

According to [38], to formulate the equations necessary for aircraft sizing during the flight's transition mode, it is required to account for the following power terms: induced, profile, parasite and climb. The climb term is only needed if and only if there is a change in the aircraft's altitude during transition.

The aircraft sizing for the transition mode is based on modifying the sizing equations in rotorcraft mode rather than modifying the sizing equations in fixed-wing and have them meet the rotorcraft sizing in the middle-transition phase (as an alternative approach). The reason for selecting this approach is due to the fact that it was identified to have more accurate calculations of the required power compared to omitting some power terms in fixed-wing approach [38].

It was decided to perform the transition at a fixed altitude, hence no climb power is required. Assuming level transition flight, and for small angles of attack, the perpendicular component of forward flight velocity to the disc can be considered very small compared to the induced velocity at rotor disc. So, according to [38], the induced velocity at rotor disk can be obtained from the Linear Momentum Theory mentioned in [37].

The transition of the aircraft must respect the 3 equilibrium equations (vertical, horizontal and pitch moment equilibrium) 2.48 - 2.50 and the VTOL electric motors should only be switched off (thrust of the electric motors reduced to 0) once the stall speed of the aircraft is surpassed. The stall speed is obtained from the MATLAB code used to size the aircraft for cruise conditions (refer to subsection 2.3.4).

$$L_w + L_c + 2 \cdot T_F + 2 \cdot T_R - W = 0 \tag{2.48}$$

$$T_p - D_w - D_c - D_{fus} = 0 \tag{2.49}$$

$$M_{acw} + M_{acc} + x_c \cdot L_c - x_w \cdot L_w + 2 \cdot x_F \cdot T_F - 2 \cdot x_R \cdot T_R = 0 \tag{2.50}$$

, where all the relevant variables were already mentioned in previous sections.

The power of a front VTOL motor is given by equation 2.51, the power of a rear VTOL motor is given by equation 2.52 and the power of the pusher engine is given by equation 2.53. The total power used by the aircraft in transition is given by the sum of all the contributions, as expressed in equation 2.54 [38].

$$P_F = 2 \cdot k_i \cdot T_F \cdot v_{i_F} + \rho \cdot A_F \cdot V_{tip}^3 \cdot \frac{\sigma \cdot C_{d_0} \cdot (1 + 4.6 \cdot \mu^2)}{8} \tag{2.51}$$

$$P_R = 2 \cdot k_i \cdot T_R \cdot v_{i_R} + \rho \cdot A_R \cdot V_{tip}^3 \cdot \frac{\sigma \cdot C_{d_0} \cdot (1 + 4.6 \cdot \mu^2)}{8} \tag{2.52}$$

$$P_P = \frac{T_P \cdot V}{\eta_p} \tag{2.53}$$

$$P_{transition} = 2 \cdot P_F + 2 \cdot P_R + P_P \tag{2.54}$$

, where the induced power correction factor k_i has a typical value of 1.2 in forward movement [38], μ is the advance ratio, v_{i_F} is the induced velocity of the front rotor and v_{i_R} is the induced velocity of the rear rotor. v_{i_F} and v_{i_R} are given by equations 2.55 and 2.56, respectively [38].

$$v_{i_F} = \sqrt{-\frac{V^2}{2} + \sqrt{\frac{V^4}{4} + \frac{T_F^2}{4 \cdot \rho^2 \cdot A_F^2}}} \tag{2.55}$$

$$v_{i_R} = \sqrt{-\frac{V^2}{2} + \sqrt{\frac{V^4}{4} + \frac{T_R^2}{4 \cdot \rho^2 \cdot A_R^2}}} \tag{2.56}$$

Making use of the previous equations and for different forward velocities, it is possible to estimate the aircraft angle of attack α and the canard angle of incidence i_c that guarantee a trim condition, as well as the thrust of the electric motors (T_F and T_R), the pusher engine thrust T_p, the lift of the aircraft and, the power consumed by the electric motors (P_F and P_R) and by the pusher engine P_P in quasi-static conditions. These output will give a good picture of the evolution of forces and powers necessary to perform the transition.

2.5 Aircraft Performance Analysis

2.5.1 Final CFD analysis: aerodynamics and static stability

After obtaining a final configuration for the aircraft, already optimized for cruise and with the VTOL architecture incorporated, a final CFD analysis is performed in order to assess its aerodynamic and stability properties.

The theoretical details regarding the CFD analysis were already mentioned in subsection 2.3.2 when addressing the Navier-Stokes equations.

2.5.2 Dynamic stability

Dynamic stability refers to the characteristics of an aircraft that, when disturbed from an original state of steady flight or motion, allow it to damp the oscillations using its inherent restoring moments and gradually return to its original state [39].

To characterize the dynamics of an aircraft, two reference frames are generally used: the earth-fixed frame (inertial) and the body-fixed frame (moving). Regarding the earth-fixed frame, Earth curvature is neglected and gravity acceleration is assumed to be vertical. Regarding the body-fixed frame, the origin is set at the aircraft center of mass [40].

The Euler angles (ϕ, θ and ψ) are used to relate the linear and angular velocities of both reference frames. The relationship between the earth-fixed frame linear velocity $\vec{V_E}$ and the body-fixed frame linear velocity $\vec{V_B}$ is given by equation 2.57. The relationship between the earth-fixed frame angular velocity $\vec{\omega_E}$ and the body-fixed frame angular velocity $\vec{\omega_B}$ is given by equation 2.58 [40].

$$\vec{V_B} = \begin{bmatrix} cos(\theta)cos(\psi) & cos(\theta)sin(\psi) & -sin(\theta) \\ sin(\phi)sin(\theta)cos(\psi) - cos(\phi)sin(\psi) & sin(\phi)sin(\theta)sin(\psi) + cos(\phi)cos(\psi) & sin(\phi)cos(\theta) \\ cos(\phi)sin(\theta)cos(\psi) + sin(\phi)sin(\psi) & cos(\phi)sin(\theta)sin(\psi) - sin(\phi)cos(\psi) & cos(\phi)cos(\theta) \end{bmatrix} \cdot \vec{V_E} \tag{2.57}$$

$$\vec{\omega_B} = \begin{bmatrix} 1 & 0 & -sin(\theta) \\ 0 & cos(\phi) & sin(\phi)cos(\theta) \\ 0 & -sin(\phi) & cos(\phi)cos(\theta) \end{bmatrix} \cdot \vec{\omega_E} \tag{2.58}$$

Equations 2.59 and 2.60 show how the aircraft dynamic model is obtained from the application of Newton's Second Law to rigid bodies [40].

$$\sum \vec{F} = m \cdot (\dot{\vec{V_B}} + \vec{\omega_B} \times \vec{V_B}) \tag{2.59}$$

$$\sum \vec{M} = I \cdot \dot{\vec{\omega_B}} + \vec{\omega_B} \times I \cdot \vec{\omega_B} \tag{2.60}$$

, where m is the aircraft mass, I is the aircraft inertia matrix, $\vec{V_B} = (u, v, w)$ and $\vec{\omega_B} = (p, q, r)$. Furthermore, $\sum \vec{F} = F_a + F_g + F_c = (X, Y, Z)$ and $\sum \vec{M} = M_a + M_g + M_c = (\mathcal{L}, M, N)$ represent the total forces and moments acting on the aircraft, respectively. The subscripts a, g and c refer to the aerodynamic, gravity and control forces/moments, respectively [40].

The control forces/moments include the deflection of the control surfaces (aileron and rudder), the variation of the canard incidence angle and, the thrust from the electric motors and pusher engine. However, the control terms do not affect the dynamic stability analysis of the aircraft (only its control). The aerodynamic forces and moments are given by equations 2.61 and 2.62, respectively [40].

$$\begin{bmatrix} X_a \\ Y_a \\ Z_a \end{bmatrix} = \begin{bmatrix} X_u \cdot u + X_w \cdot w + X_{\dot{w}} \cdot \dot{w} + X_q \cdot q \\ Y_v \cdot v + Y_p \cdot p + Y_r \cdot r \\ Z_u \cdot u + Z_w \cdot w + Z_{\dot{w}} \cdot \dot{w} + Z_q \cdot q \end{bmatrix} \tag{2.61}$$

$$\begin{bmatrix} L_a \\ M_a \\ N_a \end{bmatrix} = \begin{bmatrix} L_v \cdot v + L_p \cdot p + L_r \cdot r \\ M_u \cdot u + M_w \cdot w + M_{\dot{w}} \cdot \dot{w} + M_q \cdot q \\ N_v \cdot v + N_p \cdot p + N_r \cdot r \end{bmatrix} \tag{2.62}$$

The dynamic stability of the aircraft is studied through the linearization of equations 2.57 - 2.60 around a certain steady-state condition. All dynamic variables are given by the sum of its steady-state value with its small perturbation.

In the case of this aircraft, the dynamic analysis will be performed for VTOL, transition and forward flight stages. For these conditions, no steady-state lateral velocity ($v_0 = 0$), no steady-state angular velocities ($p_0 = q_0 = r_0 = 0$) and no steady-state Euler angles are considered ($\phi_0 = \theta_0 = \psi_0 = 0$). Since stability axis are being used for the current analysis, $\alpha_0 = 0$ [40]. The steady-state velocities u_0 and w_0 vary with the flight condition. Due to symmetry, the aircraft motion can be decoupled and separately studied from a longitudinal and a lateral point of view [40].

The linearization of the longitudinal motion of the aircraft yields equation 2.63:

$$\begin{bmatrix} \dot{u} \\ \dot{w} \\ \dot{q} \\ \dot{\theta} \end{bmatrix} = \begin{bmatrix} \frac{X_u}{m} & \frac{X_w}{m} & -w_0 & -g \\ \frac{Z_u}{m - Z_{\dot{w}}} & \frac{Z_w}{m - Z_{\dot{w}}} & \frac{Z_q + m \cdot u_0}{m - Z_{\dot{w}}} & 0 \\ \frac{M_u + \frac{M_{\dot{w}} \cdot Z_u}{m - Z_{\dot{w}}}}{I_{yy}} & \frac{M_w + \frac{M_{\dot{w}} \cdot Z_w}{m - Z_{\dot{w}}}}{I_{yy}} & \frac{M_q + \frac{M_{\dot{w}} \cdot (Z_q + m \cdot u_0)}{m - Z_{\dot{w}}}}{I_{yy}} & 0 \\ 0 & 0 & 1 & 0 \end{bmatrix} \cdot \begin{bmatrix} u \\ w \\ q \\ \theta \end{bmatrix} \tag{2.63}$$

The linearization of the lateral motion of the aircraft yields equation 2.64:

$$\begin{bmatrix} \dot{v} \\ \dot{p} \\ \dot{r} \\ \dot{\phi} \end{bmatrix} = \begin{bmatrix} \frac{Y_v}{m} & \frac{Y_p}{m} + w_0 & \frac{Y_r}{m} - u_0 & g \\ L_v / I_{xx} + I_{xz} \cdot N_v & L_p / I_{xx} + I_{xz} \cdot N_p & L_r / I_{xx} + I_{xz} \cdot N_r & 0 \\ N_v / I_{zz} + I_{xz} \cdot L_v & N_p / I_{zz} + I_{xz} \cdot L_p & N_r / I_{zz} + I_{xz} \cdot L_r & 0 \\ 0 & 1 & 0 & 0 \end{bmatrix} \cdot \begin{bmatrix} v \\ p \\ r \\ \phi \end{bmatrix} \tag{2.64}$$

Expressions for all the derivatives X_u, X_w, Z_u, Z_w, $Z_{\dot{w}}$, Z_q, M_u, M_w, $M_{\dot{w}}$, M_q, Y_v, Y_p, Y_r, L_v, L_p, L_r, N_v, N_p and N_r can be found in Appendix A.

The aircraft is dynamically stable if it is both longitudinally and laterally stable. The aircraft is longitudinally stable if all eigenvalues of the 4x4 matrix of equation 2.63 have negative real parts. The aircraft is laterally stable if all eigenvalues of the 4x4 matrix of equation 2.64 have negative real parts.

2.5.3 Pusher propeller: fixed-pitch vs variable-pitch

A propeller transmits power by converting rotational motion into thrust. The design point of the propeller should be for cruise condition, so as to have an efficiency as high as possible at this flight condition. The selection of the piston engine and pusher propeller is related to each other, since the combined overall

performance determines the good design of the propulsive system.

An important trade-off study between having a fixed-pitch and a variable-pitch propellers is conducted. Compared to a fixed-pitch propeller, a variable-pitch propeller contains more parts, many of them moving, and it would be unrealistic to expect that there is no extra risk entailed in installing variable-pitch propellers rather than fixed-pitch propellers. Also, these moving parts mean more vibration, noise and cavitation [41]. However, by using a variable-pitch propeller, the maximum speed of the aircraft can be increased [42] and the search area can be reached in less time (dash time). Figure 2.9 shows curves of propeller efficiency η_p versus advance ratio J for different propeller pitches.

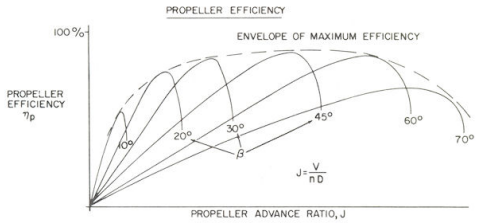

Figure 2.9: Efficiency of a propeller as a function of the advance ratio [42]

For a given propeller pitch, there is always a point of maximum efficiency (the target when sizing the propeller for cruise) and once the forward speed (and thus, the advance ratio) is decreased or increased, the propeller efficiency drops. If a fixed-pitch propeller is used, the drop can be considerable and the solution to attenuate this drop is to use a variable-pitch propeller. By having a variable-pitch propeller, the propeller can operate at the envelope of maximum efficiency, which means less power consumption and, therefore, the aircraft can achieve higher maximum speeds and better efficiency at lower speeds.

To quantitatively study and compare the difference in aircraft maximum forward speed when using a fixed-pitch or a variable-pitch propellers, it is necessary to compute the real power P_{real} spent by the aircraft for a given forward speed. P_{real} is given, as function of ideal power P_{ideal} and propeller efficiency η_p, by:

$$P_{real} = \frac{P_{ideal}}{\eta_p} \tag{2.65}$$

The maximum speed is achieved when the real power P_{real} is equal to the engine installed power.

Chapter 3

Aircraft Design - Implementation and Results

3.1 Preliminary Design

3.1.1 Numerical implementation of the geometry optimization code

In order to have a first estimate of the most suitable aircraft configuration, the geometry optimization code mentioned in subsection 2.3.4 is used. The aircraft is designed to achieve a good aerodynamic performance and stability when in cruise. The most suitable geometry for both the wing and canard, as well as the most suitable location of the lifting surfaces with respect to the fuselage is optimized.

The aerodynamic properties of the selected wing and canard airfoils as a function of Re are stored in a separate file. The data in this file is used by the code during the optimization process.

The code estimates the aerodynamic behaviour of the lifting surfaces through the Lifting Line Theory equations. Once chord and twist distributions are known, equation 2.5 is solved by the code for different angles of attack α. According to [29], equation 2.5 can be easily solved by converting it into a system of algebraic equations. This is done by using the transformation of coordinates of figure 3.1.

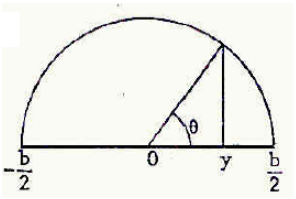

$$\cos(\theta) = \frac{2y}{b}$$

$$dy = -\frac{b\,\mathrm{sen}(\theta)}{2} d\theta$$

Figure 3.1: Transformation of coordinates used in the Lifting Line Theory

Equation 2.5 is then transformed into equation 3.1.

$$\alpha + \theta_t(\theta) = \frac{2 \cdot \Gamma(\theta)}{C'_{l\infty}(\theta) \cdot V_\infty \cdot c(\theta)} - \beta(\theta) + \frac{1}{4\pi \cdot V_\infty} \int_0^\pi \frac{2}{b \cdot (cos(\theta') - cos(\theta))} \frac{d\Gamma}{d\theta'} d\theta' \tag{3.1}$$

According to [29], the circulation $\Gamma(\theta)$ can be given by equation 3.2.

$$\Gamma(\theta) = \sum_{n=1,3,...}^{\infty} \Gamma_n \cdot sen(n\theta) \tag{3.2}$$

Combining equations 3.1 and 3.2, the code assesses the aerodynamic performance of the lifting surfaces by solving the system of algebraic equations 3.3.

$$\sum_{n=1,3,...}^{2N-1} \Gamma_n \cdot (\frac{2 \cdot sen(n\theta_i)}{C'_{l\infty}(\theta_i) \cdot V_\infty \cdot c(\theta_i)} + \frac{n \cdot sen(n\theta_i)}{2 \cdot b \cdot V_\infty \cdot sen(\theta_i)}) = \alpha + \theta_t(\theta_i) + \beta(\theta_i) \tag{3.3}$$

, where N is the number of terms used in the series and $\theta_i = i\frac{\pi}{2N}$, with $i = 1, 2, ..., N$. Once the coefficients Γ_n are determined, C_L is found from equation 3.4 and C_D is found from equation 3.5 [29].

$$C_L = \frac{\pi}{2 \cdot V_\infty \cdot \bar{c}} \cdot \Gamma_1 \tag{3.4}$$

$$C_D = \frac{C_L^2 \cdot \bar{c}}{\pi \cdot b} \sum_{n=1,2,...}^{N} \frac{(2n-1) \cdot \Gamma_n^2}{\Gamma_1^2} + \frac{1}{b} \cdot \int_{-b/2}^{b/2} C_{D_{airfoil}}(y)dy \tag{3.5}$$

The fuselage is designed to fit the internal components and its aerodynamic drag evolution with α (see figure 3.10) is considered in the code.

For a certain forward speed V, the optimization statement is as follows:

$$\min_{x} \quad T_p(x) \cdot V \tag{3.6a}$$

subject to

$$L_w(x) + L_c(x) - W = 0 \tag{3.6b}$$

$$T_p(x) - D_w(x) - D_c(x) - D_{fus}(x) = 0 \tag{3.6c}$$

$$M_{acw}(x) + M_{acc}(x) + x_c \cdot L_c(x) - x_w \cdot L_w(x) = 0 \tag{3.6d}$$

$$9.8 \leq \frac{x_w \cdot a_w(x) \cdot S_w(x) - x_c \cdot a_c(x) \cdot S_c(x)}{\bar{c}_w(x) \cdot (a_w(x) \cdot S_w(x) + a_c(x) \cdot S_c(x))} \cdot 100 \leq 10.2 \tag{3.6e}$$

$$V_{stall} \leq 20 \tag{3.6f}$$

$$|\alpha| \leq 10^{\circ} \tag{3.6g}$$

$$|\alpha + i_c| \leq 10^{\circ} \tag{3.6h}$$

$$0.75 \leq \frac{L_w(x)}{L_w(x) + L_c(x)} \leq 0.8 \tag{3.6i}$$

$$b_w \leq 4 \tag{3.6j}$$

x = [α, i_c, b_w, $c_w(y)$, $\theta_w(y)$, b_c, $c_c(y)$, $\theta_c(y)$, x_w, x_c, α_{stall}, i_{cstall}, V_{stall}] is the set of design variables.

To perform the optimization statement shown above, the MATLAB code uses the *fmincon* function. *fmincon* aims at finding the minimum of a constrained nonlinear multivariable function [43].

In this case, the MATLAB code uses the *fmincon* function to find the aircraft geometry, angle of attack α and canard incidence angle i_c that minimize the ideal power consumed by the aircraft for a certain forward velocity (equation 3.6a). The constraints are the equilibrium equations (equations 3.6b - 3.6d),

a static margin in cruise around 10% (equation 3.6e), a maximum stall speed of 20 m/s (equation 3.6f) and, a maximum angle of attack for both the wing and canard limited to 10º (equations 3.6g and 3.6h). A ratio of 75% - 80% between wing lift and aircraft lift in cruise is also intended (equation 3.6i) and, due to space constraints in a ship, the maximum acceptable wingspan is 4 m (equation 3.6j).

The MATLAB code is able to determine the aircraft stall speed by finding the minimum forward speed at which the equilibrium equations are still satisfied, while keeping the angle of attack of both the wing and canard limited to 10º, as can be seen in equations 3.7a - 3.7h.

$$\min_{x} \quad V_{stall} \tag{3.7a}$$

$$\text{subject to} \quad V_{stall} \leq 20 \tag{3.7b}$$

$$|\alpha_{stall}| \leq 10^{\circ} \tag{3.7c}$$

$$|\alpha_{stall} + i_{cstall}| \leq 10^{\circ} \tag{3.7d}$$

$$L_{w\_stall}(x) + L_{c\_stall}(x) - W = 0 \tag{3.7e}$$

$$T_{p\_stall}(x) - D_{w\_stall}(x) - D_{c\_stall}(x) - D_{fus\_stall}(x) = 0 \tag{3.7f}$$

$$M_{acw\_stall}(x) + M_{acc\_stall}(x) + x_c \cdot L_{c\_stall}(x) - x_w \cdot L_{w\_stall}(x) = 0 \tag{3.7g}$$

$$b_w \leq 4 \tag{3.7h}$$

x = [α, i_c, b_w, $c_w(y)$, $\theta_w(y)$, b_c, $c_c(y)$, $\theta_c(y)$, x_w, x_c, α_{stall}, i_{cstall}, V_{stall}] is the set of design variables.

The obtention of the most suitable aircraft geometry is an iterative process (which not only takes into consideration aerodynamic issues, but also magnetic signature, structural, vibration and control constraints) and, for convenience, only the final results are presented.

3.1.2 Wing and canard airfoils

Selecting suitable airfoils for the lifting surfaces is a first step in the design of the aircraft. To characterize the aerodynamic behaviour of different airfoils, XFOIL software is used (refer to subsection 2.3.1). In [44], coordinates that define the shape of different airfoils are found and inputted in the software. Operational characteristics such as air viscosity ν, Reynolds number Re and a range of angles of attack α are then defined and, the software computes the aerodynamic coefficients Cl, Cd and Cm for the different α.

The airfoils of the wing and the canard must respect the following conditions:

- Lift-to-drag maximization. This is a common design characteristic and has the goal of providing the best aerodynamic performance for the airfoils and, thus, for the lifting surfaces and for the aircraft
- In a canard configuration, if the wing stalls before the canard, irrecoverable aircraft pitch-up moment occurs. Thus, to avoid this situation, it is necessary to guarantee that the canard stalls before the wing [45]
- Stall proofing requires the stall angle of the canard to be smaller than the stall angle of the wing. One way to accomplish so is to have the canard airfoil more cambered than the wing airfoil [45]

The obtained wing has a $\bar{Re} = 8.33333 \times 10^5$ (refer to subsection 3.1.3) and the obtained canard has a $\bar{Re} = 4.28571 \times 10^5$ (refer to subsection 3.1.4). For these values of $\bar{Re}$, figure 3.2 provides comparisons between the aerodynamic characteristics of different airfoils from the NACA family and, shows why a NACA 2412 for the wing and a NACA 4412 for the canard are the most adequate airfoil solutions among those analysed.

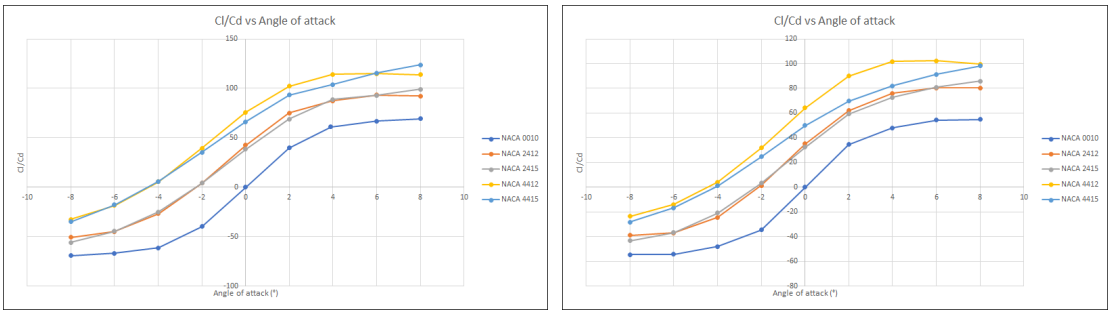

Figure 3.2: Left image: Wing airfoil comparison at $\bar{Re} = 8.33333 \times 10^5$. Right image: Canard airfoil comparison at $\bar{Re} = 4.28571 \times 10^5$

Regarding the canard, the airfoil that maximizes L/D for expected angle of attack values in cruise conditions (low values, close to 0) is the NACA 4412 and it is therefore selected.

Regarding the wing and, due to the stall requirements already mentioned, its airfoil must be less cambered than the canard airfoil. Given this fact, NACA 4412 and 4415 airfoils are ruled out of selection. Within the remaining airfoils, NACA 2412 is the airfoil that maximizes L/D for expected angle of attack values in cruise conditions (low values, close to 0) and it is therefore selected.

3.1.3 Wing design

The wing obtained has a span b_w of 3.67 m and a mean chord $\bar{c}_w$ of 0.35 m. The chord distribution is as follows: first, from the wing root till the section at 52.5% of the wing semi-span, the chord is kept constant and is equal to 0.3974 m; then, from the section at 52.5% of the wing semi-span till the wing tip, there is a linear decrease in the chord. The chord has a value of 0.3974 m at the section at 52.5% of the wing semi-span and a value of 0.1888 m at the tip of the wing. By dividing the tip chord by the root chord, a taper ratio of 0.475 is obtained for the wing.

The twist distribution is as follows: first, from the wing root till the section at 82.5% of the wing semi-span, there is a linear decrease in the twist, which varies from 0º to -0.5º; then, from the section at 82.5% of the wing semi-span till the wing tip, there is a more pronounced linear decrease in the twist, which varies from -0.5º to -1.25º. Therefore, the root has a higher angle of incidence than the tip (washout), meaning that the aircraft stalls at the root first and there's enough airflow over the tips of the wings to prevent any rapid rolling motion during a stall, which makes the airplane more stable and more resistant to entering a spin [46]. On top of that, a root stall also guarantees some aileron effectiveness during the stall, giving a greater control of the aircraft [46].

The summary of the geometric properties of the wing are presented in tables 3.1 and 3.2. The wing planform is shown in figure 3.3.

Parameter	Value
Wingspan	3.67 m
Mean chord	0.35 m

Table 3.1: Wingspan and mean chord

Parameter	Value	Parameter	Value
Root chord	0.3974 m	Root twist	0º
Chord at 52.5% of the wing semi-span	0.3974 m	Twist at 82.5% of the wing semi-span	-0.5º
Tip chord	0.1888 m	Tip twist	-1.25º

Table 3.2: Wing chord and twist distributions

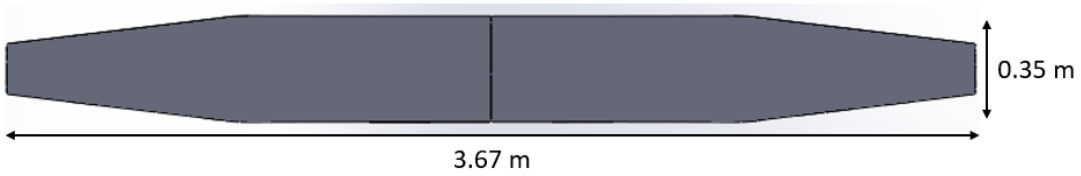

Figure 3.3: Wing geometry

The aerodynamic characteristics of the wing were first obtained with the Lifting Line Theory equations used in the optimization algorithm. The aerodynamic characteristics were then compared with two other theories: Panel Method and Navier-Stokes numerical solution (CFD). A trend agreement between the results from all the 3 theories can be witnessed below (wing area is the reference area).

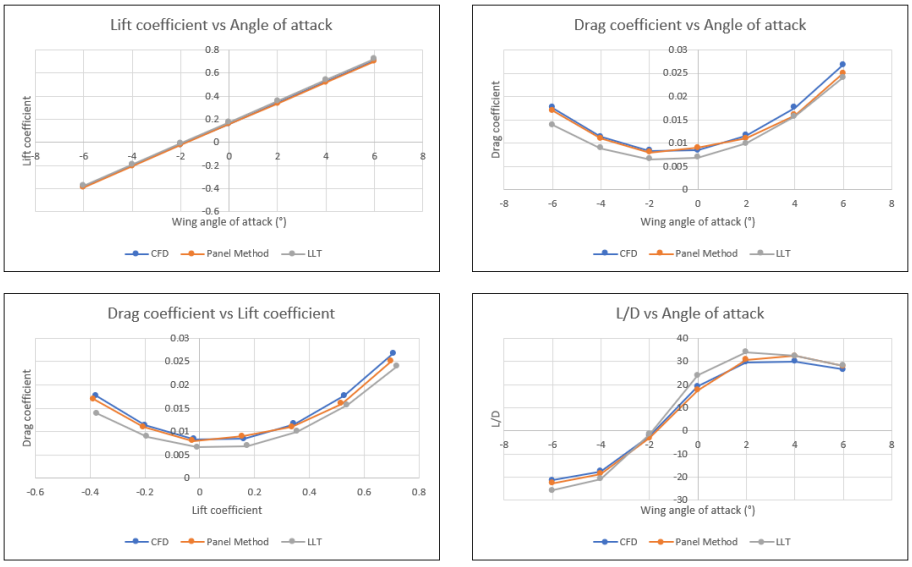

Figure 3.4: Comparison between results from Lifting Line Theory, Panel Method and CFD analysis

As for the lift coefficient variation with the angle of attack, very similar results are estimated by the 3 theories. As for the drag coefficient variation with the angle of attack, some discrepancies exist between

the results estimated by the 3 theories, likely due to the drag models used to assess the friction drag and the boundary layer effect.

Table 3.3 compares the estimated values for the wing lift coefficient slope C_{L_α} and zero-lift drag coefficient C_{D_0} when using CFD, LLT and empirical equations. Regarding the empirical equations, C_{L_α} is given by equation 3.8 and C_{D_0} is given by equation 3.9 [47]. Wing area is used as reference area to compute the values in table 3.3.

$$C_{L_\alpha} = \frac{2 \cdot \pi \cdot AR}{2 + \sqrt{4 + AR^2}} \tag{3.8}$$

$$C_{D_0} = C_f \cdot F \cdot Q \cdot \frac{S_{wet}}{S} \tag{3.9}$$

, where AR is the lifting surface aspect ratio, C_f is the viscous drag coefficient, F is the form factor, Q is the interference factor, S_{wet} is the lifting surface wetted area and S is the lifting surface area.

Parameter	CFD	LLT	Difference	Empirical	Difference
C_{L_α}	0.0907/º	0.0914/º	0.77 %	0.0907/º	0 %
C_{D_0}	0.0085	0.0065	23.53 %	0.0095	11.76 %

Table 3.3: Comparison between CFD, LLT and empirical results for wing C_{L_α} and C_{D_0}

From table 3.3, in terms of C_{L_α}, the estimations obtained with CFD and empirical approaches yield the same value. The LLT approach yields a C_{L_α} estimation 0.77 % higher. In terms of C_{D_0}, the CFD estimation is 23.53 % higher than the LLT estimation and 11.76 % smaller than the empirical estimation.

3.1.4 Canard design

The canard obtained is rectangular and untwisted, as shown in figure 3.5. The canard has a span b_c of 1.71 m and a chord c_c of 0.18 m.

Parameter	Value
Span	1.71 m
Chord	0.18 m

Table 3.4: Canard span and mean chord

Figure 3.5: Canard geometry

The aerodynamic characteristics of the canard were first obtained with the Lifting Line Theory equations used in the optimization algorithm. The aerodynamic characteristics were then compared with two

other theories: Panel Method and Navier-Stokes numerical solution (CFD). A trend agreement between the results from all the 3 theories can be witnessed below (canard area is the reference area).

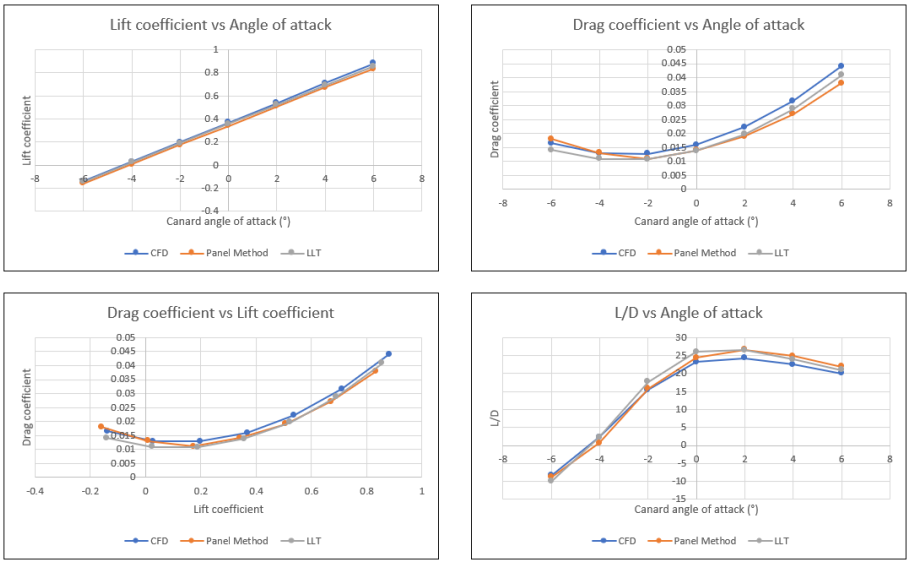

Figure 3.6: Comparison between results from Lifting Line Theory, Panel Method and CFD analysis

The canard results show similar behaviour as for the wing.

Table 3.5 compares the estimated values for the canard lift coefficient slope C_{L_α} and zero-lift drag coefficient C_{D_0} when using CFD, LLT and empirical equations. Regarding the empirical equations, C_{L_α} is given by equation 3.8 and C_{D_0} is given by equation 3.9 [47]. In table 3.5, canard area is used as reference area to compute C_{L_α}, while wing area is used as reference area to compute C_{D_0}.

Parameter	CFD	LLT	Difference	Empirical	Difference
C_{L_α}	0.0851/º	0.0831/º	2.35 %	0.0890/º	4.58 %
C_{D_0}	0.0032	0.0027	15.63 %	0.0029	9.38 %

Table 3.5: Comparison between CFD, LLT and empirical results for canard C_{L_α} and C_{D_0}

From table 3.5, in terms of C_{L_α}, the CFD estimation is 2.35 % higher than the LLT estimation and 4.58 % smaller than the empirical estimation. In terms of C_{D_0}, the CFD estimation is 15.63 % higher than the LLT estimation and 9.38 % higher than the empirical estimation.

In the code used for the preliminary design of the aircraft, the aerodynamic properties of the lifting surfaces are estimated by means of the Lifting Line Theory instead of CFD. Although less accurate, LLT provides analytical equations and avoids the need of developing CAD models and running CFD simulations for different geometries of the lifting surfaces, reducing significantly the workload and time of the process. From figures 3.4 and 3.6 and, from tables 3.3 and 3.5, LLT and CFD estimate close values for the lift properties, however as for the drag properties, LLT underestimates the total drag of the lifting surfaces, since the viscous drag contribution is not so well taken into consideration when compared to CFD. Nevertheless, for a preliminary sizing, LLT is still preferred due to its simplicity, with a more detailed analysis, namely in what regards the viscous drag contribution, being performed with CFD later.

3.1.5 Fuselage design

The fuselage must fulfill two types of requirements: functional (capable of fitting all internal components) and aerodynamic (be as smooth and low-drag as possible).

In terms of functional aspects, the biggest internal components of the aircraft are expected to be the MAD-XR sensor (placed at the front of the fuselage) and the piston engine (placed at the back of the fuselage). The former has dimensions clearly defined, however the dimensions of the latter depend on existing models in the market. A detachable payload pod to fit the MAD-XR sensor and eventually other type of payload in the future is also taken into consideration.

In terms of aerodynamic aspects, inflexion points in the exterior of the fuselage promote turbulence in the boundary layer [29], thus increasing the drag of the fuselage. Hence, inflexion points in the exterior of the fuselage should be avoided as maximum as possible.

A fuselage was designed with the help of SolidWorks software. In figures 3.7, 3.8 and 3.9, the general dimensions and cross-section shape are depicted.

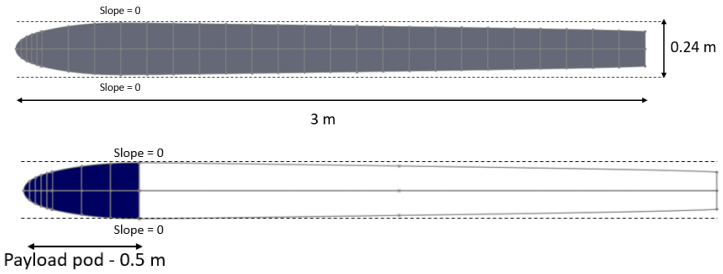

Figure 3.7: Top image: Dimensions of the fuselage. Bottom image: Payload pod

Figure 3.8: Longitudinal view of the fuselage with the MAD-XR sensor included

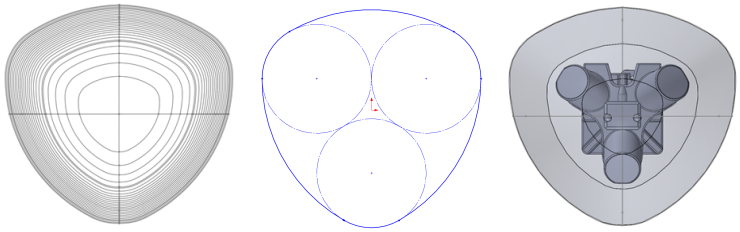

Figure 3.9: Left image: Cross-section view of the fuselage. Middle image: Cross-section shape of the fuselage. Right image: Cross-section view of the fuselage with the MAD-XR sensor included

As can be witnessed from the above figures, the fuselage is 3 m long and has a maximum diameter of 0.24 m. A length of 3 m guarantees that the distance between pusher engine and MAD-XR sensor is in accordance with the set requirements (refer to table 1.2). The payload pod is 0.5 m long and, since it is meant to be detachable, the local slope at the point of attachment/detachment with the rest of the fuselage is made to be 0 so as to ease all the process of attaching and removing it.

The cross-section shape is inspired by the geometry of the MAD-XR sensor. This can be clearly understood by inspection of figure 3.9, where it can be seen that the three inner circles are based on the disposition of the three scalar magnetometers of the MAD-XR sensor.

During the process of designing the fuselage in Solidworks, its curvature combs were taken into account to check the existence of inflexion points. A more accurate estimation of the drag of the fuselage as function of the angle of attack was then performed with the help of CFD. The results are plotted in figure 3.10 (wing area is used as reference area).

Table 3.6 compares the estimated values for the fuselage base drag coefficient C_{D_0} when using CFD and when using empirical equations. Regarding the empirical equations, C_{D_0} is given by equation 3.9 [47]. Wing area is used as reference area to compute the values in table 3.6.

From table 3.6, in terms of C_{D_0}, the CFD estimation is 5.88 % higher than the empirical estimation.

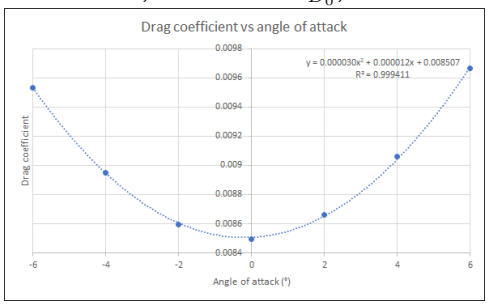

Figure 3.10: Fuselage drag coefficient variation with angle of attack

Parameter	CFD	Empirical	Difference
C_{D_0}	0.0085	0.0080	5.88 %

Table 3.6: Comparison between CFD and theoretical results for fuselage C_{D_0}

3.1.6 Vertical fins design

After a first geometry was obtained for the wing, canard and fuselage so as to guarantee equilibrium and longitudinal stability, it is important to take a look at the lateral stability of the aircraft. In particular, it is necessary to have a first estimate of the dimensions of the vertical fins. In subsection 2.3.5, the method used to obtain a first sizing of the vertical fins was introduced.

A study is conducted to analyse how wing sweep influences the dimensions of the vertical fins necessary to obtain $C_{N\beta} = 0.0571/rad$ (this value is explained in subsection 2.3.5), but also the aerodynamics of the wing. 3 different wing configurations are considered: the wing obtained in figure 3.3 (used as reference in this study), a wing with 0º leading edge sweep and a wing with 0º trailing edge sweep. This study allows to choose the wing configuration to be used in the aircraft.

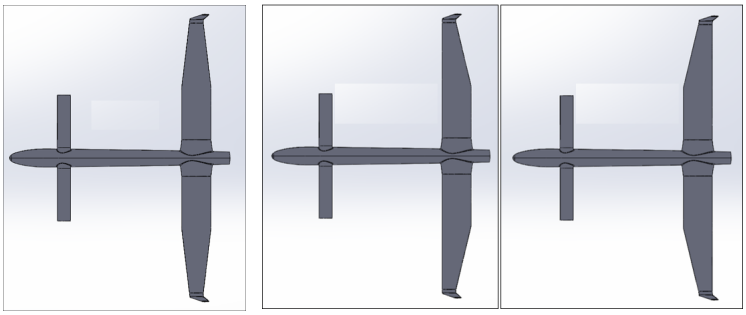

Figure 3.11: Left image: Reference wing. Middle image: Wing with 0º leading edge sweep. Right image: Wing with 0º trailing edge sweep

Using the equations from subsection 2.3.5, the area of the vertical fins/winglets necessary to obtain $C_{N\beta} = 0.0571/rad$ is computed. According to [48], for aerodynamic efficiency, the winglets must be tapered in the same way of the wing. Having information about the area, root chord (same as the wing tip chord) and taper ratio, the height of the vertical fins is calculated. The dimensions of the vertical fins associated with the 3 different wing geometries are compared in table 3.7.

Wing geometry	**Fin area (m^2)**	**Fin height (m)**
Wing with 0º leading edge sweep	0.0968	0.6955
Reference wing	0.0794	0.5704
Wing with 0º trailing edge sweep	0.0673	0.4835

Table 3.7: Vertical fins dimensions vs wing sweep

The wing with 0º trailing edge sweep yields the smallest values for the area and height of the fins. This is explained by the fact that, with this wing configuration, the distance between the aircraft CG and the aerodynamic center of the fins is bigger, requiring thus less force to be generated to obtain the same yaw moment. A smaller force means a smaller area and, consequently, a smaller height for the fins. A smaller size of the vertical fins is structurally beneficial.

The aerodynamic performance, namely, the lift-to-drag ratio of the reference wing and of the wing with 0º trailing edge sweep for different angles of attack are compared in figure 3.12.

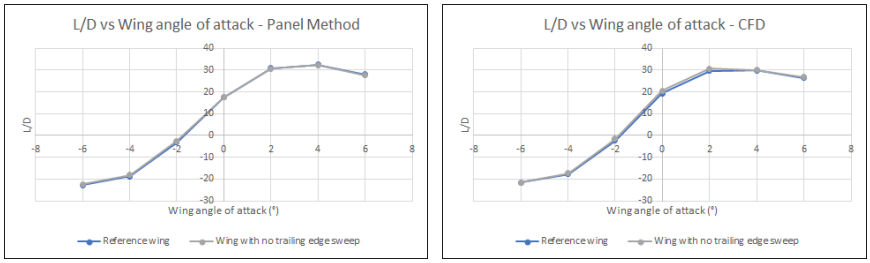

Figure 3.12: Lift-to-drag ratio - Reference wing vs Wing with 0º trailing edge sweep

From figure 3.12, the wing aerodynamic performance is not significantly affected by having 0º sweep at the trailing edge. Furthermore, since this also allows a reduction in the size of the vertical fins, which is structurally beneficial, a wing with 0º trailing edge sweep is used in this UAV.

3.1.7 Preliminary CAD Model and Aircraft Performance

The optimization code (explained in subsection 3.1.1) was used to obtain different aircraft configurations, each one optimized for a certain forward/possible cruise speed. A MTOW = 35 Kg was assumed.

3 possible aircraft configurations were obtained, respectively optimized for the forward speeds of 30 m/s, 35 m/s and 40 m/s. As for the forward speeds of 45 m/s and 50 m/s, optimizations were also carried out, however the optimization code could not satisfy all the constraints, thus no solutions were obtained.

In table 3.8, the wingspan, wing mean chord, canard span and canard chord of the 3 optimized configurations are presented. In figures 3.13 - 3.16, plots representing the important output obtained

from the optimization algorithm are presented. The aircraft angle of attack α / wing angle of attack α_w (as a first approximation, the wing incidence angle $_{1_w}$ is assumed to be 0) and canard angle of attack α_c to guarantee trim condition are represented in figure 3.13. The ratio between wing lift and aircraft lift, ratio between canard lift and aircraft lift and, static margin of the aircraft are represented in figure 3.14. The thrust and ideal power required to move the aircraft forward are represented in figure 3.15. The lift-to-drag ratio of the aircraft is represented in figure 3.16.

Parameter	Configuration 1 - 30 m/s	Configuration 2 - 35 m/s	Configuration 3 - 40 m/s
b_w	4 m	3.67 m	3.3 m
$\bar{c}_w$	0.37 m	0.35 m	0.34 m
b_c	1.84 m	1.71 m	1.58 m
c_c	0.19 m	0.18 m	0.17 m

Table 3.8: Wingspan, wing mean chord, canard span and canard chord of the optimized configurations

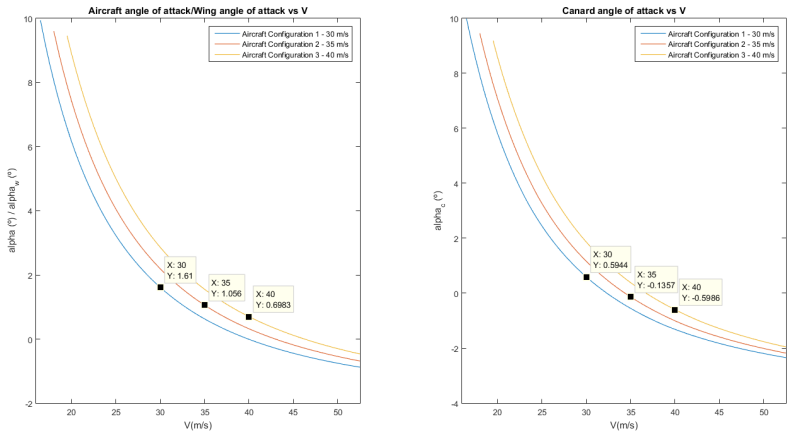

Figure 3.13: Aircraft angle of attack/wing angle of attack and canard angle of attack for the 3 optimized configurations

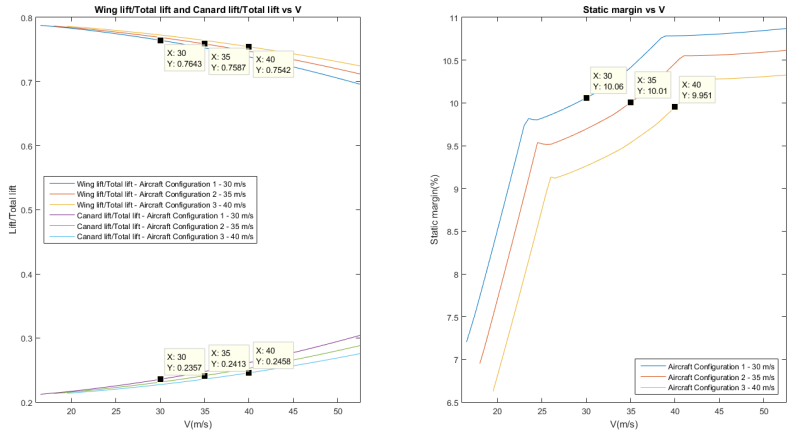

Figure 3.14: Wing lift/aircraft lift, canard lift/aircraft lift and aircraft static margin for the 3 optimized configurations

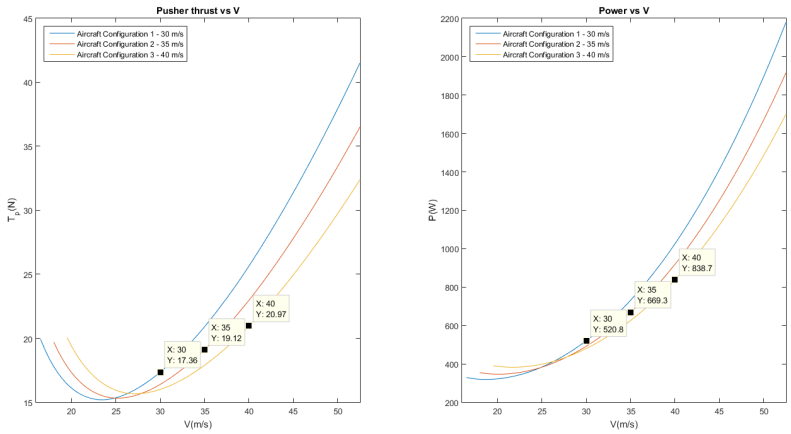

Figure 3.15: Thrust and ideal power required for the 3 optimized configurations

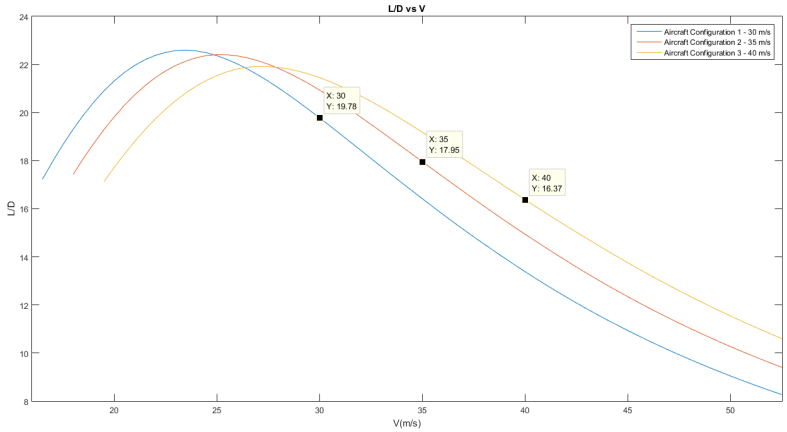

Figure 3.16: Lift-to-drag ratio of the aircraft for the 3 optimized configurations

As can be seen from table 3.8 and figures 3.13 - 3.16, the geometric and aerodynamic characteristics of the aircraft are intrinsically connected. A configuration optimized for lower speeds presents a bigger lifting surface area and a lower stall speed. A configuration optimized for higher speeds presents a smaller lifting surface area and a higher stall speed.

A configuration optimized for lower speeds implies less drag, higher lift-to-drag ratio and less power consumption (better aerodynamic efficiency) at the speed it was optimized for than a configuration optimized for higher speeds.

Configuration 2 (optimized for a cruise speed of 35 m/s) is selected for the aircraft. Among the 3 configurations, configuration 2 is deemed to present the best balance between aerodynamic efficiency, robustness to wind gusts at sea environment and space constraints. Configuration 2 presents a better aerodynamic performance at the speed it was optimized for when compared to configuration 3, being also more robust to wind gusts and having a smaller wingspan than configuration 1.

Regarding the configuration selected for the aircraft, the wing characteristics can be found in subsection 3.1.3, the canard characteristics can be found in subsection 3.1.4, the fuselage characteristics can be found in subsection 3.1.5 and the vertical fins characteristics can be found in subsection 3.1.6.

The CAD model with this preliminary configuration obtained for the aircraft is shown in figure 3.17.

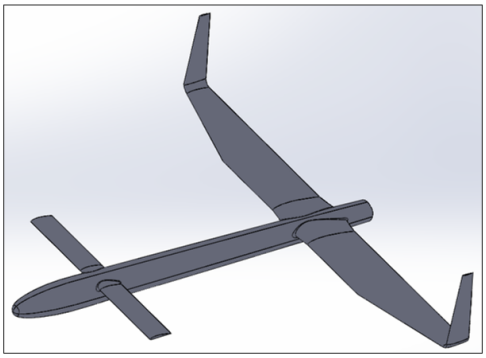

Figure 3.17: Preliminary CAD model: wing, canard, fuselage and vertical fins

The aircraft has a good aerodynamic performance (lift-to-drag of 17.95) and longitudinal stability (static margin of 10.01%). The intended CG longitudinal position is 2.095 m. The stall speed is 18 m/s.

3.2 Aircraft Design Improvement using CFD

The preliminary methods used in the previous section gave a very good estimate of the most suitable shape for the aircraft. However, at this point, a more complete approach should be used to have a better assessment of the aerodynamics of the full aircraft so as to identify possible problems and modify some of the aircraft's features to tackle those issues. By means of a CFD analysis, using the commercial software Ansys CFX, the determination of the aerodynamic forces and moments acting on a certain geometry is done by fully solving the Navier-Stokes equations (refer to subsection 2.3.2).

Each CFD simulation is performed in accordance with the following procedure:

- A CAD model of the aircraft is inputted. An enclosure representing the computational domain is defined. The dimensions are: 5 wing chords to the front, 10 wing chords to the back, 7 wing chords to the top and to the bottom and, 2.5 wingspans to the right and to the left
- A mesh is defined. Its optimum dimensions are determined after a convergence study is performed
- The properties of the flow are set. In accordance with the ISA model [34] and for sea level conditions, the temperature is set at 15 ºC, the density is set at 1.225 kg/m^3 and the pressure is set at 1 atm. The SST turbulence model is also defined at this stage.

  Then, the boundary conditions are set. An inlet condition (cartesian components of the velocity V_x, V_y and V_z) is set at the front, top, bottom, right and left faces of the domain. These components of the velocity take into account the angle of attack α (see equation 3.10) and the sideslip angle β (see equation 3.11). An outlet condition (atmospheric pressure) is set at the back face of the domain. A no slip wall condition is set at the surface of the aircraft
- Ansys CFX solves the problem and the results are obtained. The forces F_x, F_y, F_z and the moments M_x, M_y and M_z at the origin of the CAD model (aircraft nose) are obtained. Lift L and

drag D can be calculated from equation 3.12. The moments at a generic point (x,y,z) $\mathcal{L}$, M and N can be calculated from equation 3.13.

$$\begin{bmatrix} V_x \\ V_y \\ V_z \end{bmatrix} = V_\infty \begin{bmatrix} cos(\alpha) \\ 0 \\ sin(\alpha) \end{bmatrix} \quad (3.10) \qquad \begin{bmatrix} V_x \\ V_y \\ V_z \end{bmatrix} = V_\infty \begin{bmatrix} cos(\beta) \\ -sin(\beta) \\ 0 \end{bmatrix} \quad (3.11)$$

$$\begin{bmatrix} D \\ L \end{bmatrix} = \begin{bmatrix} cos(\alpha) & sin(\alpha) \\ -sin(\alpha) & cos(\alpha) \end{bmatrix} \cdot \begin{bmatrix} F_x \\ F_z \end{bmatrix} \quad (3.12) \qquad \begin{bmatrix} \mathcal{L} \\ M \\ N \end{bmatrix} = \begin{bmatrix} M_x - F_z \cdot y + F_y \cdot z \\ M_y - F_x \cdot z + F_z \cdot x \\ M_z - F_y \cdot x + F_x \cdot y \end{bmatrix} \quad (3.13)$$

3.2.1 Longitudinal static stability

As for the longitudinal motion of the aircraft, the variation of the lift and drag coefficients with angle of attack and canard angle of incidence are given by equations 3.14 and 3.16, respectively [40]. The longitudinal stability of the aircraft is studied through its CG pitch moment. The variation of the CG pitch moment coefficient with angle of attack and canard angle of incidence is given by equation 3.15 [40].

$$C_L = C_{L0} + C_{L\alpha} \cdot \alpha + C_{Li_c} \cdot i_c \quad (3.14) \qquad C_M = C_{M0} + C_{M\alpha} \cdot \alpha + C_{Mi_c} \cdot i_c \quad (3.15)$$

$$C_D = C_{D0} + C_{D\alpha} \cdot \alpha + C_{D\alpha^2} \cdot \alpha^2 + C_{Di_c} \cdot i_c + C_{Di_c^2} \cdot i_c^2 + C_{D\alpha i_c} \cdot \alpha \cdot i_c \quad (3.16)$$

For the theories used in the preliminary sizing (Lifting Line Theory and Panel Method), the computation of the derivatives C_{L0}, $C_{L\alpha}$, C_{Li_c}, C_{D0}, $C_{D\alpha}$, $C_{D\alpha^2}$, C_{Di_c}, $C_{Di_c^2}$, $C_{D\alpha i_c}$, C_{M0}, $C_{M\alpha}$ and C_{Mi_c} follows from the formulas listed in appendix B. For the CFD analysis, these derivatives are obtained by polynomial regression of the aerodynamic coefficients C_L, C_D and C_M obtained for different α and i_c.

In tables 3.9 and 3.10 and, for the preliminary configuration of the aircraft (refer to subsection 3.1.7), the derivatives calculated from Lifting Line Theory, Panel Method and CFD analysis are compared. It is worth mentioning that the moments are referred to the preliminary CG position, i.e, x = 2.095 m.

	Panel Method	**Lifting Line Theory**	**Navier-Stokes (CFD)**
C_{M0}	0.109815	0.113977	0.132606
$C_{M\alpha}$	-0.013626/º	-0.012419/º	0.009657/º
C_{Mi_c}	0.079460/º	0.079843/º	0.082889/º

Table 3.9: Pitch moment derivatives obtained from different theories

	Panel Method	Lifting Line Theory	Navier-Stokes (CFD)
C_{L0}	0.237477	0.254986	0.243156
$C_{L\alpha}$	0.110365/º	0.109661/º	0.118897/º
C_{Li_c}	0.019865/º	0.019961/º	0.013954/º
C_{D0}	0.020066	0.018890	0.021717
$C_{D\alpha}$	0.001119/º	0.001439/º	0.001165/º
$C_{D\alpha^2}$	0.000426/º/º	0.000526/º/º	0.000537/º/º
C_{Di_c}	0.000407/º	0.000527/º	0.000541/º
$C_{Di_c^2}$	0.000096/º/º	0.000096/º/º	0.000015/º/º
$C_{D\alpha i_c}$	0.000192/º/º	0.000192/º/º	0.000215/º/º

Table 3.10: Lift and drag derivatives obtained from different theories

From tables 3.9 and 3.10, some discrepancies can be observed between the preliminary theories and the CFD analysis. First, neither the lift of the fuselage nor the drag of the vertical fins is considered in the preliminary models (this not only affects the aircraft lift and drag, but also its pitch moment); second, the interaction between the flow and the wakes from different parts of the aircraft is better estimated with a CFD analysis; third, the blending between the lifting surfaces and the fuselage, as well as the blending between the vertical fins and the wing also contribute to the observed differences.

According to [40], for a longitudinally stable aircraft, $C_{M\alpha} < 0$. However, as one can see from the third column of table 3.9, $C_{M\alpha} > 0$, meaning that the aircraft is not actually longitudinally stable. This can be further evidenced by the fact that the aerodynamic center is placed at x=2058.55 mm, i.e., ahead of the intended CG (x=2095 mm). In order to improve the pitch stability of the aircraft, some of the actions that can be performed are: moving the canard backwards, moving the wing backwards and/or moving the intended CG forward. It is deemed that moving the wing backwards and/or moving the intended CG forward are the most appropriate actions, since this will also increase the distance between the aerodynamic center of the vertical fins and the CG, thus, increasing the lateral stability of the aircraft.

In order to have a more accurate understanding of how moving the wing backwards influences the longitudinal position of the aerodynamic center of the aircraft, different aircraft configurations with different wing leading edge positions are analysed. Figure 3.18 illustrates this fact.

The top blue line of figure 3.19 gives an estimate of the aerodynamic center longitudinal position as a function of the wing leading edge position. The dots in the top blue line correspond to the aerodynamic center longitudinal positions obtained for the wing leading edge positions shown in figure 3.18. For other wing leading edge positions, the aerodynamic center longitudinal position is estimated from a linear interpolation method. The other lines in figure 3.19 represent the positions at which the CG must be to have a certain static margin, namely 5%, 7.5%, 10%, 12.5% and 15%.

Some useful estimations can be achieved by inspection of figure 3.19:

- If a certain wing leading edge position is desired, the aerodynamic center can be estimated. If, additionally, a certain static margin is also desired, the required CG position can be estimated

- If a certain CG position and a certain static margin are desired, the wing leading edge position can be estimated

- In case placing the fuel tank at the CG is not possible, there will be CG travel during flight as the fuel amount decreases. With figure 3.19 and, for a certain wing leading edge position, a range of possible static margins/CG positions during flight can be estimated

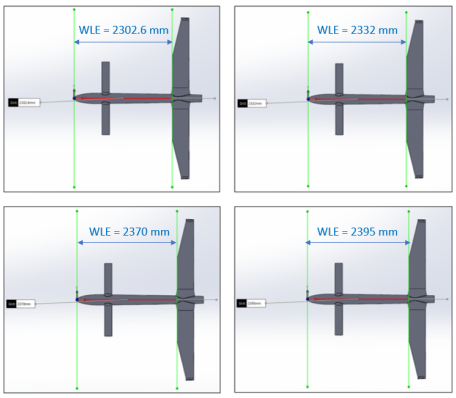

Figure 3.18: Different wing leading edge positions. WLE = 2302.6 mm; WLE = 2332 mm; WLE = 2370 mm; WLE = 2395 mm

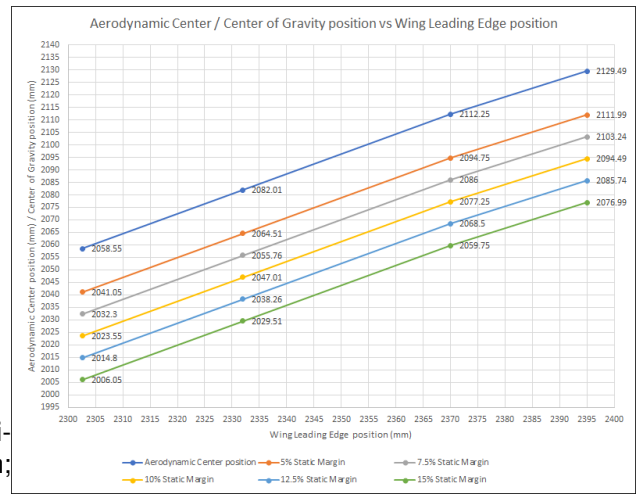

Figure 3.19: Aerodynamic center position vs Wing leading edge position

3.2.2 Lateral static stability

The aircraft lateral stability is studied through its CG roll and yaw moments. The coefficients of the CG roll and yaw moments are given by equations 3.17 and 3.18, respectively [40]. β is the sideslip angle.

$$C_{\mathcal{L}} = C_{L0} + C_{L\beta} \cdot \beta \qquad (3.17)$$

$$C_N = C_{N0} + C_{N\beta} \cdot \beta \qquad (3.18)$$

CFD simulations are done to evaluate the possible need to improve the yaw stability obtained from the preliminary design (refer to subsection 3.1.6). Among other actions, this can be achieved by increasing the area of the fins, moving the aerodynamic center of the fins backwards (therefore, increasing the distance between the CG and the aerodynamic center of the fins) and/or by adding a third vertical fin. Roll stability is also evaluated with CFD simulations and imposing a wing dihedral might be needed [40].

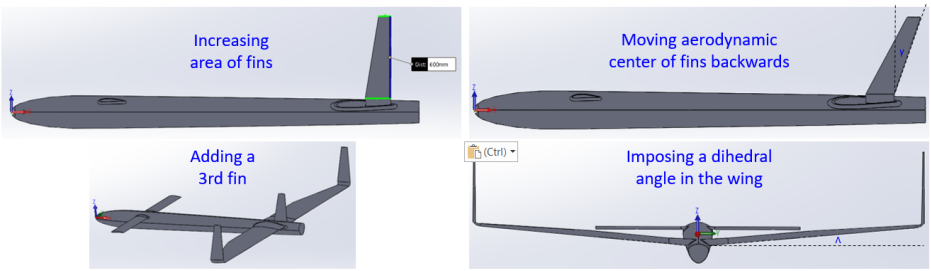

Figure 3.20: Actions that may be used to improve the lateral stability of the aircraft

According to [40], for an aircraft to have yaw stability, $C_{N\beta} > 0$. However, different authors consider different optimum values for $C_{N\beta}$. In [34], $C_{N\beta} > 0.0571/rad$ is advised for enough yaw stability. In [47], $C_{N\beta} \simeq 0.1/rad$ is advised for an optimum yaw stability, however this value is based on statistical data from past aircraft which do not include canard configurations.

Based on figure 3.20, $C_{N\beta}$ is plotted as function of different CG positions for different fin heights, fin angles (angle γ of figure 3.20) and heights of a possible third fin.

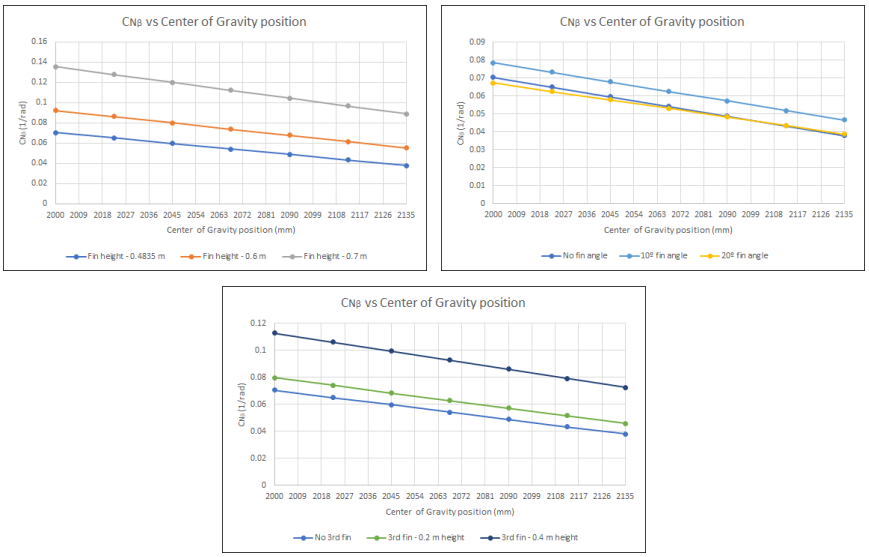

Figure 3.21: Top left image: $C_{N\beta}$ vs CG position for different fin heights. Top right image: $C_{N\beta}$ vs CG position for different fin angles. Bottom image: $C_{N\beta}$ vs CG position for different heights of a third fin

Keep assuming an intended aircraft CG position of x = 2.095 m, figure 3.21 shows that the solutions that actually guarantee $C_{N\beta} > 0.0571/rad$ are to increase the fin height and/or to add a third fin. Among these two solutions, it was decided that increasing the fin height is an aerodynamically more efficient and more practical solution than adding a third fin. Aerodynamically, it is more efficient, since the extra drag contribution from increasing the fin area is expected to be less pronounced than the extra drag contribution from adding a complete new fin. Adding a complete new fin also means more mechanical complexity in the aircraft design, thus a less practical approach.

Furthermore, to complement the solution of fin height increase to 0.6 m, a fin angle of 10º is also used to further enhance the yaw stability of the aircraft.

From [40], for an aircraft to have roll stability, $C_{L\beta} < 0$. In [35], $-0.4/rad < C_{L\beta} < 0/rad$ is advised.

Table 3.11 shows the influence of wing dihedral in the roll stability of the aircraft.

Dihedral	$C_{L\beta}$ **(/rad)**	**Dihedral**	$C_{L\beta}$ **(/rad)**
No dihedral	-0.193216	5º dihedral	-0.313555

Table 3.11: $C_{L\beta}$ vs wing dihedral

When wing dihedral is considered, there is clearly an increase in the absolute value of $C_{L\beta}$, meaning that the aircraft is more stable in terms of roll. However, it is deemed that the value of $C_{L\beta}$ obtained for

the configuration without wing dihedral is already quite acceptable. Furthermore, building a wing with dihedral is also harder to accomplish when compared to a wing with no dihedral. Given these motives, it is decided that no dihedral will be incorporated in the wing of the aircraft.

3.2.3 Wing/Canard position

A high wing/high canard configuration is deemed to be the most appropriate. In this subsection, the reasons that explain this fact are presented.

According to [49], high wing airplanes are very stable (especially at slower speeds), meaning they can right themselves quickly if they encounter turbulence while travelling slowly. Mid wing airplanes are very well balanced, and their design implies a large control surface area. These airplanes are very maneuverable, but not as stable as high wing airplanes. Low wing airplanes are more stable than mid wing airplanes, but not as much as high wing airplanes. The characteristics of a MAD mission require a very stable aircraft. In particular, during transition, it is important to have an aircraft quite stable at slower speeds and robust to wind gusts in a maritime environment. A high wing configuration is selected.

The optimization of the canard's position is based on a trade-off between aerodynamic, lateral stability and functional aspects. 3 different canard configurations are compared: low, mid and high. From an aerodynamic point of view, the lift-to-drag ratio L/D for different angles of attack α and canard incidence angles i_c are compared among the 3 canard configurations. As for lateral stability, the lateral aerodynamic derivatives are compared among the 3 canard configurations. Regarding the functional aspects, the canard shall be placed in the most suitable way possible so as to take into account the presence of the VTOL architecture and also the vibration and structural issues associated with it.

Figure 3.22 shows the lift-to-drag ratio L/D for different α and i_c for the 3 canard configurations.

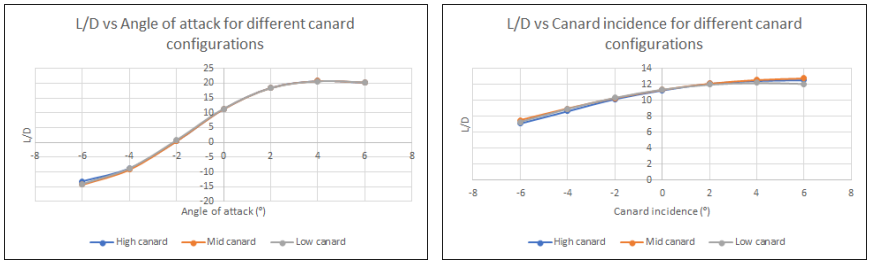

Figure 3.22: Left: L/D vs α for 3 canard configurations. Right: L/D vs i_c for 3 canard configurations

Figure 3.23 shows the roll and yaw moment coefficients for different β for the 3 canard configurations.

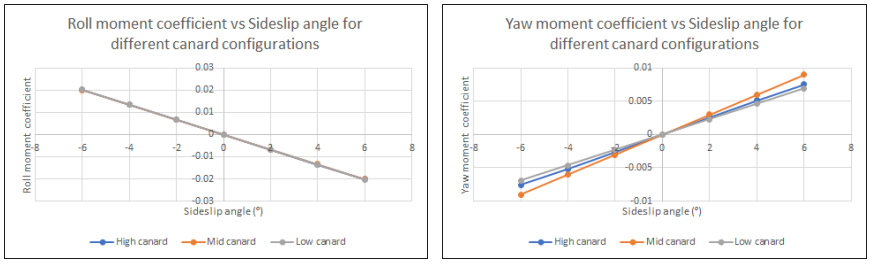

Figure 3.23: Left: $C_{\mathcal{L}}$ vs β for 3 canard configurations. Right: C_N vs β for 3 canard configurations

In figure 3.22, a quite similar aircraft aerodynamic performance for the 3 canard configurations can be seen. In the left image of figure 3.23, a quite similar aircraft roll stability for the 3 canard configurations can be seen. In the right image of figure 3.23, it can be seen that the mid canard configuration is the most stable in terms of yaw, while the high and low canard configurations are less stable in terms of yaw.

A trade-off between all aspects is considered and a high canard configuration (with canard and wing at the same level) is selected mainly due to the fact that it is much easier to fit the VTOL architecture and tackle all the structural and vibration issues regarding it (refer to subsection 3.4.5). Furthermore, aerodynamic and stability aspects are also deemed acceptable with a high canard configuration.

In appendix C, images with the flow interaction between wing and canard for low speed, cruise speed and high speed trimmed conditions can be consulted.

3.2.4 Aircraft Configuration (optimized for cruise, no VTOL architecture included)

The preliminary configuration was presented in subsection 3.1.7. In subsections 3.2.1, 3.2.2 and 3.2.3, CFD simulations were carried out to understand what characteristics of the aircraft had to be modified with respect to the preliminary design so as to provide it with the most suitable aerodynamic performance, longitudinal and lateral stability and, operationality.

In terms of longitudinal characteristics, the wing is moved 9.24 cm backwards to ensure a good static margin/pitch stability for the aircraft. In terms of lateral characteristics, the height of the fins is increased to 0.6 m and a fin angle of 10º is also used to ensure good yaw stability. No wing dihedral is incorporated, since the roll stability is already quite acceptable.

The CAD model with the aircraft configuration optimized for cruise, but without VTOL architecture included yet, is shown in figure 3.24.

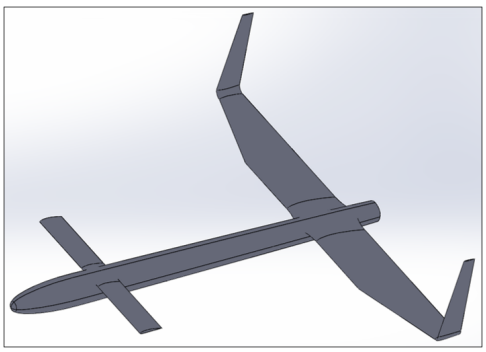

Figure 3.24: CAD model of the aircraft optimized for cruise, but without VTOL architecture included yet

The full aerodynamic analysis of the aircraft in figure 3.24 was performed with CFD. The coefficients of the aerodynamic forces C_L and C_D and, moments C_M, $C_{\mathcal{L}}$ and C_N are obtained for different angles of attack α, canard angles of incidence i_c and sideslip angles β ranging between -6º and 6º. By using polynomial regressions, the aerodynamic derivatives of equations 3.14 - 3.18 can be estimated.

For the case of the lift, drag and CG pitch moment, the following plots can be obtained. C_L, C_D and C_M vs α are obtained for $i_c = 0^o$; C_L, C_D and C_M vs i_c are obtained for $\alpha = 0^o$.

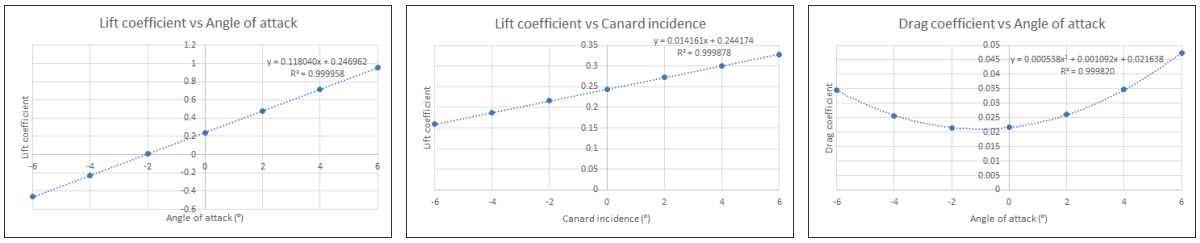

Figure 3.25: Left image: Lift coefficient vs α. Middle image: Lift coefficient vs i_c. Right image: Drag coefficient vs α

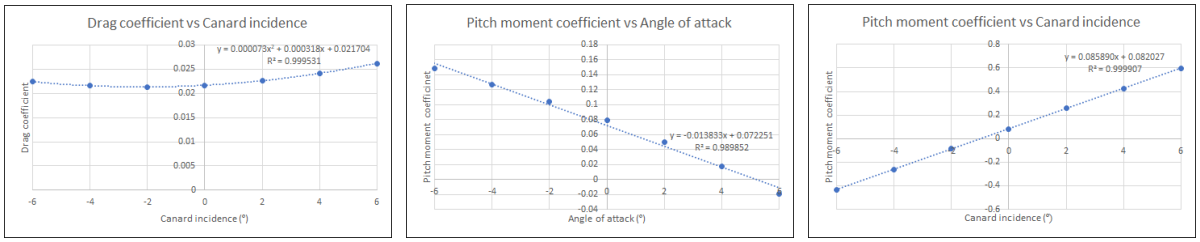

Figure 3.26: Left image: Drag coefficient vs i_c. Middle image: Pitch moment coefficient vs α. Right image: Pitch moment coefficient vs i_c

By inspection of the polynomial regressions present in figures 3.25 - 3.26, the aerodynamic derivatives of equations 3.14 - 3.16 are found. Therefore, equations 3.14 - 3.16 can be rewritten into equations 3.19 - 3.21. α and i_c are given in degrees.

$$C_L = 0.245568 + 0.118040 \cdot \alpha + 0.014161 \cdot i_c \quad (3.19) \qquad C_M = 0.077139 - 0.013833 \cdot \alpha + 0.085890 \cdot i_c \quad (3.20)$$

$$C_D = 0.021671 + 0.001092 \cdot \alpha + 0.000538 \cdot \alpha^2 + 0.000318 \cdot i_c + 0.000073 \cdot i_c^2 + 0.000262 \cdot \alpha \cdot i_c \quad (3.21)$$

For the case of the CG roll and yaw moments, the following plots can be obtained:

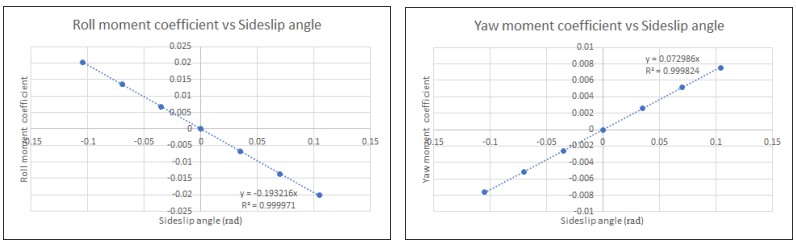

Figure 3.27: Left image: Roll moment coefficient vs β. Right image: Yaw moment coefficient vs β

By inspection of the polynomial regressions present in figure 3.27, the aerodynamic derivatives of equations 3.17 and 3.18 are found. Therefore, equations 3.17 - 3.18 can be rewritten into equations 3.22 - 3.23. β is given in radians.

$$C_{\mathcal{L}} = -0.193216 \cdot \beta \qquad (3.22) \qquad C_N = 0.072986 \cdot \beta \qquad (3.23)$$

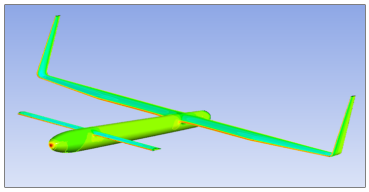

Figure 3.28: Aerodynamic analysis with CFD software

For a better assessment of the aircraft performance, its aerodynamic properties are recalculated, but now with the lift, pitch moment and drag coefficients given by equations 3.19, 3.20 and 3.21, respectively.

The aircraft angle of attack α / wing angle of attack α_w (at this design stage, the wing incidence angle i_w is still assumed to be 0), canard incidence angle i_c and canard angle of attack α_c to guarantee trim condition are represented in figure 3.29. The lift-to-drag ratio and trimmed drag polar are represented in figure 3.30. The thrust and ideal power required to move the aircraft forward are represented in figure 3.31.

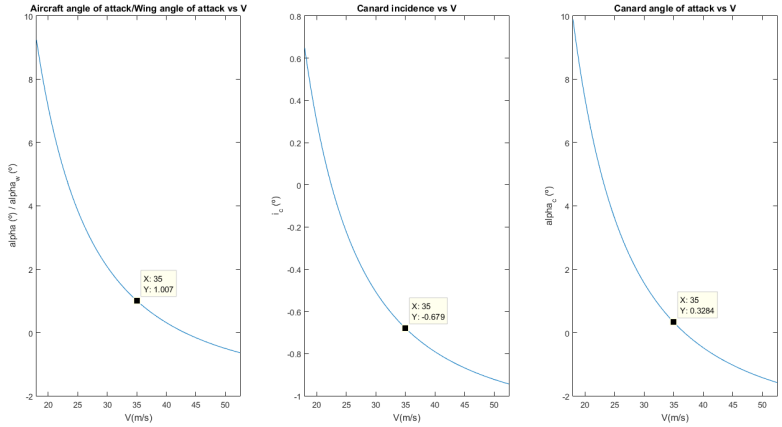

Figure 3.29: Aerodynamic angles for different forward velocities

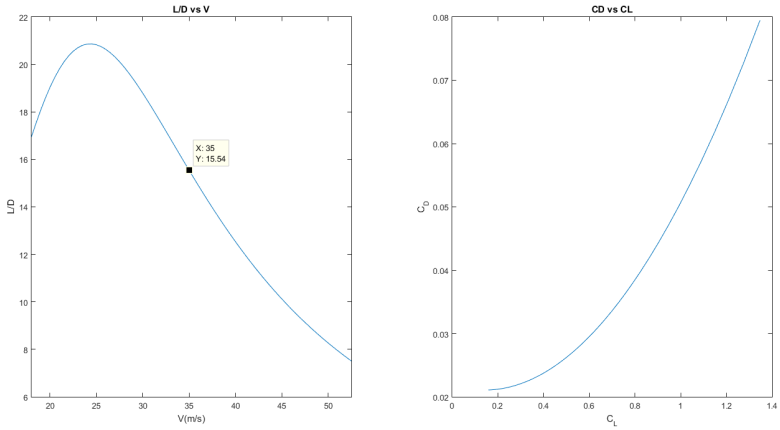

Figure 3.30: Lift-to-drag ratio for different forward velocities and trimmed drag polar

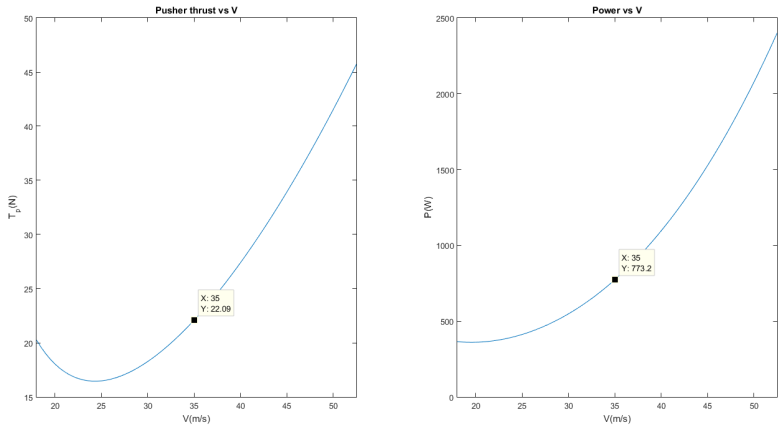

Figure 3.31: Thrust and ideal power for different forward velocities

Compared to when the preliminary sizing was done (refer to subsection 3.1.7), there is now a more accurate evaluation of the forces and moments on the aircraft, already considering the interaction between the flow and the wakes from different parts of the aircraft.

The preliminary and CFD approaches yield similar results for the aircraft angle of attack required to guarantee trim condition. As for the lift-to-drag ratio L/D at the cruise speed of 35 m/s, the value estimated with the CFD approach is $\simeq$ 15.5% smaller than the value estimated with the preliminary approach. These results are further evidenced by the fact that the lift coefficient C_L estimated with both approaches is the same, however there is a $\simeq$ 15.5% increase in the drag coefficient C_D estimated with the CFD approach, as can be seen in table 3.12.

Parameter	CFD	Preliminary	Difference
C_L	0.3563	0.3563	0 %
C_D	0.0229	0.0198	15.5 %
L/D	15.54	17.95	15.5 %

Table 3.12: Comparison between lift coefficient C_L and drag coefficient C_D at cruise speed of 35 m/s estimated with CFD and preliminary approaches

Overall, the aircraft has a good aerodynamic performance (lift-to-drag ratio of 15.54) and longitudinal stability (CG position is set at x = 2.095 m and aerodynamic center position is set at x = 2.131 m, yielding a static margin of $\simeq 10\%$). The estimated ideal power required at cruise condition is 773.2 W.

3.3 Design of Control Surfaces

3.3.1 Ailerons

In subsection 2.3.7, the method used to size the ailerons for this aircraft was presented.

As mentioned, the ailerons should guarantee that the aircraft achieves a bank angle ϕ_{req} of 60º in no more than 1.3 s. Since the performance of the ailerons is worse at lower speeds [50], the aircraft stall

speed is the critical speed for sizing the ailerons.

The ailerons are designed to be capable of complying to the bank angle requirement by using a deflection angle lower than their maximum deflection. As a worst-case scenario, a maximum aileron deflection of 20º is assumed during the design procedure, but in general the deflection limits are higher.

The ratios between the dimensions of the ailerons and the dimensions of the wing are presented in table 3.13. The CAD model of the wing with ailerons included and its dimensions is shown in figure 3.32. Due to symmetry, only one side of the wing is shown.

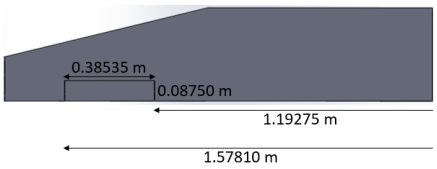

Figure 3.32: Aileron geometry

Parameter	Value	Parameter	Value
Inboard position b_{ai}/b_w	0.650	Span b_a/b_w	0.210
Outboard position b_{ao}/b_w	0.860	Chord $c_a/\bar{c}_w$	0.251
		Area S_a/S_w	0.053

Table 3.13: Ratios between the dimensions of the ailerons and the dimensions of the wing

As a general guidance, the typical values for the parameters listed in table 3.13 are as follows: b_{ai}/b_w = 0.6-0.8, b_a/b_w = 0.2–0.4, $c_a/\bar{c}_w$ = 0.15-0.3 and S_a/S_w = 0.03-0.12 [35]. The designed ailerons are within these typical values.

With these ailerons having a deflection of 20º and, at the stall speed of 18 m/s, the aircraft takes 1.2882 s to achieve a bank angle of 60º, therefore complying to its design requirements. Bigger ailerons can make this time even smaller, however the ailerons may be become excessively sensitive as well, increasing the risk of a perturbation affecting the ailerons and making the aircraft no longer controllable. To avoid this phenomenon, the ailerons are sized to achieve the required bank angle of 60º in a time interval smaller than, yet close to 1.3 s.

For the cruise speed of 35 m/s, a deflection of 5.17º in the ailerons is enough to achieve a bank angle of 60º in precisely 1.3 seconds.

3.3.2 Rudders

In subsection 2.3.7, the method used to size the rudders for this aircraft was presented.

As mentioned, the rudders are designed for a cross-wind situation. Using equations 2.35 and 2.37, equation 3.24 can be obtained and used to estimate the maximum wind V_W sustained by the aircraft (as a fraction of the forward speed U_1) for different rudder deflections δ_R .

$$\frac{V_W}{U_1} = tan(-\frac{C_{N_{\delta_R}}}{C_{N_\beta}} \cdot \delta_R) \tag{3.24}$$

The ratios between the dimensions of the rudders and the dimensions of the vertical fins are presented in table 3.14. The CAD model of the vertical fins with rudders included and its dimensions is shown in the left image of figure 3.33. Due to symmetry, only one vertical fin is shown.

Parameter	Value	Parameter	Value
Inboard position b_{ri}/b_V	0.100	Span b_r/b_V	0.800
Outboard position b_{ro}/b_V	0.900	Chord c_r/c_V	0.539
		Area S_r/S_V	0.431

Table 3.14: Ratios between the dimensions of the rudders and the dimensions of the vertical fins

$C_{N_{\delta_R}} = -0.018/rad$ is estimated from equation 2.39. C_{N_β} can be estimated either from equation 2.38 or from the CFD analysis (refer to subsection 3.2.4). Since a CFD approach is expected to be more accurate, $C_{N_\beta} = 0.073/rad$. Using equation 3.24, the ratio $\frac{V_W}{U_1}$ is plotted for different rudder deflections δ_R in the right image of figure 3.33.

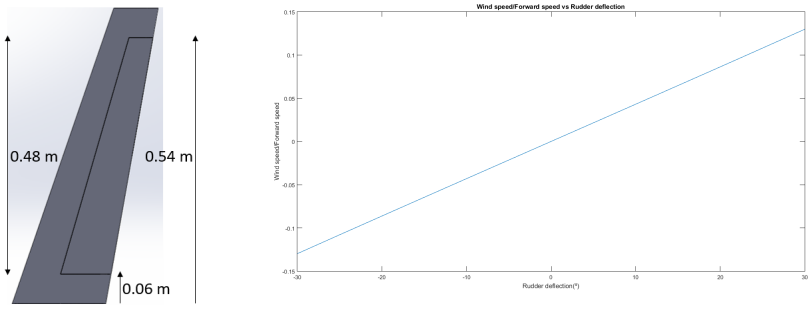

Figure 3.33: Left image: Rudder geometry. Right image: $\frac{V_W}{U_1}$ for different rudder deflections δ_R

For the cruise speed of 35 m/s, the aircraft is expected to sustain a cross-wind of 4.55 m/s with a rudder deflection of 30°.

3.4 Vertical Take-off and Landing Architecture

In section 2.4, the aspects to be taken into account when designing the VTOL architecture of the aircraft were briefly introduced. These include magnetic interference, power consumption, aerodynamic, structural, vibration and control aspects.

Designing the VTOL architecture of the aircraft is a cumbersome task, since many variables are present. From equations 2.40 - 2.47, one can understand that axial climb speed V_c, axial descent speed V_d, radius of the front rotors R_F, radius of the rear rotors R_R, position of the front rotors x_F and position of the rear rotors x_R all play a role in characterizing the VTOL behaviour of the aircraft. These variables not only influence the thrust and power required by both the front and rear rotors, but also the size and weight of the VTOL motors, pods and booms.

3.4.1 Axial climb speed definition

The VTOL motors are used during axial climb, hover, axial descent and transition (the transition stage is analysed with more detail in subsection 3.4.6). The sizing of the VTOL motors is done for the critical condition, i.e., the stage at which more thrust is required to trim the aircraft and more power is consumed.

The critical condition is the axial climb stage. The thrust and power of the motors must be enough to provide the required axial climb speed to the aircraft and, to overcome the weight of the aircraft and the drag component associated with the axial climb speed.

As a simplified way to define the most suitable aircraft axial climb speed, a look at the aircraft drag for different axial climb speeds is shown in figure 3.34. The drag is calculated using equation 3.25. The value of 1.28 is the drag coefficient of a flat plate perpendicular to the flow [51]. The value of 0.8425 is the drag coefficient of a cylinder perpendicular to the flow [52].

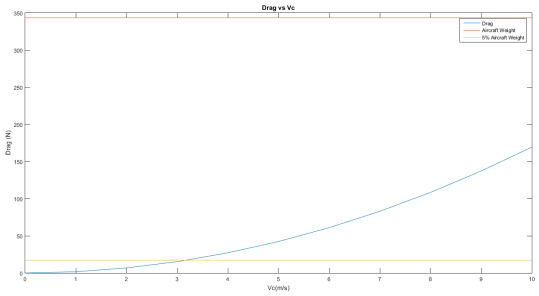

Figure 3.34: Drag of the aircraft vs Axial climb speed

$$Drag = \frac{1}{2} \cdot \rho \cdot V_c^2 \cdot (A_{wing} + A_{canard}) \cdot 1.28 + \frac{1}{2} \cdot \rho \cdot V_c^2 \cdot A_{body} \cdot 0.8425 \tag{3.25}$$

From figure 3.34, a value of 2 m/s is deemed suitable for the axial climb speed. With an axial climb speed of 2 m/s, the drag is less than 5% of the aircraft weight. Furthermore, with this axial climb speed, the aircraft takes between 30 seconds and 70 seconds to reach the cruise altitude (refer to table 1.3).

3.4.2 Thrust required

The thrust required from both the front and rear VTOL motors depends on the flight condition and, on the position of the front rotors x_F and rear rotors x_R. A better understanding of the meaning of the parameters x_F and x_R is provided by figure 3.35.

For an axial climb of 2 m/s, the front rotor thrust T_F and the rear rotor thrust T_R are plotted for different positions of the VTOL motors in the left and right images of figure 3.36, respectively. The thrust of a rotor is obviously bigger (smaller) when this same rotor is placed closer (further) to the CG of the aircraft.

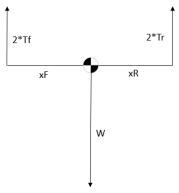

Figure 3.35: Parameters x_F and x_R, respectively position of the front and rear VTOL motors

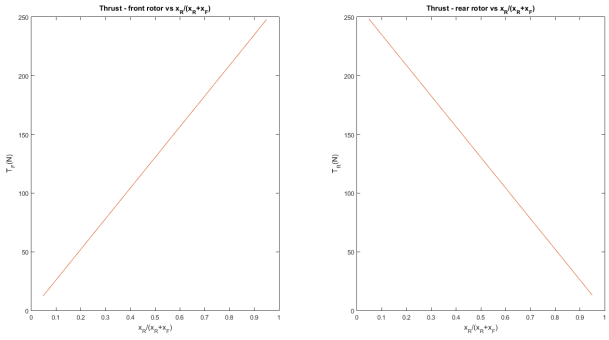

Figure 3.36: Front rotor thrust T_F and rear rotor thrust T_R for different positions of the VTOL motors

3.4.3 Power calculations and location of the VTOL motors

The power required from both the front and rear VTOL motors, as well as the total power required, depend on the flight condition, position of the front rotors x_F and rear rotors x_R and, radius of the front rotors R_F and rear rotors R_R.

For an axial climb of 2 m/s, the front rotor power P_F, the rear rotor power P_R and the total power P are plotted for different positions and radius of the VTOL motors in figure 3.37.

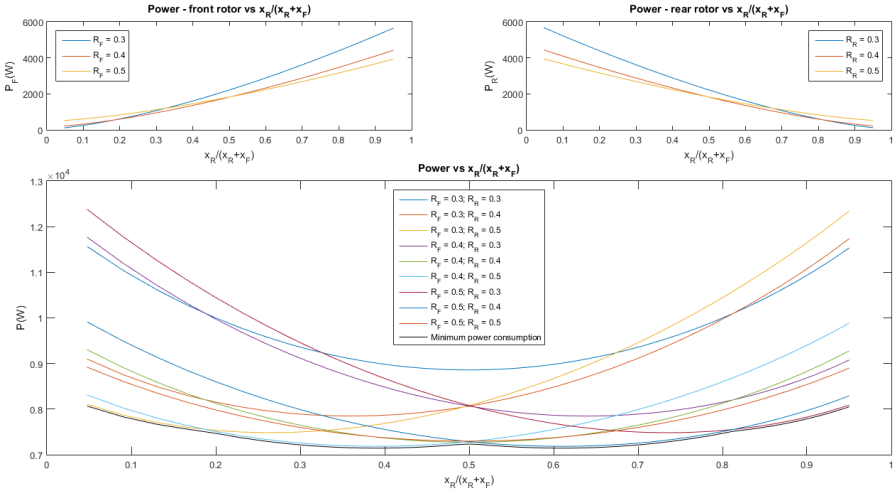

Figure 3.37: Top left image: Front rotor power P_F for different positions and radius of the VTOL motors. Top right image: Rear rotor power P_R for different positions and radius of the VTOL motors. Bottom image: Total power P for different positions and radius of the VTOL motors

In the bottom image of figure 3.37, the black line represents the minimum theoretical total power required P for a certain position of the VTOL rotors, which occurs when both the front and rear rotors have a certain theoretical radius. Overall, the minimum theoretical total power consumption occurs when $R_F \simeq 0.4$, $R_R \simeq 0.5$ and $\frac{x_R}{x_R+x_F} = 0.39$ or when $R_F \simeq 0.5$, $R_R \simeq 0.4$ and $\frac{x_R}{x_R+x_F} = 0.61$.

In practise, having rotors placed at exactly these positions may be very hard to accomplish, since other constraints (magnetic interference, structural, vibration, control) also play important roles. Hence, it is worth quantifying the difference, in terms of total power consumption, between having the rotors at these positions of minimum theoretical total power consumption and having the rotors in other positions.

Figure 3.38 shows the total power increase when the rotors are at a certain position compared to when the rotors are at the positions of minimum theoretical total power consumption.

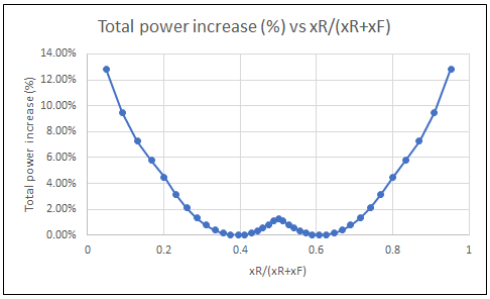

Figure 3.38: Total power increase for different positions of the front and rear rotors

From figure 3.38, it is possible to conclude that the differences between having the rotors at the positions of minimum theoretical total power consumption and having the rotors in other positions are limited to a maximum increase of 12.83%. Furthermore, for $0.2 < \frac{x_R}{x_R+x_F} < 0.8$, the power increase is limited to a maximum value of just 4.51%.

Hence, if placing the rotors at positions other than those that minimize total power consumption is needed to meet other constraints, the power penalties arising from that strategy are deemed acceptable.

3.4.4 VTOL booms

The orientation and aspect ratio of a boom influences the drag due to its presence. In [52], drag coefficients of booms perpendicular and parallel to flow can be found for different boom aspect ratios L/D. This allows to obtain the ratio between the drag of a boom parallel to the flow and the drag of a boom perpendicular to the flow for different boom aspect ratios L/D, as can be seen in figure 3.39.

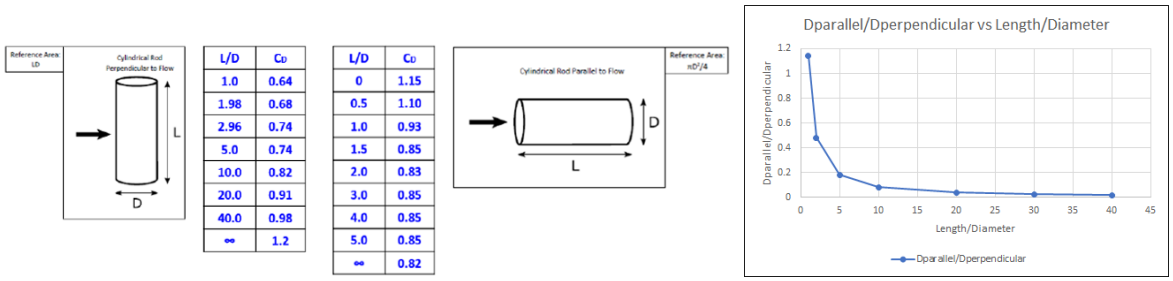

Figure 3.39: Ratio between the drag of a boom parallel to the flow and the drag of a boom perpendicular to the flow for different aspect ratios L/D [52]

Figure 3.39 proves that, for normal boom aspect ratios L/D ($L >> D$), the drag of a boom parallel to the flow is substantially lower when compared to the drag of a boom perpendicular to the flow.

3.4.5 Aircraft Configuration (VTOL architecture included)

Based on all the magnetic interference, power consumption, aerodynamic, structural, vibration and control issues, a VTOL architecture is defined for the aircraft.

The CAD model of the aircraft with the VTOL architecture included is shown in figure 3.40.

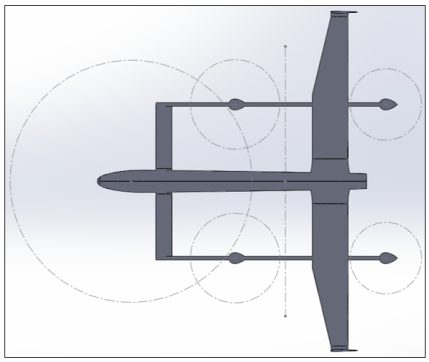

Figure 3.40: CAD model of the aircraft with VTOL architecture included

In figure 3.40, the biggest dashed circle has a radius of 1.35 m and represents the minimum distance from the MAD-XR sensor at which the VTOL motors can be placed (refer to table 1.2). The VTOL motors are placed outside of this circle, thus complying to the requirements regarding magnetic interference.

Furthermore, the VTOL motors are placed in such a way that $\frac{x_R}{x_R+x_F} \simeq 0.67$. This value is feasible in terms of aircraft control and implies a very small increase in the total power consumption compared to the configurations associated with a minimum total power consumption. As an example, for an axial climb of 2 m/s, the thrusts and powers consumed by the rotors are shown in table 3.15. These values are obtained for an MTOW = 35 kg.

Parameter	**Value**	**Parameter**	**Value**
Front rotor thrust (N)	173.934	Front rotor power (W)	2529.6
Rear rotor thrust (N)	86.967	Rear rotor power (W)	1076.4
		Total power (W)	7212

Table 3.15: Front rotor thrust (1 rotor), rear rotor thrust (1 rotor), front rotor power (1 rotor), rear rotor power (1 rotor) and total power (4 rotors) for an axial climb of 2 m/s

Based on the study in figure 3.39 and since a configuration with fixed booms is adopted, these booms are placed parallel to the flow. The increase in the aircraft drag is smaller, which results in an aerodynamically more efficient configuration.

VTOL pods are used to enclose the electric motors and protect them during flight. According to [53], for speeds lower than the speed of sound, the most aerodynamically efficient shape is the teardrop. This shape has the lowest drag coefficient [53] and it is therefore used to design the VTOL pods. A teardrop curve is defined by the following generic parametric equations [54]:

$$x(t) = a \cdot cos(t) + a \tag{3.26}$$

$$y(t) = b \cdot sin(t) \cdot sin(0.5t)^m \tag{3.27}$$

To have an estimation of suitable dimensions for the VTOL pods, a reference electric motor (KDE10218XF-105 [55]) available in the market is used. This motor is capable of providing the required thrust and power characteristics estimated in table 3.15.

Based on equations 3.26 and 3.27, the geometry of the designed VTOL pods respects the following parametric equations.

$$x(t) = 0.1 \cdot cos(t) + 0.1 \tag{3.28}$$

$$y(t) = 0.08 \cdot sin(t) \cdot sin(0.5t) \tag{3.29}$$

From figure 3.41, the designed VTOL pods fit the reference electric motor (KDE10218XF-105) inside.

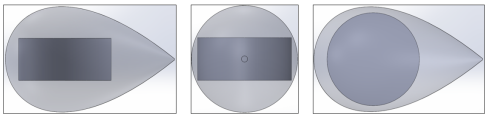

Figure 3.41: Light grey: VTOL pod; dark grey: simplistic representation of an electric motor

The structural and vibration issues are also very important constraints of the design. Namely, stiffening the structure is necessary to counter the vibration of the electric motors and respect the structural integrity of the aircraft. This is achieved by ”connecting” the VTOL booms to the rest of the aircraft structure in the way pictured in figure 3.40.

As can be seen in figure 3.40, wing and canard are at the same level. One end of the booms coincides with the tip of the canard. The rear VTOL pods are placed at the other end of the booms. The front VTOL pods are placed in the middle of the booms. The adopted strategy is expected to assure a robust and stiffened aircraft structure against the vibration of the VTOL motors.

3.4.6 Transition

In section 2.4.3, the equations necessary to describe the evolution of forces and powers generated by all the components of the propulsive system during the aircraft's transition mode were introduced.

In terms of performance, the definition of the transition speed V_{trans} follows the same criterium used to define the take-off speed in a conventional aircraft, i.e., $V_{trans} = 1.2 \times V_{stall}$ [47]. The stall speed V_{stall} of the aircraft is estimated to be 18 m/s (in section 4.1). Once the transition speed is reached, the electric motors are switched off and the aircraft is solely powered by the pusher engine.

For the position of the rotors determined in subsection 3.4.5, the evolution of all the forces (aircraft lift, front rotor thrust, rear rotor thrust and pusher thrust), as a function of the speed during transition, is provided in figure 3.42. Data from section 4.1 is used to compute these results.

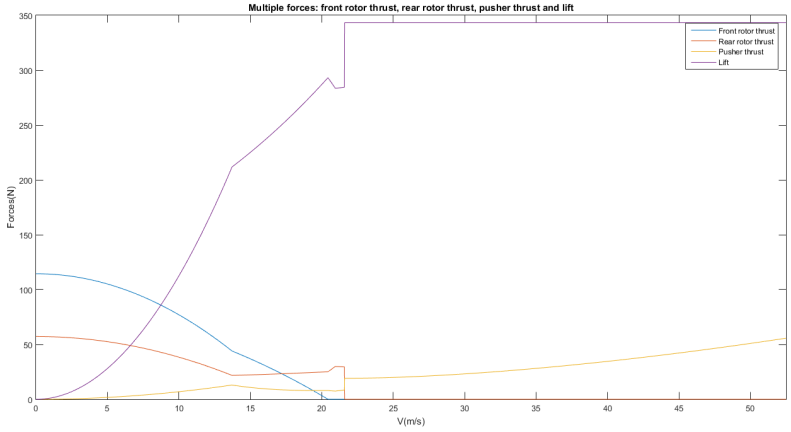

Figure 3.42: Evolution of forces during the aircraft's transition mode

For the position of the rotors determined in subsection 3.4.5, the evolution of all the powers (total power, front rotor power, rear rotor power and pusher power), as a function of the speed during transition, is provided in figure 3.43. Data from section 4.1 is used to compute these results.

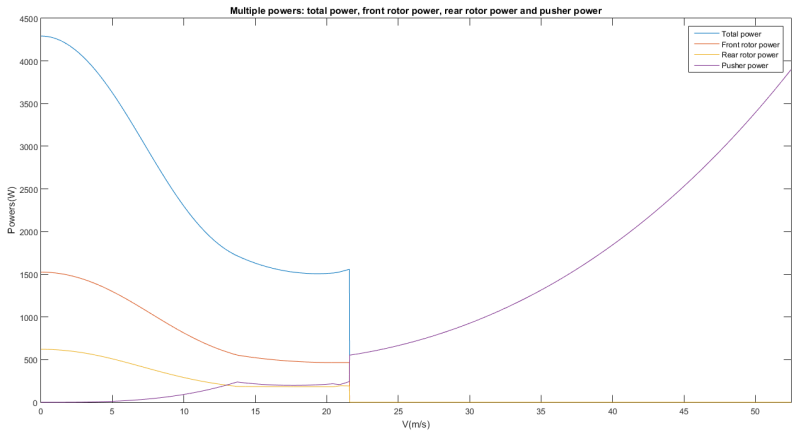

Figure 3.43: Evolution of powers during the aircraft's transition mode

In figures 3.42 and 3.43, the dynamics of forces and consumed powers by the aircraft becomes clear. In the beginning, at very low speeds, the thrust of the VTOL rotors is dominant, since the generated lift is still very small. At these very low speeds, the thrust of the VTOL rotors does the major work in overcoming the aircraft weight. As the speed during transition mode increases, the lifting surfaces are capable of generating more lift, meaning that less thrust is gradually required from the VTOL rotors; on the other hand, in order to propel the aircraft forward, the pusher engine also has more and more influence on the behaviour of the aircraft. Once the stall speed is achieved, the thrust of the VTOL rotors is no longer needed to trim the aircraft, however for safety reasons, they only become 0 at the transition speed V_{trans}. Thus, for speeds higher than V_{trans}, the aircraft is fully powered by the piston engine, namely during its cruise condition.

As for power evolution, it can be seen that as the speed increases, power from VTOL rotors continuously decreases and pusher engine power continuously increases. Due to these two power contributions evolving in opposite ways, a minimum of the total power consumed by the aircraft during transition can be obtained.

The sudden change of forces and powers at the transition speed is explained by the fact that when the VTOL rotors are switched off and the thrust contribution is lost, there is a sudden increase in the aircraft lift in order to overcome the weight and trim the aircraft. A sudden increase in the aircraft lift is achieved with a sudden increase in the aircraft angle of attack, meaning also a sudden increase in the aircraft drag, thrust required and pusher power.

Chapter 4

Aircraft Performance Analysis

4.1 Final Configuration and Aircraft Performance

Based on all the results from chapter 3, a final optimization of the aircraft configuration is performed.

The CAD model with the final configuration for the aircraft is shown in figure 4.1.

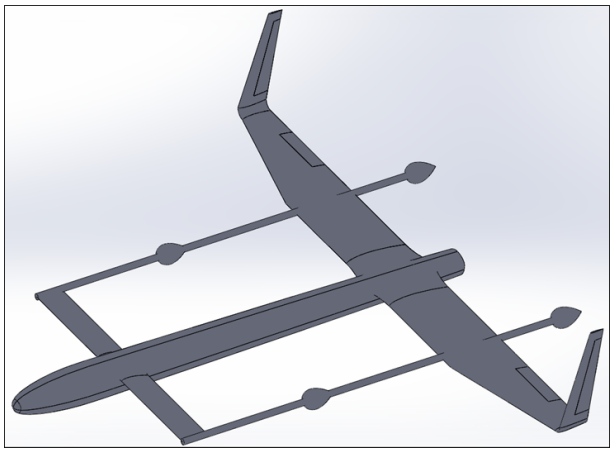

Figure 4.1: CAD model with the final configuration for the aircraft

So far, no wing incidence angle i_w had been considered, so as to ease all the process of design. However, the use of an incidence angle for the wing is appropriate since it helps in reducing the drag for a given lift. Having the wings at a certain angle of attack and the fuselage horizontal in cruise means that the aircraft drag is minimized, while the wing has the required angle of attack to trim the aircraft [56]. From the left image of figure 3.29, at the cruise speed of 35 m/s, the wing must have an angle of attack of $\simeq 1^{o}$ to trim the aircraft. Thus, the wing incidence angle i_w is set at 1^{o}.

Furthermore, all the blendings between the lifting surfaces and the fuselage are better designed, so as to have a smoother and more aerodynamic aircraft geometry.

A final CFD analysis is performed to estimate the aerodynamic properties of the aircraft. In this CFD analysis, the presence of the VTOL architecture is finally considered and, the drag penalties due to its incorporation in the aircraft can be assessed.

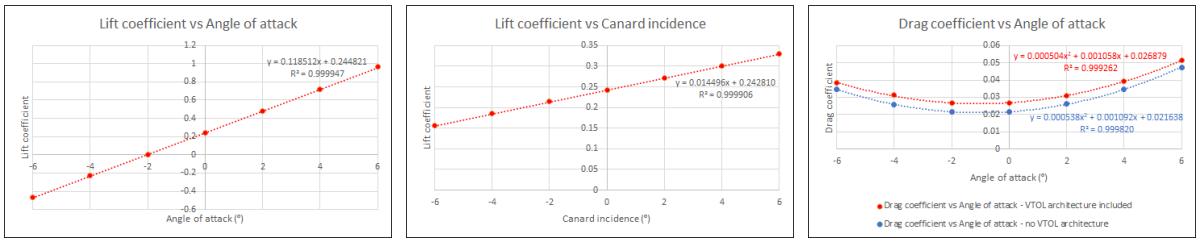

Figure 4.2: Left image: Lift coefficient vs α. Middle image: Lift coefficient vs i_c. Right image: Drag coefficient vs α

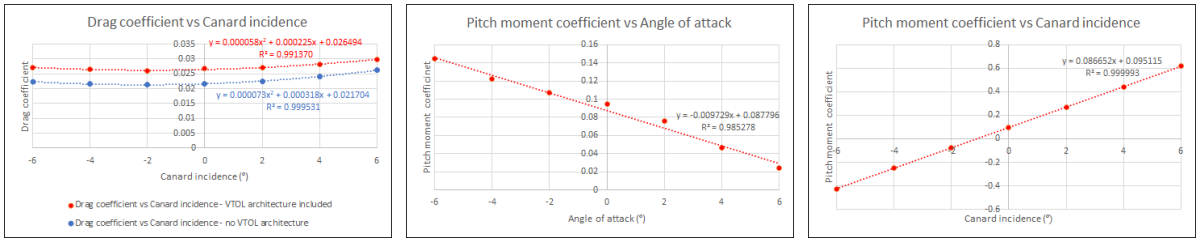

Figure 4.3: Left image: Drag coefficient vs i_c. Middle image: Pitch moment coefficient vs α. Right image: Pitch moment coefficient vs i_c

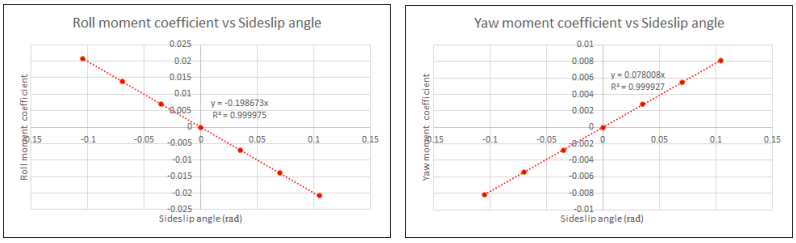

Figure 4.4: Left image: Roll moment coefficient vs β. Right image: Yaw moment coefficient vs β

In the right image of figure 4.2 and in the left image of figure 4.3, the blue lines represent the drag of the aircraft when no VTOL architecture is considered and, the red lines represent the drag of the aircraft when the VTOL architecture is considered. For different angles of attack and canard incidence angles, an increase of around 20% in the drag of the aircraft can be observed when the VTOL architecture is incorporated.

From figures 4.2, 4.3 and 4.4, equations 4.1, 4.2, 4.3, 4.4 and 4.5 are obtained and used to describe the lift, pitch moment, drag, roll moment and yaw moment coefficients of the aircraft, respectively. α and i_c are given in degrees. β is given in radians.

$$C_L = 0.243816 + 0.118512 \cdot \alpha + 0.014496 \cdot i_c \quad (4.1)$$

$$C_M = 0.091456 - 0.009729 \cdot \alpha + 0.086652 \cdot i_c \quad (4.2)$$

$$C_D = 0.026687 + 0.001058 \cdot \alpha + 0.000504 \cdot \alpha^2 + 0.000225 \cdot i_c + 0.000058 \cdot i_c^2 - 0.000888 \cdot \alpha \cdot i_c \quad (4.3)$$

$$C_{\mathcal{L}} = -0.198673 \cdot \beta \qquad (4.4) \qquad\qquad C_N = 0.078008 \cdot \beta \qquad (4.5)$$

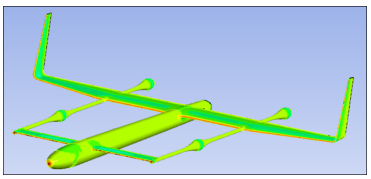

Figure 4.5: Final aerodynamic analysis of the aircraft with CFD software

For this final configuration, the aircraft angle of attack α and canard incidence angle i_c to guarantee trim condition, as well as the wing angle of attack α_w and canard angle of attack α_c are represented in figure 4.6. The lift-to-drag ratio and trimmed drag polar are represented in figure 4.7. The thrust and ideal power required to move the aircraft forward are represented in figure 4.8.

In figures 4.7 and 4.8, the blue lines correspond to the situation in which no VTOL architecture is considered and, the red lines correspond to the situation in which the VTOL architecture is considered. The observed differences are explained by the drag increase due to the presence of the VTOL architecture.

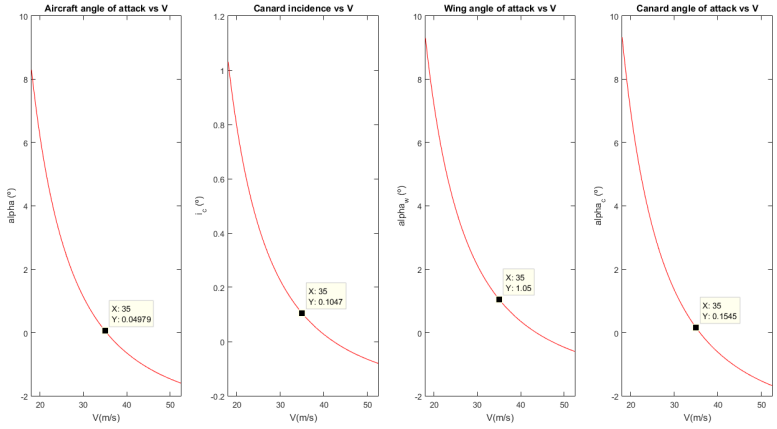

Figure 4.6: Aerodynamic angles for different forward velocities

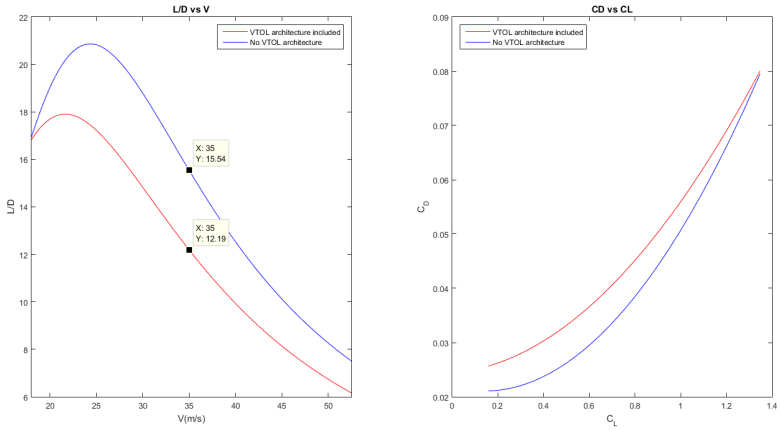

Figure 4.7: Lift-to-drag ratio for different forward velocities and trimmed drag polar

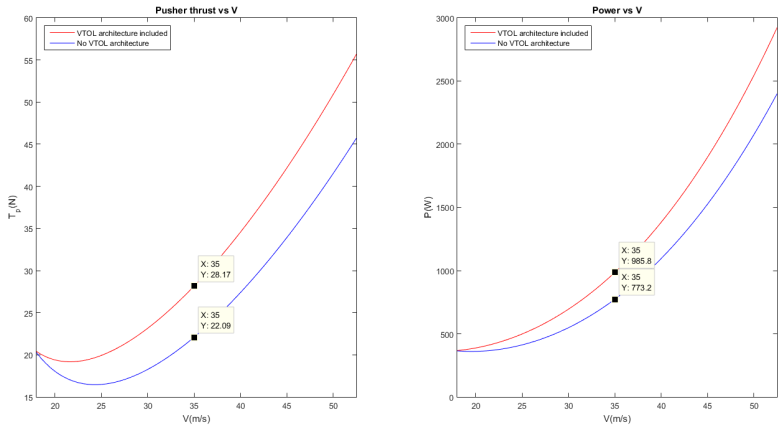

Figure 4.8: Thrust and ideal power for different forward velocities

The final results for this aircraft show a lift-to-drag ratio L/D of 12.19 at the cruise speed of 35 m/s, a stall speed of 18 m/s and an ideal power required at cruise condition of 985.8 W. Therefore, it can be concluded that the incorporation of the VTOL architecture in the aircraft implies a L/D reduction of $\simeq$ 21.5% and an ideal power required increase of $\simeq$ 21.5% (at cruise condition) compared to the results estimated in subsection 3.2.4 (when no VTOL architecture was considered).

In terms of longitudinal stability, the aerodynamic center longitudinal position is placed at x = 2.12636 m. For a CG longitudinal position of x = 2.095 m, this yields a static margin of $\simeq 9\%$. In terms of lateral stability, $-0.4/rad < C_{L\beta} = -0.198673/rad < 0/rad$ and $C_{N\beta} = 0.078008/rad > 0.0571/rad$, thus both derivatives comply to the acceptable requirements found in the literature.

The total fuel required by the aircraft during its mission can be estimated using a simplified approach. Since cruise is by far the dominant condition, it will be assumed that the total fuel required by the aircraft is spent in cruise. Using the Breguet range equation [57] and following the method in [47], equation 4.6 is used to estimate the fuel required to perform the mission.

$$W_{Fuel} = W_i \cdot (1 - e^{-\frac{SFC \cdot g \cdot R}{\eta_p \cdot L/D}}) \cdot (1 + 0.06) \tag{4.6}$$

, where W_i is the MTOW, SFC is the specific fuel consumption, g is the constant of gravity, R is the range, η_p is the propeller efficiency and L/D is the lift-to-drag ratio. In the present case, W_i = 35 kg, SFC = 0.6 lb/bhp.hr [47], $R = 5\ h \times 35\ m/s = 630\ km$ and η_p = 0.75.

With the VTOL architecture incorporated in the aircraft, L/D = 12.19 and the amount of fuel required is $\simeq$ 2.45 kg. As a comparison, when no VTOL architecture is considered, L/D = 15.54 and the amount of fuel required is $\simeq$ 1.93 kg. Therefore, the inclusion of the VTOL architecture implies a $\simeq$ 26.94% increase in the amount of fuel required to perform the mission.

4.2 Wing Loading, Disc Loading and Power Loading

Wing loading

Wing loading W/S is the total weight of an aircraft divided by the area of its wing [58]. A higher wing loading means an aircraft which is faster, less manoeuvrable and with a higher stall speed, whereas a lower wing loading means an aircraft which is slower, more manoeuvrable and with a lower stall speed [58].

In the case of the designed aircraft, $W/S = 267.302\ N/m^2$ or $W/S = 27.248\ kg/m^2$. According to [59], this corresponds to a low wing loading UAV, since $W/S = 27.248\ kg/m^2 < 50\ kg/m^2$.

Disc loading

Disc loading W/A is defined as the ratio of the weight of an aerial vehicle by the rotors disc area [60]. A lower disc loading yields a higher hover efficiency, i.e, the larger the area that the rotors sweep the less power is required to hover, but a large disc area also implies space penalties; on the other hand, a higher disc loading makes the aircraft less sensitive to wind gusts and more stable [60].

In the case of the designed aircraft, $W/A = 133.283\ N/m^2$ or $W/A = 13.586\ kg/m^2$. In [61], characteristics, namely disc loading, are compared between different electric VTOL configurations. Also, in [60], a chart showing the typical range of disc loadings of different vehicles is provided. By comparison with existing data (aircraft with $1\ kg/m^2 \leq W/A \leq 5000\ kg/m^2$), this UAV has a low disc loading.

Power loading

Power loading W/P represents the weight of an aircraft divided by the available power from a propulsive system. A low power loading configuration requires a larger amount of power (also engine/motor and fuel/battery weight) to lift the same amount of weight than a high power loading configuration [62].

A enough powerful piston engine should be able to propel the aircraft forward at a maximum speed of at least $35 \times 1.5 = 52.5\ m/s$ [63]. Assuming a propeller efficiency of 75%, the required power for a speed of 52.5 m/s is 3897.33 W. Thus, a piston engine with a $W/P \leq 0.088\ N/W$ or $W/P \leq 0.009\ kg/W$ should be selected.

Enough powerful electric motors should be able to move the aircraft upwards at an axial climb condition of 2 m/s. The power required for both front and rear rotors is $P_F = 2529.6\ W$ and $P_R = 1076.4\ W$, respectively. Thus, front electric motors with a $W/P \leq 0.136\ N/W$ or $W/P \leq 0.014\ kg/W$ and, rear electric motors with a $W/P \leq 0.319\ N/W$ or $W/P \leq 0.033\ kg/W$ should be selected.

4.3 Dynamic Analysis

VTOL

While performing axial climb/descent stages, the aircraft has a vertical motion. Thus, this implies that $u_0 = 0$ and that w_0 is equal to the climb/descent speed.

Since the aircraft has no horizontal velocity ($u_0 = 0$), the aerodynamic forces and moments X_a, Y_a, Z_a, L_a, M_a and N_a are 0, i.e., $X_a = Y_a = Z_a = L_a = M_a = N_a = 0$.

For axial climb/descent and regardless of the axial climb/descent speed, all the eigenvalues of both 4x4 matrices of equations 2.63 and 2.64 are 0.

Transition

It is admitted that the aircraft performs a horizontal, level transition. Thus, this implies that $w_0 = 0$ and that u_0 is equal to the forward speed.

The left image of figure 4.9 shows the evolution of the longitudinal eigenvalues with the forward speed. The right image of figure 4.9 shows the evolution of the lateral eigenvalues with the forward speed. The longitudinal dynamic modes (short period and phugoid), as well as the lateral dynamic modes (roll, dutch roll and spiral) can be identified.

The left image of figure 4.10 shows the evolution of the real part of the longitudinal eigenvalues with the forward speed. The right image of figure 4.10 shows the evolution of the real part of the lateral eigenvalues with the forward speed.

All results in figures 4.9 and 4.10 are presented for forward speeds between 0 and the transition speed ($V_{trans} = 21.6\ m/s$).

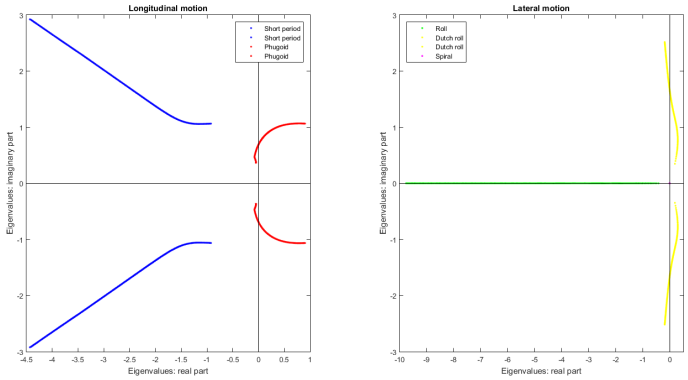

Figure 4.9: Left image: Evolution of the longitudinal eigenvalues with the forward speed before transition occurs. Right image: Evolution of the lateral eigenvalues with the forward speed before transition occurs

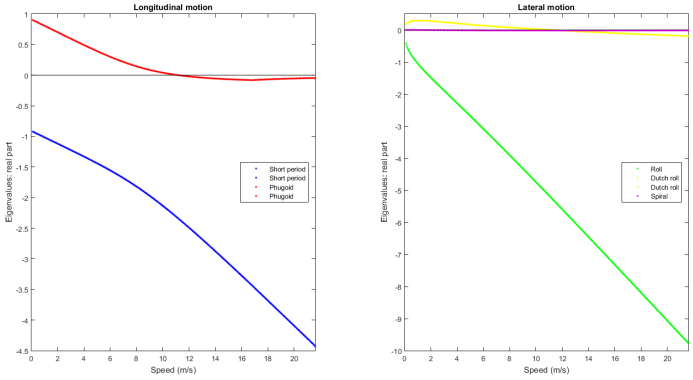

Figure 4.10: Left image: Evolution of the real part of the longitudinal eigenvalues with the forward speed before transition occurs. Right image: Evolution of the real part of the lateral eigenvalues with the forward speed before transition occurs

As seen in figure 4.10, for speeds below 11.2 m/s, the aircraft is both longitudinally and laterally unstable, respectively due to the phugoid and dutch roll modes. All other modes are stable. For speeds above 11.2 m/s, the aircraft is both longitudinally and laterally stable, since all modes are stable.

Forward speed

During its forward speed stage, the aircraft has a horizontal, level motion. Thus, this implies that $w_0 = 0$ and that u_0 is equal to the forward speed.

The left image of figure 4.11 shows the evolution of the longitudinal eigenvalues with the forward speed. The right image of figure 4.11 shows the evolution of the lateral eigenvalues with the forward speed. The longitudinal dynamic modes (short period and phugoid), as well as the lateral dynamic modes (roll, dutch roll and spiral) can be identified.

The left image of figure 4.12 shows the evolution of the real part of the longitudinal eigenvalues with the forward speed. The right image of figure 4.12 shows the evolution of the real part of the lateral eigenvalues with the forward speed.

All results in figures 4.11 and 4.12 are presented for forward speeds between the transition speed ($V_{trans} = 21.6\ m/s$) and the maximum speed ($V_{max} = 52.5\ m/s$).

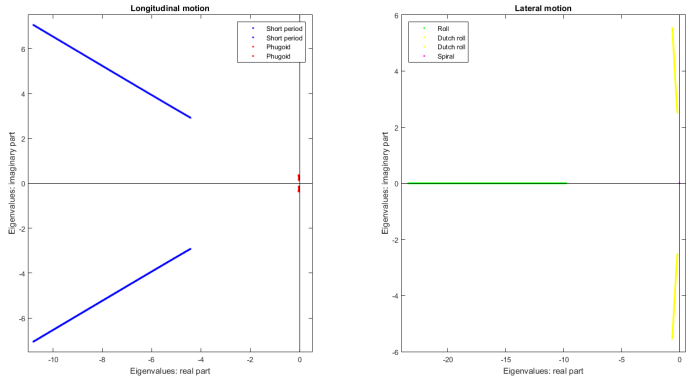

Figure 4.11: Left image: Evolution of the longitudinal eigenvalues with the forward speed after transition occurs. Right image: Evolution of the lateral eigenvalues with the forward speed after transition occurs

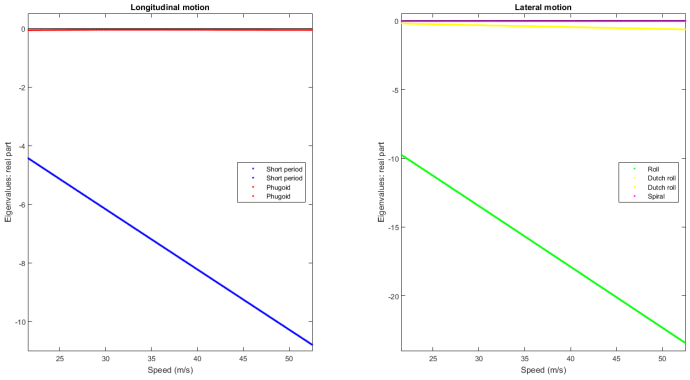

Figure 4.12: Left image: Evolution of the real part of the longitudinal eigenvalues with the forward speed after transition occurs. Right image: Evolution of the real part of the lateral eigenvalues with the forward speed after transition occurs

As seen in figure 4.12, the aircraft is both longitudinally and laterally stable for all forward speeds.

As for the dynamic characteristics at the cruise speed of 35 m/s, the aircraft has the eigenvalues shown in table 4.1. Taking into account these eigenvalues, the flying qualities of every dynamic modes

can be determined from [40] and are also presented in table 4.1.

Dynamic mode	Eigenvalue	Flying quality
Short period	-7.1973 $\pm$ 4.7067 $\cdot i$	Level 1
Phugoid	-0.0374 $\pm$ 0.2250 $\cdot i$	Level 1
Roll	-15.6799	Level 1
Dutch roll	-0.3881 $\pm$ 3.7924 $\cdot i$	Level 1
Spiral	-0.0094	Level 1

Table 4.1: Aircraft eigenvalues and flying qualities for the cruise speed of 35 m/s

4.4 Fixed-pitch Propeller vs Variable-pitch Propeller

In subsection 2.5.3, the advantages and disadvantages between using fixed-pitch and variable-pitch propellers were mentioned. As a summary, some of the disadvantages of variable-pitch propellers include more design complexity and, more vibration and noise since there are more parts, many of them moving. However, a variable-pitch propeller can operate at the envelope of maximum efficiency, meaning less power consumed and required from the engine. The aircraft can achieve higher speeds, thus taking less time to reach its research area.

A study is conducted so as to quantify and compare the maximum speed capable of being achieved by the aircraft for different values of the efficiency of the propeller. The ideal power of the aircraft as function of its forward velocity is given by the red line shown in the right image of figure 4.8. Using equation 2.65 and, for different propeller efficiencies, the real power of the aircraft as function of its forward velocity is shown in figure 4.13.

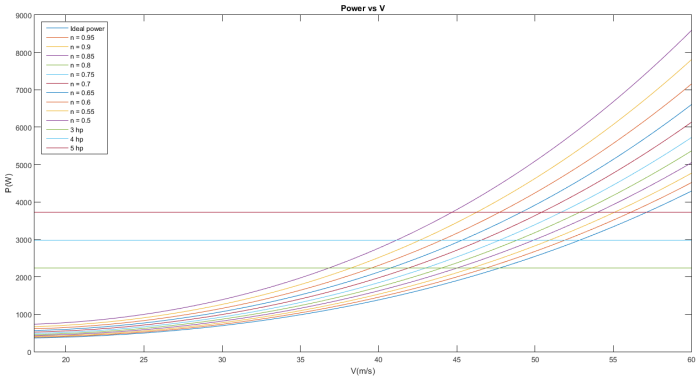

Figure 4.13: Real power of the aircraft vs forward velocity for different propeller efficiencies

Also in figure 4.13, the horizontal lines represent generic values for the engine installed power. 3 hp, 4 hp and 5 hp are used as generic values for the engine installed power. The intersection between these horizontal lines and the real power curves define the maximum speed of the aircraft (this speed is achieved when the power required from the engine to move the aircraft forward is equal to the engine maximum power) for a certain propeller efficiency and a certain engine installed power.

The maximum speed of the aircraft for a certain propeller efficiency and a certain engine installed power (using the generic values of 3 hp, 4 hp and 5 hp) is represented in figure 4.14.

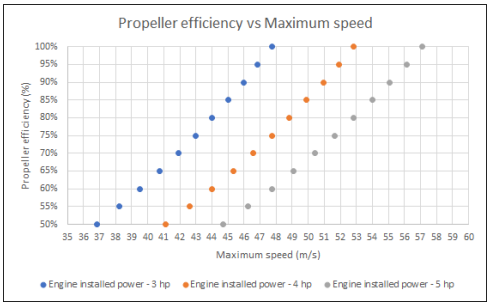

Figure 4.14: Maximum speed of the aircraft vs propeller efficiencies and engine installed powers

Comparing, for example, the maximum speed achieved by the aircraft when the propeller efficiency is 50% and when it is 75%, the results listed in table 4.2 can be obtained.

	Engine power - 3 hp	**Engine power - 4 hp**	**Engine power - 5 hp**
50%	36.82 m/s	41.14 m/s	44.69 m/s
75%	42.99 m/s	47.73 m/s	51.67 m/s
Variation	16.76 %	16.02 %	15.62 %

Table 4.2: Maximum speed achieved by the aircraft when propeller efficiency is 50% and when it is 75%

From table 4.2, there is an increase of around 16 % in the maximum speed capable of being achieved by the aircraft when the propeller efficiency is 75 % (a value which can be reached if a variable-pitch propeller is used) instead of just 50 % (a value which frequently occurs if a fixed-pitch propeller is used).

All the analyses performed in this section are strictly from an aerodynamic point of view. In fact, the maximum speed of the aircraft not only depends on the propulsive system but also on the structural safety of the aircraft. In these analyses, the structural limits of the aircraft were not taken into consideration.

4.5 Possible Improvements to the Design of the Aircraft

As seen in subsection 3.2.4 and in section 4.1, with the incorporation of the VTOL motors, pods and booms in the way pictured in figure 3.40, a significant reduction in the aerodynamic efficiency of the aircraft in cruise is observed. Furthermore, since the VTOL motors are not operating during cruise, they represent ”dead weight” carried by the aircraft during this flight stage.

From the above exposed, an improvement in the design of the VTOL architecture and propulsive system for future versions of the aircraft is advised. For instance, some solutions are presented next: the use of detachable booms instead of fixed booms for the front VTOL motors and, replacing the two rear VTOL motors and pusher engine of the actual aircraft by a tilt rotor.

4.5.1 Detachable booms for the front VTOL motors

With the current aircraft design, all the VTOL motors are fixed and connected to the rest of the aircraft structure with fixed booms. This solution, although satisfactory for a first and minimum risk design, is not the most appropriate in aerodynamic terms. For the front motors, the use of detachable booms to hold them is more appropriate. During VTOL and transition stages, the front motors and detachable booms would be in the position shown in the left image of figure 4.15. During cruise, the detachable booms would be collected and the front motors would be in the position shown in the right image of figure 4.15.

With the strategy pictured in figure 4.15, during cruise, the detachable booms would be parallel to the incoming flow and attached to the fuselage, reducing significantly the drag due to their presence, which improves the aircraft aerodynamic performance and decreases the fuel consumption.

As a disadvantage, there is a possible weight penalty due to the detachable booms' mechanism.

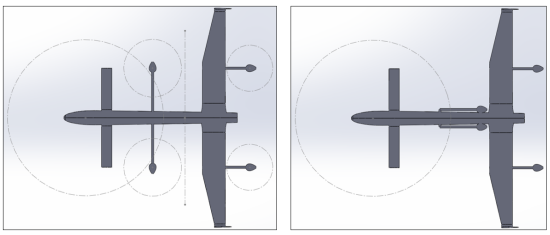

Figure 4.15: Left: VTOL architecture during VTOL and transition. Right: VTOL architecture during cruise

4.5.2 Use of a tilt rotor

Besides using detachable booms for the front VTOL rotors, replacing the two rear VTOL rotors and the pusher engine of the actual aircraft by a single tilt rotor is also advised. Although implying a weight penalty and a more complex design (due to the tilt mechanism), three advantages arise from this solution: better aerodynamic performance, maximum speed increase and propulsive system mass reduction.

Better aerodynamic performance

The booms that currently support the two rear VTOL rotors would disappear. Together with the solution of detachable booms advised for the front VTOL rotors, the aircraft in cruise would adopt a configuration quite similar to what is shown in figure 3.24. Therefore, UAV aerodynamics is significantly improved and fuel consumption is significantly reduced.

Maximum speed increase - fixed booms

3 different propulsive system configurations are compared in terms of power consumption: the current configuration, a configuration with 2 front VTOL motors and 1 tilt rotor in the back and, a configuration with 2 front VTOL motors and 2 tilt rotors in the back.

The front part of the propulsive system is common for all 3 configurations (2 electric VTOL motors). As for the rear part of the propulsive system, with the current configuration, there are 2 electric VTOL motors and a pusher fuel engine for cruise and high speed condition. For the alternative configurations, the tilt rotor(s) (fed by a fuel engine) provide power for vertical motion, cruise and high speed condition.

In figure 4.16, the powers from the pusher/tilt rotor(s) are compared for all 3 configurations and for different locations of the rotors. For the current configuration, power for cruise of 35 m/s and high speed condition of 52.5 m/s are presented. For the 1 tilt rotor and 2 tilt rotors configurations, power for axial climb of 2 m/s, cruise of 35 m/s and high speed condition of 52.5 m/s are presented. The dashed black lines represent the minimum fuel engine installed power required for all 3 configurations.

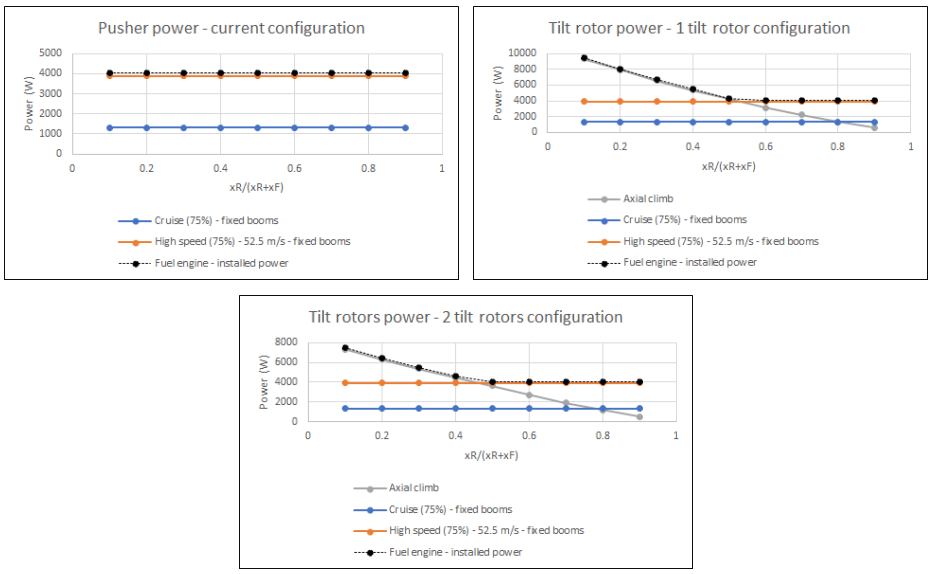

Figure 4.16: Powers required from the pusher/tilt rotor(s) for all 3 configurations and for different locations of the rotors. A 75% propeller efficiency is assumed

In figure 4.16, the power estimations for cruise and high speed condition consider the presence of fixed booms and, thus, the aerodynamic properties of section 4.1 are used. The axial climb power equations are found in [37]. From figure 4.16 and, for all 3 configurations and for different locations of the rotors, the minimum fuel engine installed power required (dashed black lines) is used to determine the aircraft maximum speed, as shown in table 4.3.

	Current configuration		**1 tilt rotor configuration**		**2 tilt rotors configuration**	
xR/(xR + xF)	**Power (W) Pusher**	**Maximum speed (m/s)**	**Power (W) 1 tilt rotor**	**Maximum speed (m/s)**	**Power (W) 2 tilt rotors**	**Maximum speed (m/s)**
0.1	3898	52.5	9326.4	70.9	7328.5	65.31
0.2	3898	52.5	7914.7	67.04	6316.6	62.07
0.3	3898	52.5	6585.9	62.96	5363.2	58.67
0.4	3898	52.5	5345.7	58.59	4472.5	55.08
0.5	3898	52.5	4201.2	53.88	3898	52.5
0.6	3898	52.5	3898	52.5	3898	52.5
0.7	3898	52.5	3898	52.5	3898	52.5
0.8	3898	52.5	3898	52.5	3898	52.5
0.9	3898	52.5	3898	52.5	3898	52.5

Table 4.3: Aircraft maximum speed for all 3 configurations and for different locations of the rotors

The left image of figure 4.17 shows the maximum speed achieved by the aircraft for all 3 configurations and for different locations of the rotors and, it is a graphical representation of the data shown in table 4.3. The right image of figure 4.17 shows the maximum speed increase, in percentage, when using a 1 tilt rotor configuration or a 2 tilt rotors configuration instead of the current configuration.

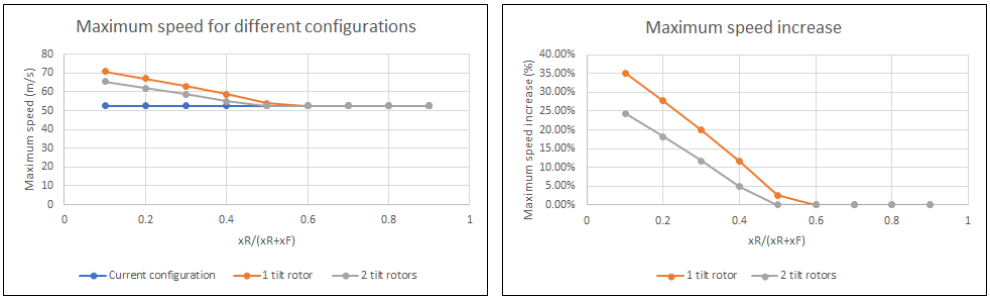

Figure 4.17: Maximum speed achieved by the aircraft for all 3 configurations and for different locations of the rotors.

From the right image of figure 4.17 and, when using fixed booms, a 1 tilt rotor configuration instead of the actual configuration increases the aircraft maximum speed if $\frac{x_R}{x_R+x_F} \leq 0.6$ and, a 2 tilt rotors configuration instead of the actual configuration increases the aircraft maximum speed if $\frac{x_R}{x_R+x_F} \leq 0.5$.

In terms of achieving the highest aircraft maximum speed, a 1 tilt rotor configuration should be used if $\frac{x_R}{x_R+x_F} \leq 0.6$. For other positions of the rotors, all configurations yield the same maximum speed.

Maximum speed increase - detachable booms

The same power estimations shown previously are done again, but now considering the presence of detachable booms. The same 3 propulsive system configurations and flight conditions are considered.

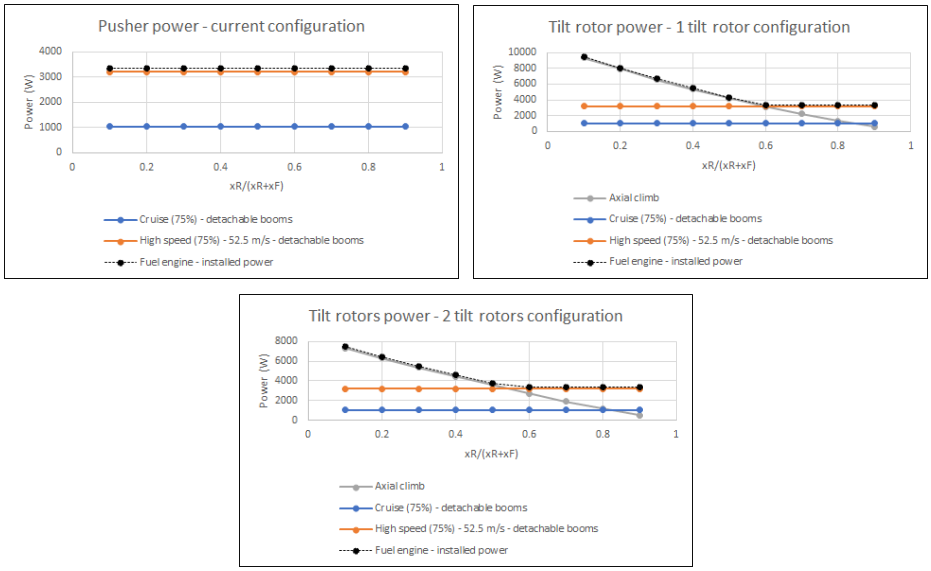

Figure 4.18: Powers required from the pusher/tilt rotor(s) for all 3 configurations and for different locations of the rotors. A 75% propeller efficiency is assumed

In figure 4.18, the power estimations for cruise and high speed condition consider the presence of

detachable booms and, thus, the aerodynamic properties of subsection 3.2.4 are used. The axial climb power equations are found in [37]. From figure 4.18 and, for all 3 configurations and for different locations of the rotors, the minimum fuel engine installed power required (dashed black lines) is used to determine the aircraft maximum speed, as shown in table 4.4.

	Current configuration		**1 tilt rotor configuration**		**2 tilt rotors configuration**	
xR/(xR + xF)	**Power (W) Pusher**	**Maximum speed (m/s)**	**Power (W) 1 tilt rotor**	**Maximum speed (m/s)**	**Power (W) 2 tilt rotors**	**Maximum speed (m/s)**
0.1	3200	52.5	9326.4	74.8	7328.5	69.1
0.2	3200	52.5	7914.7	70.86	6316.6	65.79
0.3	3200	52.5	6585.9	66.7	5363.2	62.33
0.4	3200	52.5	5345.7	62.26	4472.5	58.69
0.5	3200	52.5	4201.2	57.47	3636.6	54.79
0.6	3200	52.5	3200	52.5	3200	52.5
0.7	3200	52.5	3200	52.5	3200	52.5
0.8	3200	52.5	3200	52.5	3200	52.5
0.9	3200	52.5	3200	52.5	3200	52.5

Table 4.4: Aircraft maximum speed for all 3 configurations and for different locations of the rotors

The left image of figure 4.19 shows the maximum speed achieved by the aircraft for all 3 configurations and for different locations of the rotors and, it is a graphical representation of the data shown in table 4.4. The right image of figure 4.19 shows the maximum speed increase, in percentage, when using a 1 tilt rotor configuration or a 2 tilt rotors configuration instead of the current configuration.

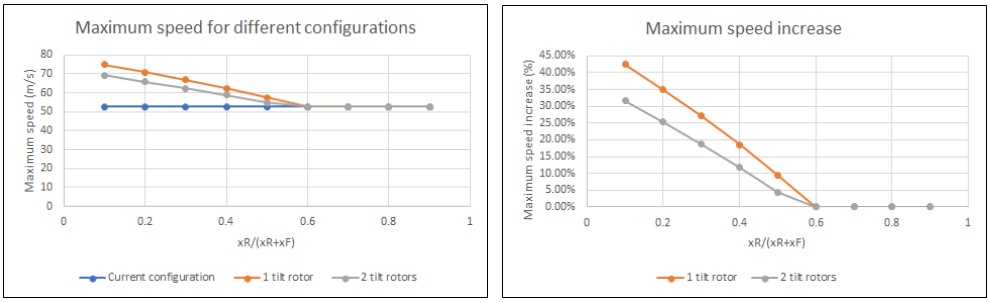

Figure 4.19: Maximum speed achieved by the aircraft for all 3 configurations and for different locations of the rotors.

From the right image of figure 4.19 and, when using detachable booms, both the 1 tilt rotor configuration and the 2 tilt rotors configuration instead of the actual configuration increase the aircraft maximum speed if $\frac{x_R}{x_R+x_F} \leq 0.6$.

In terms of achieving the highest aircraft maximum speed, a 1 tilt rotor configuration should be used if $\frac{x_R}{x_R+x_F} \leq 0.6$. For other positions of the rotors, all configurations yield the same maximum speed.

As a summary, tables 4.3 and 4.4 allow us to understand that, regardless if the booms are fixed or detachable, when $\frac{x_R}{x_R+x_F} \leq 0.6$, a 1 tilt rotor configuration is preferred in order to provide the aircraft with

a higher maximum speed. Furthermore, tables 4.3 and 4.4 also highlight the fact that having detachable booms is indeed more aerodynamic than having fixed booms. For the same maximum speed, less power is required and, for the same power, a higher maximum speed is achieved with detachable booms.

Propulsive system mass reduction

Assuming that it is possible to have electric motors whose maximum thrust is exactly the required thrust and, fuel engines whose installed power is exactly the required power, a study regarding the weight of the propulsive system is carried out.

Using data from electric motors available in the market, a cloud of points is obtained and a regression is used to have a first idea of the mass of a generic electric motor (see left image of figure 4.20). Using data from fuel engines available in the market, a cloud of points is obtained and a regression is used to have a first idea of the mass of a generic fuel engine (see right image of figure 4.20).

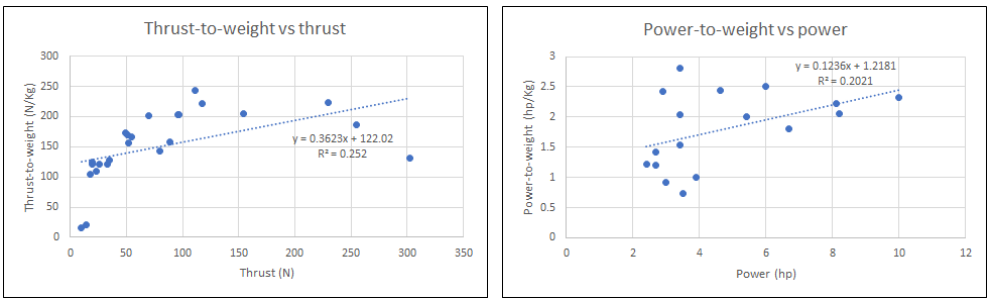

Figure 4.20: Left image: Thrust-to-weight vs maximum thrust for different electric motors. Right image: Power-to-weight vs installed power for different fuel engines

Using the values calculated for the required thrusts (in the case of electric motors) and powers (in the case of fuel engines), the mass of the propulsive system can be estimated for all 3 configurations and for different locations of the rotors, as shown in the left image of figure 4.21. The right image of figure 4.21 shows the mass variation, in percentage, when using a 1 tilt rotor configuration or a 2 tilt rotors configuration instead of the current configuration. A negative variation means a mass reduction, whereas a positive variation means a mass increase.

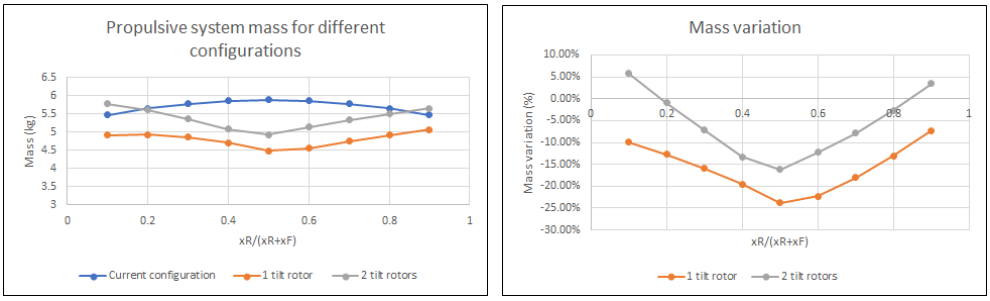

Figure 4.21: Left image: Mass of the propulsive system for all 3 configurations and for different locations of the rotors. Right image: Mass variation when using a 1 tilt rotor configuration or a 2 tilt rotors configuration instead of the current configuration

From the right image of figure 4.21, a 1 tilt rotor configuration instead of the actual configuration

reduces the propulsive system mass regardless of the positions of the rotors and, a 2 tilt rotors configuration instead of the actual configuration reduces the propulsive system mass if $0.2 \leq \frac{x_R}{x_R+x_F} \leq 0.8$.

In terms of achieving the highest propulsive system mass reduction, a 1 tilt rotor configuration should be used regardless of the positions of the rotors.

Overall analysis

Based on the studies conducted, the use of detachable booms instead of fixed booms should be adopted in future design versions. Furthermore, the current propulsive system configuration should be replaced by a 1 tilt rotor configuration in future design versions as well.

With this solution, a better aerodynamic performance is obtained. With the current configuration, at the cruise speed of 35 m/s, $L/D = 12.19$ and $W_{Fuel} = 2.45\ kg$. With the proposed future configuration, at the cruise speed of 35 m/s, $L/D = 15.54$ and $W_{Fuel} = 1.93\ kg$. Therefore, a fuel consumption reduction of $\simeq 20\%$ is verified when detachable booms and 1 tilt rotor are used.

As seen from figures 4.17 and 4.19, with a 1 tilt rotor configuration and once assured that the rotors are placed in such a way that $\frac{x_R}{x_R+x_F} \leq 0.6$, the aircraft maximum speed is increased. This increase is higher if detachable booms are used. The aircraft structural limits are not considered in these analyses.

In terms of propulsive system mass reduction, a 1 tilt rotor configuration instead of the current configuration is more advantageous for all positions of the rotors. This mass reduction can be used to increase the payload or the fuel amount (range) of the aircraft. If all the gained mass is used as payload, figure 4.22 is obtained. If all the gained mass is used as fuel, the range gain shown in the left image of figure 4.23 is obtained. For a cruise speed of 35 m/s, the mission time gain shown in the right image of figure 4.23 is obtained.

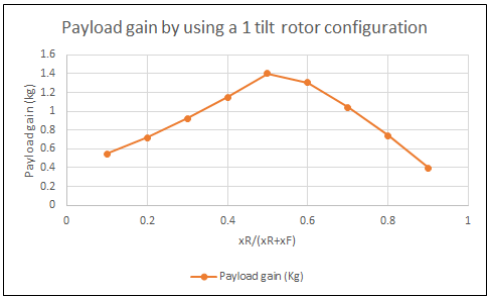

Figure 4.22: Maximum payload gain

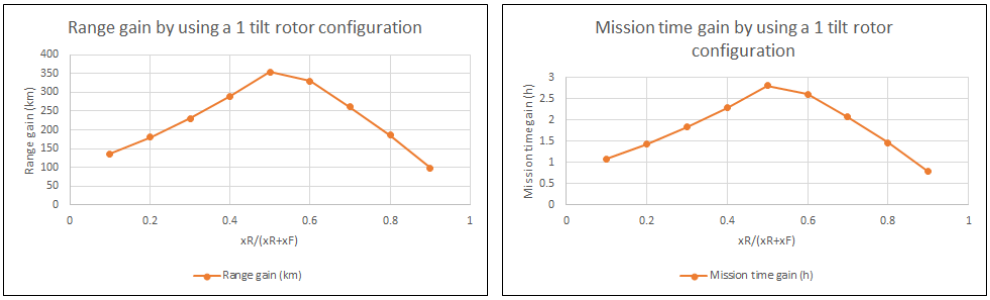

Figure 4.23: Left image: Maximum range gain. Right image: Maximum mission time gain

Chapter 5

Conclusions

5.1 Summary

Within the scope of this Master's Thesis in Aerospace Engineering, a new canard fixed-wing VTOL UAV to be used by the Canadian Air Force to conduct MAD operations was designed and developed.

First, using preliminary methods and, later, by doing a study with the help of CAD and CFD software, an optimized configuration for cruise condition was obtained for the aircraft. Suitable wing and canard airfoils, shape and dimensions of the lifting surfaces, fuselage, vertical fins, control surfaces, as well as the location of the lifting surfaces with respect to the fuselage were optimized in order to endow the aircraft with the most suitable magnetic interference, functionality, stability, aerodynamic and control characteristics. The CAD model of the aircraft optimized for cruise can be seen in figure 3.24.

After achieving an efficient aircraft configuration for cruise condition, the definition and implementation of the VTOL architecture was performed, bearing in mind magnetic interference, power consumption, aerodynamic, structural, vibration and control issues. The best location for the VTOL motors was determined. The solution adopted for the booms stiffens the aircraft structure to deal with the vibration of electric motors. The CAD model with the final configuration for the aircraft can be seen in figure 4.1.

Subsequently, aircraft aerodynamic, stability and power/fuel consumption characteristics were estimated, including the drag due to the presence of the VTOL architecture. The aircraft transition mode and dynamic stability behaviour were also analysed.

Lastly, solutions for possible improvements in future design versions of the aircraft were presented: the use of detachable booms for the front VTOL motors and the replacement of the current propulsive system configuration by a 1 tilt rotor configuration. These solutions will increase aerodynamic efficiency, reduce fuel consumption, increase maximum forward speed and reduce propulsive system mass.

5.2 Achievements

For this first design version of a new UAV, it was important to define and implement an aircraft design step-by-step method (with empirical and software tools) in order to size and obtain a valid aircraft con-

figuration to perform its mision in the most suitable way possible. In particular, the specific objectives to be met were listed in section 1.5.

Although experimental data from ground/flight testing is required to validate the current design of the aircraft, an overview of the aircraft performance can be established from a theoretical point of view. The results obtained in chapters 3 and 4 show that the goals mentioned in section 1.5 were achieved.

A fuselage capable of carrying the MAD-XR sensor and other internal components at an adequate distance from the MAD-XR sensor, together with the lifting surfaces, the vertical fins and the control surfaces provide adequate aerodynamic and stability characteristics to the aircraft. A simple and suitable VTOL architecture is implemented, after determining the best location for the VTOL motors and the best strategy to incorporate the booms. Transition is modeled and analysed, which is particularly useful to define the best control strategy for this flight stage. For the final configuration of this new aircraft, full aerodynamic and stability studies are performed. These studies allow to determine the aerodynamic forces and moments for different aerodynamic angles.

Possible improvements for future design versions are proposed. Additionally, after preforming ground and flight tests, this first design version will be useful to understand what characteristics of the aircraft should be tackled and modified in order to improve its overall performance in future design versions.

5.3 Future Work

5.3.1 Ground and flight testing

To validate the current design of the aircraft and identify issues to be improved in future design versions, there is the need to perform ground and flight tests. Building and testing a full-scale aircraft is a cumbersome and expensive process, so scale models are used to assess the characteristics of a full-scale aircraft.

A scale model is a physical representation of the full-scale aircraft, since accurate relationships between important aspects of the aircraft and physical variables are kept. A scale-model has the great advantages of being easier, faster and cheaper to build when compared to the full-scale aircraft. Based on dimensional analysis, geometric, kinematic and dynamic similarity rules are used to make the correct equivalence between the prototype (full-scale aircraft) and the model, so that the experimental results obtained from the latter can be compared to the theoretical results predicted for the former [64].

A model and prototype are geometrically similar if and only if all body dimensions in all three spatial coordinates have the same linear scale ratio. By having geometric similarity, all angles and flow directions are preserved. A model and prototype are kinematically similar if and only if they have the same length scale ratio and the same time scale ratio, meaning that the velocity scale ratio is also the same for both. A model and prototype are dynamically similar if and only if they have the same length scale ratio, the same time scale ratio and the same force scale (or mass scale) ratio [64].

To ensure similarity between model and prototype, a non-dimensional number is kept the same for both model and prototype. In the case of this project and, according to [65], the Froude number similarity

is used. The Froude number Fr is a non-dimensional number that gives the ratio between inertia forces and gravitational forces. It is defined, as a function of the speed U, the length L and the gravitational constant g, by equation 5.1.

$$Fr = \frac{U^2}{g \cdot L} \tag{5.1}$$

Based on the Froude similarity, mathematical relationships between all the physical variables for model (scaled down proof of concept) and prototype (sized aircraft) are derived and obtained. These relationships can be consulted in appendix D.

5.3.2 Use of folding propellers

A folding propeller is a type of propeller whose blades automatically fold out when the engine is turning (due to the centrifugal force), and then fold back (due to the airflow pressure) when the engine stops.

Folding propellers reduce drag while not in use, thereby allowing for more speed or reduced fuel consumption. Folding propellers also imply less noise and vibration than fixed blades when not in use, since fluid flow will not cause the propeller to rotate.

5.3.3 Magnetic shielding techniques/materials

Some magnetic shielding techniques/materials are indicated in order to have an aircraft with better magnetic properties: use of METGLAS® 2605SA1 & 2605HB1M Alloy and use of Niquel Epoxy Spray painting.

Use of METGLAS® 2605SA1 & 2605HB1M Alloy

Once created, magnetic fields cannot be blocked, i.e. all magnetic lines must start in the North Pole and terminate in the South Pole. However, instead of following their natural path, magnetic lines can be re-routed, i.e. it is possible to provide an alternative path for the magnetic lines to flow. This is achieved by using a ferromagnetic/high magnetic permeability material. A ferromagnetic material conducts magnetic flux better than other materials, meaning that a magnetic field will tend to flow along this material and avoid other materials and objects [66].

A better understanding of the phenomenon mentioned above can be seen in the next figure [66]:

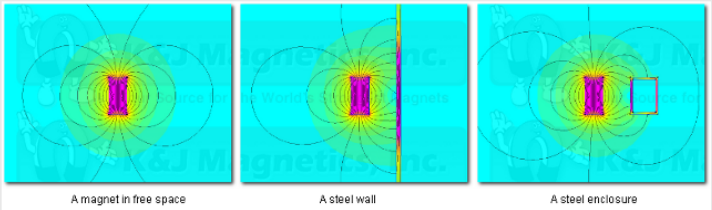

Figure 5.1: Magnetic shielding - use of a ferromagnetic material

The magnetic shielding with ferromagnetic materials can be employed in two ways, for example:

- By ”blocking” an object with a ferromagnetic material which can conduct magnetic flux better than the materials around it, the magnetic field will tend to flow along this material and avoid the object. Thus, by shielding the MAD-XR sensor with a high permeability material, the magnetic lines from the aircraft's components reaching the sensor and interfering with its operation will be reduced.
- By enclosing the VTOL motors and the fuel engine (main sources of magnetic noise) with a ferromagnetic material, part of the magnetic lines emanated from their magnets will take a shorter path (they will be ”reflected” by the ferromagnetic enclosure) and will not reach the MAD-XR sensor.

After some research for materials suitable for magnetic shielding, METGLAS® 2605SA1 & 2605HB1M Alloy was found. In [67], the general properties of this material can be checked.

Use of Niquel Epoxy Spray painting

METGLAS® 2605SA1 & 2605HB1M Alloy is good for magnetic shielding since it has a very high magnetic permeability. However, if the high flux density field is too strong for the high permeability shield, the shield will saturate. Therefore, a material with a high saturation induction should be used as well. This material would provide a first barrier to the magnetic lines, by weakening them. Once their flux density is smaller, the use of METGLAS® 2605SA1 & 2605HB1M Alloy would be enhanced [66].

As an example of practical application, the inside of the fuselage could be painted with Niquel Epoxy Spray painting. In [68], the general properties of this material can be checked.

5.3.4 Aircraft manufacturing, assembly and tooling

In terms of manufacturing, assembly and tooling of the aircraft, attention should be given to the fact that materials with strong magnetic properties can induce magnetisation in other materials. Tools that are magnetic or have become magnetized can in turn magnetize fasteners or other aircraft parts they contact. Thus, strong tool control and magnetic discipline are required to prevent magnetic contamination.

5.4 Final Conclusions

The several steps undertaken in this project intended to design a new canard fixed-wing Magnetic Anomaly Detection Unmanned Aerial Vehicle with Vertical Take-off and Landing capabilities which complies to a set of established mission requirements.

The designed aircraft presents a good solution and balance between all the magnetic interference, aerodynamic, stability, power and fuel consumption, control, structural and vibration issues mentioned throughout this thesis.

Besides all the Engineering-related skills acquired during this thesis, such as knowledge and experience in Aircraft Design, other important skills for my future as an engineer were achieved with this thesis: the capability of overcoming obstacles and challenges encountered, to be a valid member of a team with diverse range of skills in an international environment, problem solving skills, attention to detail and, ability to deal with clients and meet stringent deadlines.

Bibliography

[1] C.-C. B. Review. What is a drone? https://www.cbronline.com/what-is/what-is-a-drone-4946842/. [Online; accessed on March 2019].

[2] NOVA. 1940s —— V-1 (Germany). https://www.pbs.org/wgbh/nova/spiesfly/uavs_07.html. [Online; accessed on March 2019].

[3] J. F. The History Of Drones (Drone History Timeline From 1849 To 2019). https://www.dronethusiast.com/history-of-drones/. [Online; accessed on March 2019].

[4] T. Guardian. Drones by country: who has all the UAVs? https://www.theguardian.com/news/datablog/2012/aug/03/drone-stocks-by-country. [Online; accessed on March 2019].

[5] future of everything. 7 Ways Drones Are Actually Being Used Today. https://www.futureofeverything.io/ways-drones-used-today/. [Online; accessed on March 2019].

[6] M. MARGARITOFF. Watch the Ehang 184 Passenger Drone Successfully Taxi Someone Around. http://www.thedrive.com/aerial/18261/watch-the-ehang-184-passenger-drone-successfully-taxi-someone-around. [Online; accessed on March 2019].

[7] P. Jain. Magnetometers. https://www.engineersgarage.com/articles/magnetometer. [Online; accessed on March 2019].

[8] A. GEOPHYSICS. What is an aeromagnetic geophysical survey? http://www.ageophysics.com/en/blog/what-is-an-aeromagnetic-geophysical-survey/2/6. [Online; accessed on March 2019].

[9] T. A. Gardner. Magnetic Anomaly Detection. https://uboat.net/allies/technical/mad.htm. [Online; accessed on March 2019].

[10] C. Reeves. *Aeromagnetic Surveys. Principles, Practice Interpretation*. GEOSOFT, October 2005.

[11] Brican TD100. http://www.navaldrones.com/TD-100M.html, . [Online; accessed on March 2019].

[12] Brican TD100. https://www.int-arch-photogramm-remote-sens-spatial-inf-sci.net/XL-1-W4/143/2015/isprsarchives-XL-1-W4-143-2015.pdf, . [Online; accessed on March 2019].

[13] Height Technologies PD-1 UAV. https://heighttech.nl/wp-content/uploads/2018/10/Techspecs_PD-1.pdf. [Online; accessed on March 2019].

[14] Height Technologies PD-1 UAV. https://heighttech.nl/pd1/. [Online; accessed on March 2019].

[15] PD-1 UAS. https://pd1uas.com/. [Online; accessed on March 2019].

[16] HAASW UTAS. https://www.militaryaerospace.com/articles/2015/01/bae-subhunting-drone.html. [Online; accessed on March 2019].

[17] Northrop Grumman MQ-8 Fire Scout. https://www.militaryfactory.com/aircraft/detail.asp?aircraft_id=889#history. [Online; accessed on March 2019].

[18] Fire Scout VTUAV. https://www.naval-technology.com/projects/fire-scout-vtuav/. [Online; accessed on March 2019].

[19] Geoscan 201. https://www.geoscan.aero/en/products/geoscan201/base, . [Online; accessed on March 2019].

[20] Geoscan 201. https://geo-matching.com/uas-for-mapping-and-3d-modelling/geoscan-201, . [Online; accessed on March 2019].

[21] GeoSurv II. http://2014uav.mae.carleton.ca/geosurv-ii-prototype/, . [Online; accessed on March 2019].

[22] GeoSurv II. http://2014uav.mae.carleton.ca/fleet/, . [Online; accessed on March 2019].

[23] CAE. Magnetic Anomaly Detection Extended Role (MAD-XR). https://www.cae.com/media/media-center/documents/datasheet.MAD-XR.pdf. [Online; accessed on March 2019].

[24] C. R. D. Hansen. Magnetic Signature Characterization of a Fixed-Wing Vertical Take-off and Landing (VTOL) Unmanned Aircraft Vehicle (UAV). https://fenix.tecnico.ulisboa.pt/downloadFile/1126518382196687/MAGNETIC%20VTOL%20UAV%20-%20PROJECT%20#2-REPORT.pdf. [Online; accessed on March 2019].

[25] XFOIL - Subsonic Airfoil Development System. https://web.mit.edu/drela/Public/web/xfoil/. [Online; accessed on April 2019].

[26] A. I. Mark Drela, MIT Aero Astro/Harold Youngren. XFOIL 6.9 User Primer. https://web.mit.edu/drela/Public/web/xfoil/xfoil_doc.txt. [Online; accessed on April 2019].

[27] M. D. o. A. Mark Drela and Astronautics. XFOIL: An Analysis and Design System for Low Reynolds Number Airfoils. http://web.mit.edu/drela/Public/papers/xfoil_sv.pdf. [Online; accessed on April 2019].

[28] A. for Students. 3D PRANDTL LIFTING LINE THEORY. http://www.aerodynamics4students.com/subsonic-aerofoil-and-wing-theory/3d-prandtl-lifting-line-theory.php. [Online; accessed on April 2019].

[29] V. de Brederode. *Fundamentos de Aerodinâmica Incompressível*. IST Press, 1997.

[30] XFLR5. Analysis of foils and wings operating at low Reynolds numbers. https://sourceforge.net/projects/xflr5/files/. [Online; accessed on April 2019].

[31] NASA. Navier-Stokes Equations. https://www.grc.nasa.gov/www/k-12/airplane/nseqs.html, . [Online; accessed on April 2019].

[32] F. R. Menter. Two-equation eddy-viscosity turbulence models for engineering applications. *AIAA Journal*, 32(8):1598–1605, 1994.

[33] H. Hamburgh. Empennage Sizing. https://www.fzt.haw-hamburg.de/pers/Scholz/HOOU/AircraftDesign_11_EmpennageSizing.pdf. [Online; accessed on April 2019].

[34] J. ROSKAM and C. LAN. *Airplane Aerodynamics and Performance*. Roskam Aviation and Engineering Corporation, 2003.

[35] M. Sadraey. *Aircraft Design: A Systems Engineering Approach*. A John Wiley Sons, Ltd., Publication, 2013.

[36] D. TREST. How to choose the right motor for your multicopter drone. https://www.dronetrest.com/t/how-to-choose-the-right-motor-for-your-multicopter-drone/568. [Online; accessed on May 2019].

[37] J. G. Leishman. *Principles of Helicopter Aerodynamics*. Cambridge Aerospace Series, 2002.

[38] A. R.-S. Ashraf M Kamal. Design methodology for hybrid (vtol + fixed wing) unmanned aerial vehicles. *Aeronautics and Aerospace Open Access Journal*, 2, 2018.

[39] *An Illustrated Dictionary of Aviation Copyright*. The McGraw-Hill Companies, 2005.

[40] B. Etkin and L. D. Reid. *Dynamics of Flight: Stability and Control*. John Wiley and Sons, 1996.

[41] D. Gruyter. Propeller Pitch Change Mechanism. https://www.degruyter.com/downloadpdf/books/9783110401509/9783110401509.6/9783110401509.6.pdf. [Online; accessed on May 2019].

[42] W. F. Phillips. *Mechanics of Flight*. A John Wiley Sons, Ltd., Publication, 2009.

[43] MathWorks. fmincon. https://www.mathworks.com/help/optim/ug/fmincon.html. [Online; accessed on May 2019].

[44] U. A. A. Group. UIUC Airfoil Coordinates Database. https://m-selig.ae.illinois.edu/ads/coord_database.html. [Online; accessed on May 2019].

[45] S. Gudmundsson. *General Aviation Aircraft Design: Applied Methods and Procedures*. Elsevier, Inc, 2013.

[46] boldmethod. How Wing Washout Makes Your Airplane More Stable. https://www.boldmethod.com/learn-to-fly/aircraft-systems/wing-washout-how-it-makes-your-airplane-more-stable/. [Online; accessed on May 2019].

[47] T. C. Corke. *Design of Aircraft*. 4th edn, Prentice Hall, 2003.

[48] R. T. Whitcomb. *A design approach and selected wind-tunnel results at high subsonic speeds for wing-tip mounted winglets*. NASA, 1976.

[49] S. N. Air and S. Museum. What is the difference between the high wing, mid wing and low wing? https://howthingsfly.si.edu/ask-an-explainer/what-difference-between-high-wing-mid-wing-and-low-wing. [Online; accessed on June 2019].

[50] A. F. H. (FAA-H-8083-3B). Maintaining Aircraft Control: Upset Prevention and Recovery Training. https://www.faa.gov/regulations_policies/handbooks_manuals/aviation/airplane_handbook/media/06_afh_ch4.pdf. [Online; accessed on June 2019].

[51] NASA. Shape Effects on Drag. https://www.grc.nasa.gov/www/k-12/airplane/shaped.html, . [Online; accessed on June 2019].

[52] R. D. Blevins. *Applied Fluid Dynamics Handbook*. Van Nostrand Reinhold Company, Inc, 1984.

[53] F. Aerodynamics. What is the most aerodynamic shape? https://www.papertrell.com/apps/preview/The-Handy-Physics-Answer-Book/Handy%20Answer%20book/What-is-the-most-aerodynamic-shape/001137019/content/SC/52caff9682fad14abfa5c2e0_default.html. [Online; accessed on June 2019].

[54] WolframMathWorld. Teardrop Curve. http://mathworld.wolfram.com/TeardropCurve.html. [Online; accessed on June 2019].

[55] KDEDirect. KDE10218XF-105. https://www.kdedirect.com/collections/uas-multi-rotor-brushless-motors/products/kde10218xf-105. [Online; accessed on June 2019].

[56] A. S. Exchange. What is the reason of having an Angle of Incidence on an airplane? https://aviation.stackexchange.com/questions/32573/what-is-the-reason-of-having-an-angle-of-incidence-on-an-airplane. [Online; accessed on July 2019].

[57] MIT. Aircraft Range: the Breguet Range Equation. https://web.mit.edu/16.unified/www/FALL/thermodynamics/notes/node98.html. [Online; accessed on July 2019].

[58] FliteTest. WHAT IS WING LOADING? https://www.flitetest.com/articles/what-is-wing-loading. [Online; accessed on August 2019].

[59] unmanned air vehicle. Classification by wing loading. https://sites.google.com/site/unmannedairvehicle/classification-by-wing-loading. [Online; accessed on August 2019].

[60] K. Aerospace. DISC LOADING AND HOVER EFFICIENCY. https://www.krossblade.com/disc-loading-and-hover-efficiency. [Online; accessed on August 2019].

[61] A. Bacchini and E. Cestino. Electric vtol configurations comparison. *Aerospace*, 6, 2019.

[62] R. B. Bramlette and R. M. Barrett. Design and flight testing of a convertible quadcopter for maximum flight speed. *AIAA Journal*, 2017.

[63] T. H. G. Megson. *Aircraft Structures for Engineering Students*. Arnold, 1999.

[64] F. M. White. *FLUID MECHANICS*. McGraw-Hill, 2011.

[65] J. Chester H. Wolowicz, James S. Bowman and W. P. Gilbert. Similitude Requirements and Scaling Relationships as Applied to Model Testing. https://ntrs.nasa.gov/archive/nasa/casi.ntrs.nasa.gov/19790022005.pdf. [Online; accessed on September 2019].

[66] I. K&J Magnetics. Shielding materials. https://www.kjmagnetics.com/blog.asp?p=shielding-materials. [Online; accessed on September 2019].

[67] I. MetglasR©. METGLASR©2605SA1 & 2605HB1M Alloy. https://metglas.com/magnetic-materials/. [Online; accessed on September 2019].

[68] M. Chemicals. Niquel Epoxy Spray Painting. https://www.mgchemicals.com/products/. [Online; accessed on September 2019].

Appendix A

Dimensional and non-dimensional stability derivatives

A.1 Dimensional stability derivatives

In [40], expressions for the dimensional stability derivatives X_u, X_w, Z_u, Z_w, $Z_{\dot{w}}$, Z_q, M_u, M_w, $M_{\dot{w}}$, M_q, Y_v, Y_p, Y_r, L_v, L_p, L_r, N_v, N_p and N_r can be found.

$$X_u = \frac{1}{2} \cdot \rho \cdot S_w \cdot u_0 \cdot C_{xu} \tag{A.1}$$

$$X_w = \frac{1}{2} \cdot \rho \cdot S_w \cdot u_0 \cdot C_{x\alpha} \tag{A.2}$$

$$Z_u = \frac{-2 \cdot W}{u_0} + \frac{1}{2} \cdot \rho \cdot S_w \cdot u_0 \cdot C_{zu} \tag{A.3}$$

$$Z_w = \frac{1}{2} \cdot \rho \cdot S_w \cdot u_0 \cdot C_{z\alpha} \tag{A.4}$$

$$Z_{\dot{w}} = \frac{1}{4} \cdot \rho \cdot S_w \cdot \bar{c}_w \cdot C_{z\dot{\alpha}} \tag{A.5}$$

$$Z_q = \frac{1}{4} \cdot \rho \cdot S_w \cdot u_0 \cdot \bar{c}_w \cdot C_{zq} \tag{A.6}$$

$$M_u = \frac{1}{2} \cdot \rho \cdot S_w \cdot u_0 \cdot \bar{c}_w \cdot C_{mu} \tag{A.7}$$

$$M_w = \frac{1}{2} \cdot \rho \cdot S_w \cdot u_0 \cdot \bar{c}_w \cdot C_{m\alpha} \tag{A.8}$$

$$M_{\dot{w}} = \frac{1}{4} \cdot \rho \cdot S_w \cdot \bar{c}_w^2 \cdot C_{m\dot{\alpha}} \tag{A.9}$$

$$M_q = \frac{1}{4} \cdot \rho \cdot S_w \cdot u_0 \cdot \bar{c}_w^2 \cdot C_{mq} \tag{A.10}$$

$$Y_v = \frac{1}{2} \cdot \rho \cdot S_w \cdot u_0 \cdot C_{y\beta} \tag{A.11}$$

$$Y_p = \frac{1}{4} \cdot \rho \cdot S_w \cdot u_0 \cdot b_w \cdot C_{yp} \tag{A.12}$$

$$Y_r = \frac{1}{4} \cdot \rho \cdot S_w \cdot u_0 \cdot b_w \cdot C_{yr} \tag{A.13}$$

$$L_v = \frac{1}{2} \cdot \rho \cdot S_w \cdot u_0 \cdot b_w \cdot C_{l\beta} \tag{A.14}$$

$$L_p = \frac{1}{4} \cdot \rho \cdot S_w \cdot u_0 \cdot b_w^2 \cdot C_{lp} \tag{A.15}$$

$$L_r = \frac{1}{4} \cdot \rho \cdot S_w \cdot u_0 \cdot b_w^2 \cdot C_{lr} \tag{A.16}$$

$$N_v = \frac{1}{2} \cdot \rho \cdot S_w \cdot u_0 \cdot b_w \cdot C_{n\beta} \tag{A.17}$$

$$N_p = \frac{1}{4} \cdot \rho \cdot S_w \cdot u_0 \cdot b_w^2 \cdot C_{np} \tag{A.18}$$

$$N_r = \frac{1}{4} \cdot \rho \cdot S_w \cdot u_0 \cdot b_w^2 \cdot C_{nr} \tag{A.19}$$

, where ρ stands for the air density, S_w stands for the wing area, $\bar{c}_w$ stands for the wing mean chord, b_w stands for the wingspan, u_0 stands for the aircraft forward velocity and expressions for all the non-dimensional stability derivatives can be found in section A.2.

A.2 Non-dimensional stability derivatives

The non-dimensional stability derivatives C_{xu}, $C_{x\alpha}$, C_{zu}, $C_{z\alpha}$, $C_{z\dot{\alpha}}$, C_{zq}, C_{mu}, $C_{m\alpha}$, $C_{m\dot{\alpha}}$, C_{mq}, $C_{y\beta}$, C_{yp}, C_{yr}, $C_{l\beta}$, C_{lp}, C_{lr}, $C_{n\beta}$, C_{np} and C_{nr} are necessary to compute the dimensional stability derivatives, as can be seen in section A.1.

The values for $C_{m\alpha}$, $C_{y\beta}$, $C_{l\beta}$ and $C_{n\beta}$ are obtained from the CFD analysis performed in section 4.1. Expressions for the remaining derivatives can be found in [40].

$$C_{xu} = -3 \cdot C_{D0} \tag{A.20}$$

$$C_{zu} = 0 \tag{A.21}$$

$$C_{mu} = 0 \tag{A.22}$$

$$C_{x\alpha} = C_{L0} - C_{D\alpha} \tag{A.23}$$

$$C_{z\alpha} = -(C_{L\alpha} + C_{D0}) \tag{A.24}$$

$$C_{zq} = 1.1 \cdot 2 \cdot \frac{x_c \cdot S_c}{\bar{c}_w \cdot S_w} \cdot a_c \tag{A.25}$$

$$C_{mq} = -1.1 \cdot 2 \cdot \frac{x_c \cdot S_c}{\bar{c}_w \cdot S_w} \cdot a_c \cdot \frac{x_c}{\bar{c}_w} \tag{A.26}$$

$$C_{z\dot{alpha}} = 2 \cdot \frac{x_c \cdot S_c}{\bar{c}_w \cdot S_w} \cdot a_c \cdot \epsilon \tag{A.27}$$

$$C_{m\dot{alpha}} = -2 \cdot \frac{x_c \cdot S_c}{\bar{c}_w \cdot S_w} \cdot a_c \cdot \epsilon \cdot \frac{x_c}{\bar{c}_w} \tag{A.28}$$

$$C_{yp} = -2 \cdot a_f \cdot \frac{S_f}{S_w} \cdot \frac{z_f}{b_w} \tag{A.29}$$

$$C_{lp} = -4 \cdot \frac{a_w}{S_w \cdot b_w^2} \cdot \int_0^{b/2} y^2 \cdot c(y) dy \tag{A.30}$$

$$C_{np} = -\frac{C_{L0}}{8} + 2 \cdot a_f \cdot \frac{z_f}{b_w} \cdot \frac{x_f \cdot S_f}{b_w \cdot S_w}. \tag{A.31}$$

$$C_{yr} = 2 \cdot a_f \cdot \frac{S_f}{S_w} \cdot \frac{x_f}{b_w} \tag{A.32}$$

$$C_{lr} = 8 \cdot \frac{C_{L0}}{S_w \cdot b_w^2} \cdot \int_0^{b/2} y^2 \cdot c(y) dy + 2 \cdot a_f \cdot \frac{z_f}{b_w} \cdot \frac{x_f \cdot S_f}{b_w \cdot S_w} \tag{A.33}$$

$$C_{nr} = -2 \cdot a_f \cdot \frac{x_f \cdot S_f}{b_w \cdot S_w} \cdot \frac{x_f}{b_w} \tag{A.34}$$

Appendix B

Formulas used to estimate the aerodynamics derivatives

For the case of the theories used in the preliminary sizing (Lifting Line Theory and Panel Method), the computation of the derivatives C_{L0}, $C_{L\alpha}$, C_{Li_c}, C_{D0}, $C_{D\alpha}$, $C_{D\alpha^2}$, C_{Di_c}, $C_{Di_c^2}$, $C_{D\alpha i_c}$, C_{M0}, $C_{M\alpha}$ and C_{Mi_c} is done in accordance with the following formulas:

Lift derivatives

As a first approximation, the total lift of the aircraft L can be assumed to be due to the contributions of the wing lift L_w and canard lift L_c. Thus, equation B.1 can be obtained. Dividing all the terms of equation B.1 by the dynamic pressure q and the wing area S_w, equation B.2 can be obtained.

$$L = L_w + L_c \tag{B.1}$$

$$C_L = C_{L_w} + \frac{S_c}{S_w} \cdot C_{L_c} \tag{B.2}$$

The wing lift coefficient C_{L_w} is given, as a function of the angle of attack α, the wing lift derivative with respect to its angle of incidence a_w and the wing lift at zero angle of incidence w_0, by equation B.3. The values of a_w and w_0 can be computed from figure 3.4.

The canard lift coefficient C_{L_c} is given, as a function of the angle of attack α, the canard angle of incidence i_c, the canard lift derivative with respect to its angle of incidence a_c and the canard lift at zero angle of incidence c_0, by equation B.4. The values of a_c and c_0 can be computed from figure 3.6.

$$C_{L_w} = a_w \cdot \alpha + w_0 \tag{B.3}$$

$$C_{L_c} = a_c \cdot (\alpha + i_c) + c_0 \tag{B.4}$$

Inserting equations B.3 and B.4 into equation B.2, equation B.5 can be derived.

$$C_L = w_0 + \frac{S_c}{S_w} \cdot c_0 + (a_w + \frac{S_c}{S_w} \cdot a_c) \cdot \alpha + \frac{S_c}{S_w} \cdot a_c \cdot i_c = C_{L0} + C_{L\alpha} \cdot \alpha + C_{Li_c} \cdot i_c \tag{B.5}$$

Thus, by inspection of equation B.5, mathematical expressions can be obtained for the lift derivatives C_{L0}, $C_{L\alpha}$ and C_{Li_c}, respectively given by equations B.6, B.7 and B.8.

$$C_{L0} = w_0 + \frac{S_c}{S_w} \cdot c_0 \tag{B.6}$$

$$C_{L\alpha} = a_w + \frac{S_c}{S_w} \cdot a_c \tag{B.7}$$

$$C_{Li_c} = \frac{S_c}{S_w} \cdot a_c \tag{B.8}$$

Drag derivatives

As a first approximation, the total drag of the aircraft D can be assumed to be due to the contributions of the wing drag D_w, canard drag D_c and fuselage drag D_{fus}. Thus, equation B.9 can be obtained. Dividing all the terms of equation B.9 by the dynamic pressure q and the wing area S_w, equation B.10 can be obtained.

$$D = D_w + D_c + D_{fus} \tag{B.9}$$

$$C_D = C_{D_w} + \frac{S_c}{S_w} \cdot C_{D_c} + C_{D_fus} \tag{B.10}$$

The wing drag coefficient C_{D_w} is given, as a function of the angle of attack α, by equation B.11. The values of a_1, a_2 and a_3 can be computed from figure 3.4.

The canard drag coefficient C_{D_c} is given, as a function of the angle of attack α and the canard angle of incidence i_c, by equation B.12. The values of b_1, b_2 and b_3 can be computed from figure 3.6.

The fuselage drag coefficient C_{D_fus} is given, as a function of the angle of attack α, by equation B.13. The values of c_1, c_2 and c_3 can be computed from figure 3.10.

$$C_{D_w} = a_1 \cdot \alpha^2 + a_2 \cdot \alpha + a_3 \tag{B.11}$$

$$C_{D_c} = b_1 \cdot (\alpha + i_c)^2 + b_2 \cdot (\alpha + i_c) + b_3 \tag{B.12}$$

$$C_{D_fus} = c_1 \cdot \alpha^2 + c_2 \cdot \alpha + c_3 \tag{B.13}$$

Inserting equations B.11 - B.13 into equation B.10, equation B.14 can be derived.

$$
\begin{aligned}
C_D = a_3 + \frac{S_c}{S_w} \cdot b_3 + c_3 + (a_2 + \frac{S_c}{S_w} \cdot b_2 + c_2) \cdot \alpha + (a_1 + \frac{S_c}{S_w} \cdot b_1 + c_1) \cdot \alpha^2 + \\
+ \frac{S_c}{S_w} \cdot b_2 \cdot i_c + \frac{S_c}{S_w} \cdot b_1 \cdot i_c^2 + \frac{S_c}{S_w} \cdot 2 \cdot b_1 \cdot \alpha \cdot i_c = \\
= C_{D0} + C_{D\alpha} \cdot \alpha + C_{D\alpha^2} \cdot \alpha^2 + C_{Di_c} \cdot i_c + C_{Di_c^2} \cdot i_c^2 + C_{D\alpha i_c} \cdot \alpha \cdot i_c
\end{aligned} \tag{B.14}
$$

Thus, by inspection of equation B.14, mathematical expressions can be obtained for the drag derivatives C_{D0}, $C_{D\alpha}$, $C_{D\alpha^2}$, C_{Di_c}, $C_{Di_c^2}$ and $C_{D\alpha i_c}$, respectively given by equations B.15, B.16, B.17, B.18, B.19 and B.20.

$$
C_{D0} = a_3 + \frac{S_c}{S_w} \cdot b_3 + c_3 \tag{B.15}
$$

$$
C_{D\alpha} = a_2 + \frac{S_c}{S_w} \cdot b_2 + c_2 \tag{B.16}
$$

$$
C_{D\alpha^2} = a_1 + \frac{S_c}{S_w} \cdot b_1 + c_1 \tag{B.17}
$$

$$
C_{Di_c} = \frac{S_c}{S_w} \cdot b_2 \tag{B.18}
$$

$$
C_{Di_c^2} = \frac{S_c}{S_w} \cdot b_1 \tag{B.19}
$$

$$
C_{D\alpha i_c} = \frac{S_c}{S_w} \cdot 2 \cdot b_1 \tag{B.20}
$$

Pitch Moment derivatives

As a first approximation, the total pitch moment of the aircraft M can be assumed to be due to the contributions of the wing aerodynamic center moment M_{acw}, the canard aerodynamic center moment M_{acc}, the moment due to the wing lift $x_w \cdot L_w$ and the moment due to the canard lift $x_c \cdot L_c$. Thus, equation B.21 can be obtained. Dividing all the terms of equation B.21 by the dynamic pressure q, the wing area S_w and the wing mean chord $\bar{c}_w$, equation B.22 can be obtained.

$$
M = M_{acw} + M_{acc} + x_c \cdot L_c - x_w \cdot L_w \tag{B.21}
$$

$$
C_M = C_{Macw} + \frac{S_c \cdot \bar{c}_c}{S_w \cdot \bar{c}_w} \cdot C_{Macc} + \frac{x_c \cdot S_c}{\bar{c}_w \cdot S_w} \cdot C_{L_c} - \frac{x_w}{\bar{c}_w} \cdot C_{L_w} \tag{B.22}
$$

, where the wing lift coefficient C_{L_w} is given by equation B.3 and the canard lift coefficient C_{L_c} is given by equation B.4.

Inserting equations B.3 and B.4 into equation B.22, equation B.23 can be derived.

$$
\begin{aligned}
C_M = C_{Macw} + \frac{S_c \cdot \bar{c}_c}{S_w \cdot \bar{c}_w} \cdot C_{Macc} + \frac{x_c \cdot S_c}{\bar{c}_w \cdot S_w} \cdot c_0 - \frac{x_w}{\bar{c}_w} \cdot w_0 + \\
+ (\frac{x_c \cdot S_c}{\bar{c}_w \cdot S_w} \cdot a_c - \frac{x_w}{\bar{c}_w} \cdot a_w) \cdot \alpha + \frac{x_c \cdot S_c}{\bar{c}_w \cdot S_w} \cdot a_c \cdot i_c = \\
= C_{M0} + C_{M\alpha} \cdot \alpha + C_{Mi_c} \cdot i_c
\end{aligned}
\tag{B.23}
$$

Thus, by inspection of equation B.23, mathematical expressions can be obtained for the pitch moment derivatives C_{M0}, $C_{M\alpha}$ and C_{Mi_c}, respectively given by equations B.24, B.25 and B.26.

$$
C_{M0} = C_{Macw} + \frac{S_c \cdot \bar{c}_c}{S_w \cdot \bar{c}_w} \cdot C_{Macc} + \frac{x_c \cdot S_c}{\bar{c}_w \cdot S_w} \cdot c_0 - \frac{x_w}{\bar{c}_w} \cdot w_0 \tag{B.24}
$$

$$
C_{M\alpha} = \frac{x_c \cdot S_c}{\bar{c}_w \cdot S_w} \cdot a_c - \frac{x_w}{\bar{c}_w} \cdot a_w \tag{B.25}
$$

$$
C_{Mi_c} = \frac{x_c \cdot S_c}{\bar{c}_w \cdot S_w} \cdot a_c \tag{B.26}
$$

Appendix C

Flow interaction between wing and canard

Figures with the flow interaction between wing and canard for low speed (18 m/s), cruise speed (35 m/s) and high speed (52.5 m/s) trimmed conditions are presented for different canard configurations in figures C.1 - C.3.

High canard configuration

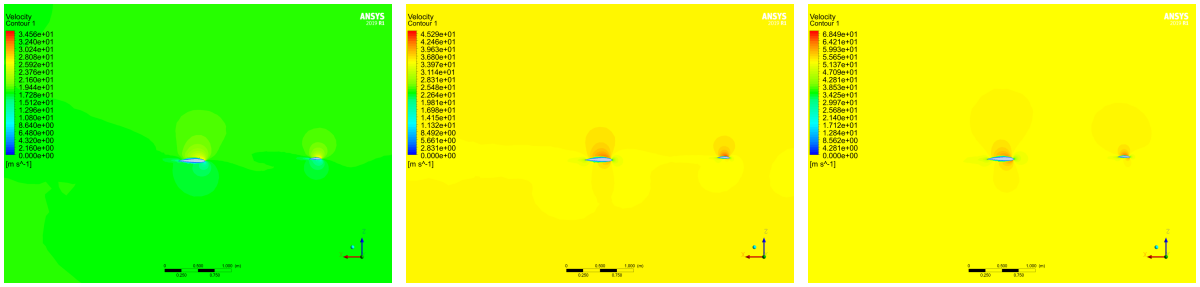

Figure C.1: Left image: Low speed (18 m/s). Middle image: Cruise speed (35 m/s). Right image: High speed (52.5 m/s)

Mid canard configuration

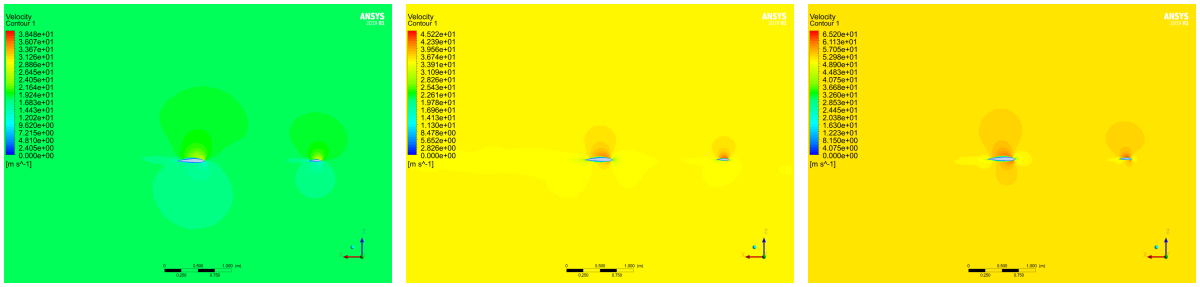

Figure C.2: Left image: Low speed (18 m/s). Middle image: Cruise speed (35 m/s). Right image: High speed (52.5 m/s)

Low canard configuration

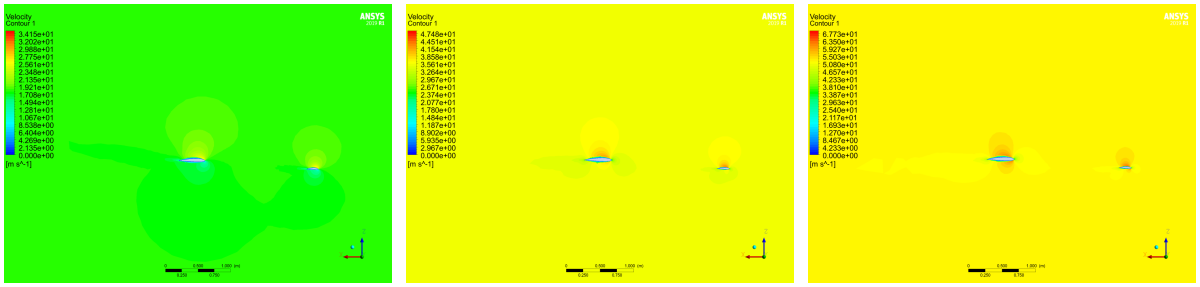

Figure C.3: Left image: Low speed (18 m/s). Middle image: Cruise speed (35 m/s). Right image: High speed (52.5 m/s)

Appendix D

Scaling laws between model and prototype

Based on the Froude similarity, the complete list with the scaling laws that relate the different physical variables of model and prototype is presented below. Note that the density of the model and prototype is assumed to be the same.

$$\frac{L_m}{L_p} = n \quad \text{(D.1)} \qquad \frac{\theta_m}{\theta_p} = 1 \quad \text{(D.2)} \qquad \frac{U_m}{U_p} = n^{0.5} \quad \text{(D.3)}$$

$$\frac{\omega_m}{\omega_p} = n^{-0.5} \quad \text{(D.4)} \qquad \frac{t_m}{t_p} = n^{0.5} \quad \text{(D.5)} \qquad \frac{Re_m}{Re_p} = n^{1.5} \quad \text{(D.6)}$$

$$\frac{a_m}{a_p} = 1 \quad \text{(D.7)} \qquad \frac{\alpha_m}{\alpha_p} = n^{-1} \quad \text{(D.8)} \qquad \frac{Press_m}{Press_p} = n \quad \text{(D.9)}$$

$$\frac{T_m}{T_p} = n \quad \text{(D.10)} \qquad \frac{E_m}{E_p} = n^4 \quad \text{(D.11)} \qquad \frac{P_m}{P_p} = n^{3.5} \quad \text{(D.12)}$$

$$\frac{J_m}{J_p} = 1 \quad \text{(D.13)} \qquad \frac{F_m}{F_p} = n^3 \quad \text{(D.14)} \qquad \frac{C_{Fm}}{C_{Fp}} = 1 \quad \text{(D.15)}$$

$$\frac{C_{F\theta m}}{C_{F\theta p}} = 1 \quad \text{(D.16)} \qquad \frac{M_m}{M_p} = n^4 \quad \text{(D.17)} \qquad \frac{C_{Mm}}{C_{Mp}} = 1 \quad \text{(D.18)}$$

$$\frac{C_{M\theta m}}{C_{M\theta p}} = 1 \quad \text{(D.19)} \qquad \frac{m_m}{m_p} = n^3 \quad \text{(D.20)} \qquad \frac{I_m}{I_p} = n^5 \quad \text{(D.21)}$$

, where L is the length, θ is the angle, U is the linear speed, ω is the angular speed, t is the time, Re is the Reynolds number, a is the linear acceleration, α is the angular acceleration, $Press$ is the pressure,

T is the temperature, E is the energy, P is the power, J is the advance ratio, F is the force, C_F is the force coefficient, $C_{F\theta}$ is the derivative of the force coefficient with respect to the angle, M is the moment, C_M is the moment coefficient, $C_{M\theta}$ is the derivative of the moment coefficient with respect to the angle, m is the mass and I is the inertia.

The subscripts m and p refer to the model and prototype, respectively.